# THE POTENTIAL FOR ENERGY EXTRACTION FROM FLUTTER

A Thesis Submitted

To the Division of Graduate Studies of the Royal Military College of Canada

by

Luba Bohdanna Goyaniuk, BSc

In Partial Fulfillment of the Requirements for the Degree of Master of

Applied Science in Mechanical Engineering

JUNE 2018

**ROYAL MILITARY COLLEGE OF CANADA**
**COLLÈGE MILITAIRE ROYAL DU CANADA**

DIVISION OF GRADUATE STUDIES AND RESEARCH
DIVISION DES ÉTUDES SUPÉRIEURES ET DE LA RECHERCHE

This is to certify that the thesis prepared by / Ceci certifie que la thèse rédigée par

**LUBA BOHDANNA GOYANIUK**

entitled / intitulée

**THE POTENTIAL FOR ENERGY EXTRACTION FROM FLUTTER**

Complies with the Royal Military College of Canada regulations and that it meets the accepted standards of the Graduate School with respect to quality, and, in the case of a doctoral thesis, originality, / satisfait aux règlements du Collège militaire royal du Canada et qu'elle respecte les normes acceptées par la Faculté des études supérieures quant à la qualité et, dans le cas d'une thèse de doctorat, l'originalité,

for the degree of / pour le diplôme de

**MASTER OF APPLIED SCIENCE IN MECHANICAL ENGINEERING**

Signed by the final examining committee: /
Signé par les membres du comité examinateur de la soutenance de thèse

_____, Chair / Président

_____, External Examiner / Examinateur externe

_____, Main Supervisor / Directeur de thèse principal

_____

Approved by the Head of Department : /
Approuvé par le Directeur du Département :_____ Date: _____

To the Librarian: This thesis is not to be regarded as classified. /
Au Bibliothécaire : Cette thèse n'est pas considérée comme une publication restreinte.

_____
Main Supervisor / Directeur de thèse principal

# Abstract

The power generated by the movement of the Earth's atmosphere is estimated to be hundreds of terrawatts. As a result, there has been particular interest in wind power generation. The high cost-factor, requirement for large towers, noise concerns, threat to birds of horizontal-axis wind turbines, along with basic engineering curiosity, have motivated the development of flapping (reciprocating) mechanisms to extract energy from the wind. The focus of this research is on alternative sustainable energy extraction from reciprocating oscillating airfoils, since there is energy available to be extracted from the flow through flutter induced Limit Cycle Oscillations (LCOs). Flutter is an aeroelastic dynamic phenomenon generally resulting from the loss of stability about an equilibrium point. The amount of energy extractable by a reciprocating device depends on its aeroelastic response, and on the underlying physical tenets of the flutter.

Indeed different flutter types exist, specifically coupled and stall. The difference in behaviour between both types of flutter is still not well understood, specifically in the non-linear regime. Due to the non-linear behaviour of stall flutter, and LCOs in general, analytical solutions are limited. Therefore, studies exploring LCO behaviour due to flutter are for the most part limited to experimental investigations. The study in this thesis investigates the energy extraction potential and aeroelastic response of stall flutter and coupled flutter induced LCOs. Experiments were conducted using the aeroelastic rig located at the large recirculating wind tunnel at RMC. The responses from two different elastic axis locations were recorded, with varying frequency ratios and increasing Reynolds numbers for each. The steady state LCO responses in pitch and heave were recorded using rotary potentiometers.

The highest efficiency values were found to be produced by coupled flutter induced LCOs. Although further investigation is required, the results suggest that the degree of structural coupling between two degrees of freedom influences the aerodynamic efficiency of a reciprocating device. Both types of flutter produced LCO trends that varied with frequency ratio. Both types of flutter induced LCOs also produced well-behaved oscillations for certain configurations which resembled Simple Harmonic Motion (SHM). For frequency ratios away from one, the two-degree-of-freedom stall flutter induced LCO response closely follows the one-degree-of-freedom case. For these cases, the pitch motion drives the heave motion. Stall flutter LCO responses for frequency ratios close to one experienced a resonance-like phenomenon resembling lock-in phenomenon.

# Résumé

L'énergie générée par le mouvement de l'atmosphère terrestre est estimée d'être en centaines de terrawatts. En conséquence, la production d'énergie éolienne a suscité un intérêt particulier. Le facteur de coût élevé, la nécessité de hautes tours, les problèmes de bruit, la menace pour les oiseaux des éoliennes à axe horizontal, ainsi qu'une curiosité en ingénierie, ont motivé le développement des éoliennes alternatives. Cette recherche se concentre sur l'extraction d'énergie à partir de profils aérodynamiques en mouvement oscillants alternatifs, car il y a de l'énergie disponible pour être extraite de l'écoulement à travers les oscillations à cycle limite (LCO) induits par le flottement. Le flottement est un phénomène aéroélastique résultant généralement de la perte de stabilité autour d'un point d'équilibre. La quantité d'énergie extractible par une éolienne alternative dépend de sa réponse aéroélastique, et sur les principes physiques sous-jacents du flottement.

Deux types de flottement existent, précisément le flottement par couplage et le flottement de décrochage. La différence entre les deux types de flottement n'est pas encore bien comprise, particulièrement dans le régime non linéaire. Les solutions analytiques pour les LCO induits par le flottement sont limitées, en raison du comportement non-linéaire inhérent. Par conséquent, les études explorant le comportement des LCO dues au flottement sont limitées à des investigations expérimentales pour la plupart. L'investigation menée dans cette thèse entrevoit le potentiel d'extraction d'énergie et le comportement aéroélastique des LCO induites par le flottement par couplage et le flottement de décrochage. Des expériences ont été menées dans la grande soufflerie à recirculation du CMR. Les réponses provenant de deux emplacements d'axes élastiques différents ont été notées, avec des rapports de fréquence et des nombres de Reynolds variables pour chacun. Les réponses du tangage et du pilonnement de LCO ont été enregistrées à l'aide de potentiomètres rotatifs.

Les valeurs d'efficacité les plus élevées se sont révélées être produites par des LCO induites par flottement couplés. Plus d'études sont nécessaires, mais les résultats préliminaires suggèrent que le degré de couplage structural entre deux degrés de liberté influence l'efficacité aérodynamique d'une éolienne alternative. Les deux types de flottement ont produit des tendances de LCO variant avec le rapport de fréquence. Les deux types de LCO induits par le flottement produisaient également des oscillations qui se comportaient bien pour certaines configurations qui ressemblaient des oscillations harmoniques. Pour les rapports de fréquence qui n'égalent pas un, la réponse LCO de flottement de décrochage à deux degrés de liberté ressemble au comportement produit par un degré de liberté. Pour ces cas, le mouvement de tangage entraîne le mouvement de pilonnement. Les réponses LCO du flottement de décrochage pour des rapports de fréquence proches d'un ont présenté un phénomène de résonance ressemblant à un phénomène d'accrochage.

# Acknowledgements

Wing Flapping About

Wow! Violent Oscillations!

Energy Exists

# Table of Contents

# Nomenclature

| Abbreviations | Definition |
|---|---|

AC ............................................................................................................... Aerodynamic Centre

AoA .................................................................................................................... Angle of Attack

CG ..................................................................................................................... Centre of Gravity

EA ........................................................................................................................... Elastic Axis

LCO ............................................................................................................. Limit Cycle Oscillation

LSB ......................................................................................................... Laminar Separation Bubble

SAO ......................................................................................................... Small Amplitude Oscillation

SHM ............................................................................................................. Simple Harmonic Motion

## Roman Symbols

$a_h$ ................................................................. Measurement between Mid-chord and Elastic Axis

$b$ ................................................................................................................. Airfoil Half-chord (m)

$c$ ................................................................................................................ Airfoil Chord Length (m)

$C(k)$ .............................................................................................................. Theodorsen Function

$D_h$ .............................................................. Heave Structural Damping Coefficient (kg•m$^2$/s)

$D_\theta$ .............................................................. Pitch Structural Damping Coefficient (kg•m$^2$/s)

$e$ ................................................................................................... Length from AC to the EA (m)

$f_n$ .................................................................................................. Structural Natural Frequency (Hz)

$f_s$ ................................................................................................................ Shedding Frequency (Hz)

$h$ ................................................................... Heave Motion Position with reference to the EA (m)

$\dot{h}$ ................................................................................................ Heave Rate of the EA (m/s)

$\ddot{h}$ .............................................................................. Heave Acceleration of the EA (m/s$^2$)

$h_{CG}$ ............................................................. Heave Motion Position with reference to the CG (m)

$I_{CG}$ .............................................................................. Moment of Inertia about CG (kg•m$^2$)

$I_{EA}$ ............................................................................. Moment of Inertia about the EA (kg•m$^2$)

$k$ ..................................................................................................................... Reduced Frequency

$K_h$ ................................................................................................ Stiffness of Heave Spring (N/m)

$K_\theta$ .............................................................................................. Total Pitch Stiffness (N/m•rad)

$\overline{KE}$ ............................................................................... Kinetic Energy per Oscillation Cycle (J)

$l$ ........................................................................................................................... Wing Span (m)

$L$ ...................................................................................................... Aerodynamic Lift Force (N)

$M_{AC}$ .......................................................................... Aerodynamic Moment about the AC (Nm)

## Greek Symbols

# Chapter 1 – Introduction and Background

## 1.1 Introduction

As the world population continues to grow exponentially, so does the demand for energy. The need to develop alternative, clean, sustainable, environmentally benign, and efficient forms of energy generation becomes increasingly imperative. In hopes of replacing environmentally costly fossil fuel generation, and moving toward more distributable energy resources, much effort has been undertaken to advance renewable energy technology. More specifically, since the power generated by the movement of the Earth's atmosphere is estimated to be hundreds of terrawatts, there has been particular interest in wind power generation. The high cost-factor, requirement for large towers, noise concerns, and threat to birds of horizontal-axis wind turbines has motivated the development of alternative methods to extract energy from the wind. Of these alternative methods are flapping, or reciprocating wind-turbines. These devices may have potential to operate efficiently in low flow-speeds and small scales, as well as maintaining a small profile compared to rotary mechanisms [1]. Although energy extraction from bluff bodies and flow induced vibration (FIV) are related flapping mechanisms, the focus of this research is on reciprocating airfoils.

Several numerical and experimental studies have investigated the aerodynamics and efficiency of reciprocating devices. The most notable of these investigations are reviewed in section 1.2. Qualitatively, the response of these reciprocating wing generators resembles flutter phenomenon [1]. The oscillatory motion of flutter is seemingly similar to the flapping of animals which propel themselves in fluid mediums. One crucial difference lies in the transfer of energy, where thrust-producing flapping transfers energy to the flow, whereas energy is transferred to a structure and its wake, from the flow in a flutter oscillatory mode [2]. If the work done by the non-conservative aerodynamic loads over one cycle is greater than the work done by the structural loads, then the oscillations are self-sustaining [3]. An interpretation of the difference in energy transfer between flutter (drag) and propulsive (thrust) modes is presented in Figure 1.1. The middle panel represents a system where the energy from excitations is shed into the wake and subsequent oscillations are damped out. Since there is energy available to be extracted from the flow by the structure through flutter, the potential for an alternative sustainable energy extraction mechanism exists through reciprocating motion based on aeroelastic phenomena.

Flutter is an aeroelastic dynamic phenomenon generally resulting from the loss of stability about an equilibrium point. Several types of aeroelastic dynamic phenomenon exist, including coupled (classical) flutter and stall flutter. Instabilities will arise at any airspeed above the critical flutter speed, when the overall damping of the system is less than or equal to zero [3]. If the critical flutter speed is reached, the aeroelastic system, a simple cantilever wing for example, will begin to initially oscillate with exponentially growing amplitude. Eventually, the oscillation of the wing will either reach a dynamic stable state, or it will break. This non-linear

dynamic stable state is defined as a Limit Cycle Oscillation (LCO), where the wing is predicted to oscillate at a constant amplitude resembling simple harmonic motion (SHM). Two general behaviours of LCO amplitude response with airspeed are presented by Dowell et al. [4]. These include the typical increase in LCO amplitude with increasing airspeed, the trend being affected by the degree of non-linearity. Another response includes the existence of LCOs below the flutter boundary if the disturbances are sufficiently large. The response for the second behaviour, presented on the right graph in Figure 1.2, shows a hysteresis where the appearance of LCO is path dependant and occurs for decreasing airspeeds below the flutter speed. In non-linear dynamics terminology, the flutter speed of the left-hand diagram is associated with a supercritical Hopf bifurcation, whereas the right-hand diagram contains a subcritical Hopf bifurcation.
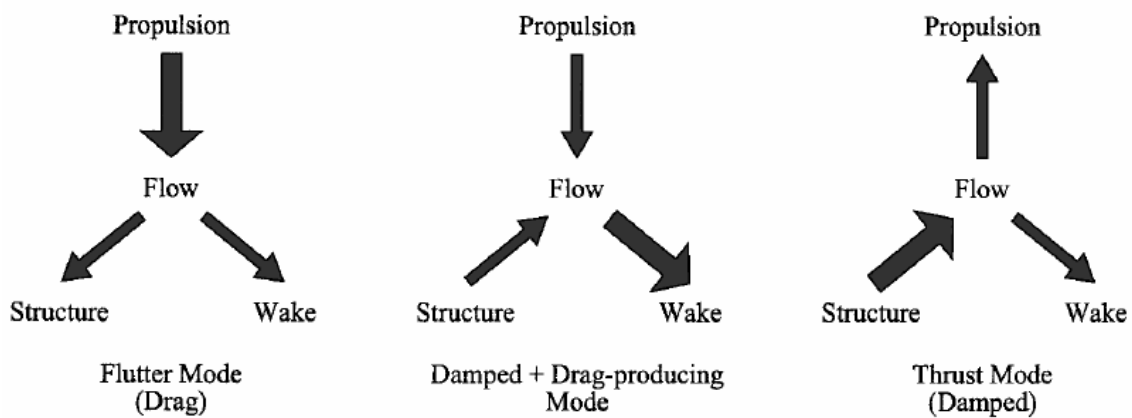


*Figure 1.2: Theoretical perspective of energy transfer mechanisms in aeroelasticity and flapping flight. Taken from [2].*
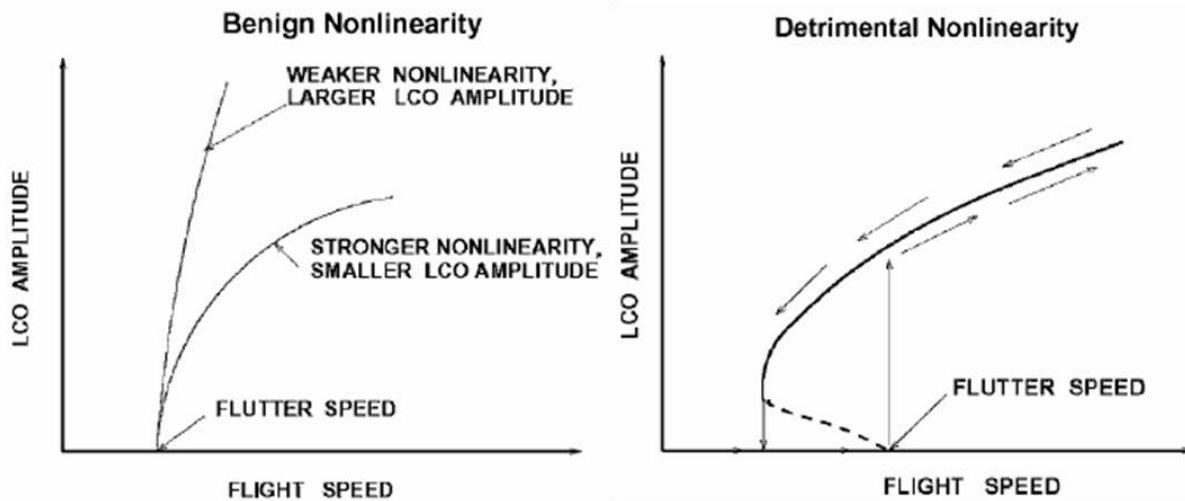


*Figure 1.2: Schematic of different types of LCO responses. Taken from [2]*

The non-linear effects that may influence an LCO response due to flutter may be either structural or aerodynamic. Structural non-linearities include spring hardening systems, large

deflection geometries and freeplay. Previous investigations have observed systems which stiffened in a cubic manner showed an increase in LCO amplitude with airspeed [4]. Aerodynamic non-linearities include shock motions at transonic airspeeds as well as separated flows. The non-linear effects of separated flow associated with the leading-edge vortex (LEV) becomes important at large oscillation amplitudes for all Reynolds numbers. Instantaneous enhanced lift can also occur as a result of complex non-linear viscous phenomena which have a significant impact on elastic airfoil behaviour [5]. Transitional Reynolds number effects, which occur for flows between $10^4 \leq Re_c \leq 10^6$, can become important for oscillations encompassing moderate angles of attack (AoAs). Within the transitional regime, strong variations in aerodynamic properties occur, as sometimes exemplified by a sharp increase in the lift-to-drag ratio with Reynolds number. Therefore, for large amplitude LCOs occurring within the transitional Reynolds number regime, both the shed LEV and sharp variations in aerodynamic properties will affect the aeroelastic response.

## 1.2 Review of Reciprocating Renewable Energy Devices

Conventional turbines based on rotational motion are designed to operate at high efficiencies while the flow remains attached to the blades. In contrast, flapping flight in nature has been observed to generate significantly higher instantaneous forces than can be achieved with attached flow. This occurs when the flow separates near the nose of the foil in the form of an LEV, thus exploiting the attending low pressure vortex core [1]. Subsequent attention has been given to alternative reciprocating wind turbines which mimic nature-inspired motion. The two types of reciprocating energy extraction devices defined in the most developed literature are based on prescribed motion in pitch. They are "kinematically-constrained" and "kinematically-passive" mechanisms, as listed by Kinsey and Dumas [6]. Kinematically-constrained systems comprise of a mechanical coupling mechanism between the pitch and heave motions. The prescribed oscillating pitch motion creates an oscillating fluid dynamic force on a foil which heaves in response. A kinematically-passive system is free to oscillate in two degrees-of-freedom (2DOF), and is dictated by the system's inherent structural and aerodynamic properties.

The first most notable development on reciprocating designs for energy extraction from a flow occurred in 1981 by McKinney and DeLaurier [7]. Their creation, the Wingmill, was an "oscillating-wing windmill" which used prescribed SHM in pitch and heave to extract energy from the airflow. Figure 1.3 includes a picture of their prototype. The purpose of their work was to determine the feasibility and efficiency of an oscillating kinematically-constrained reciprocating device, as opposed to a traditional rotary wind turbine. The whole wing-span oscillated in coupled pitch and heave, with a constrained phasing between the pitch and heave oscillations. While it is not entirely clear whether the pitch oscillations are imposed, a small electric DC motor is used to change the relative angle between portions of the horizontal shaft controlling the phase angle. The experimental apparatus consisted of a NACA 0012 wing with

constant profile, where heaving motion was translated into rotational motion. The pivot point was located at the mid-chord, rigidly attached to the vertical support shaft. Wind tunnel tests were conducted between $4.34 \times 10^5 \leq Re_c \leq 5.6 \times 10^5$ (6.2 m/s $\leq U_\infty \leq$ 8 m/s). The heave amplitude was held constant, while the pitch amplitude and phase angles could be varied.

The aerodynamic forces measured from their experiment were compared to those estimated using linear equations for incompressible and non-separated flow. Relative angles of attack during oscillations were found to exceed predicted static stall angles. Hysteresis effects were observed to occur in the obtained mechanical power for increasing and decreasing phase angles, and were attributed to dynamic stall effects. The theoretical calculated power values were seen to be consistently greater than experimental ones for smaller phase angles. From their tests, the maximum aerodynamic efficiency was found to be 16.8%, for a pitching amplitude of 30° and a Reynolds number of $5.6 \times 10^5$ ($U_\infty$ = 8 m/s). The study demonstrated that the concept of a reciprocating motion wind turbine was physically realizable at producing efficiencies comparable to conventional wind-turbines at the time.
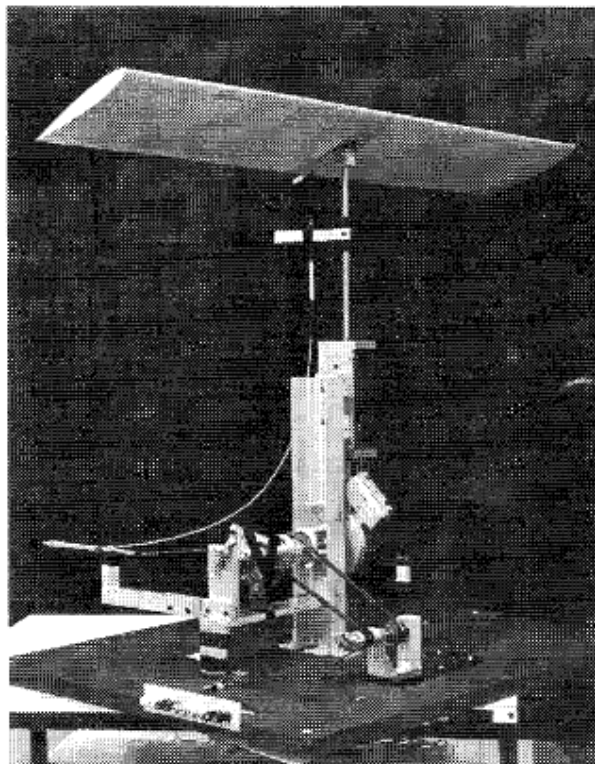


*Figure 1.3: Photo of complete Wingmill experimental model. Taken from [7]*

In 2008, Kinsey and Dumas numerically simulated the energy extraction capabilities of a two-dimensional NACA 0015 airfoil in laminar flow. The simulations used a viscous Navier-Stokes solver for a Reynolds number of $1.1 \times 10^3$, with prescribed sinusoidal motion in pitch and heave [8]. The authors defined two operating regimes based on the SHM quasi-steady flow assumptions. The derived expression differentiates between the two modes of energy transfer,

whether power is expended or extracted from the flow. Based on the timing, or phase, between the pitch and heave motions, the resultant force is either thrust or drag based. This is illustrated in Figure 1.4, where the direction of the horizontal force $X$ dictates energy extraction or expenditure. The direction of $X$ depends on the timing and direction of the AoA $\alpha$, the aerodynamic lift $L$ and drag $D$ and the resultant force $R$. This expression, presented in Equation 1.1, defines a 'feathering parameter' $\chi$. If $\chi > 1$, it can be inferred that the vertical component of force $Y$ would typically be in the same direction as the vertical displacement of the airfoil, and power can be extracted from the flow. The symbols used for SHM in their study are shown in Figure 1.5, where $\theta_0$ represents the pitching amplitude, $H_0$ the heaving amplitude, and $\omega$ the circular frequency of oscillation.

$$\chi = \frac{\theta_0}{\tan^{-1}(H_0\omega/U_\infty)} \qquad [1.1]$$

While various definitions for the aerodynamic efficiency of a flapping mechanism exist in literature, the definition used by Kinsey and Dumas calculates the power available through the flux of kinetic energy flowing through the total swept area by any part of the airfoil motion [6], as illustrated in Figure 1.5. The aerodynamic efficiency is thus calculated as the ratio of the cycle-averaged power with reference to the power available in the flow. The phase between the pitch and heave was kept at a constant 90° for the Navier-Stokes solver simulations, to ensure a feathering parameter above 1 and extraction of energy from the flow. A maximum efficiency of 34% was found to occur at non-dimensional frequencies of 0.13 - 0.17 ($f^* = f\ c/U_\infty$), for pitch amplitudes above 75° and heave amplitudes of one chord-length, where the elastic axis is located at one-third the chord length. The visualizations obtained from the simulations indicated that the vortices produced from leading-edge separation, due to large oscillation amplitudes, had a strong influence on efficiency [8].

An experimental set-up based on the parameters which produced the maximum efficiency obtained of 34% was designed and built by the authors in subsequent investigations. The mechanism was capable of being driven by one or two airfoils, where the pitch motion was connected to a four-link mechanism. This reciprocating mechanism was translated into rotational motion, connected to a driving rotating shaft which turned a speed-controlled electric generator. The generator imposed a frequency $f$ through a proportional-integral-derivative (PID) controller. The generator ran as a motor for the parts of the cycle where power was not extracted from the flow. Imposing the frequency of oscillation, the heave ($H_0$) and pitching ($\theta_0$) amplitudes were prescribed through the mechanism. A first prototype of this design was built and tested at the Laval University wind-tunnel, as shown in Figure 1.6 [9]. A second prototype was mounted underneath a pontoon boat driven by an outboard motor, and tested in a local lake. The maximum aerodynamic efficiency was found to be 30% for one airfoil, and 40% for two airfoils in tandem.
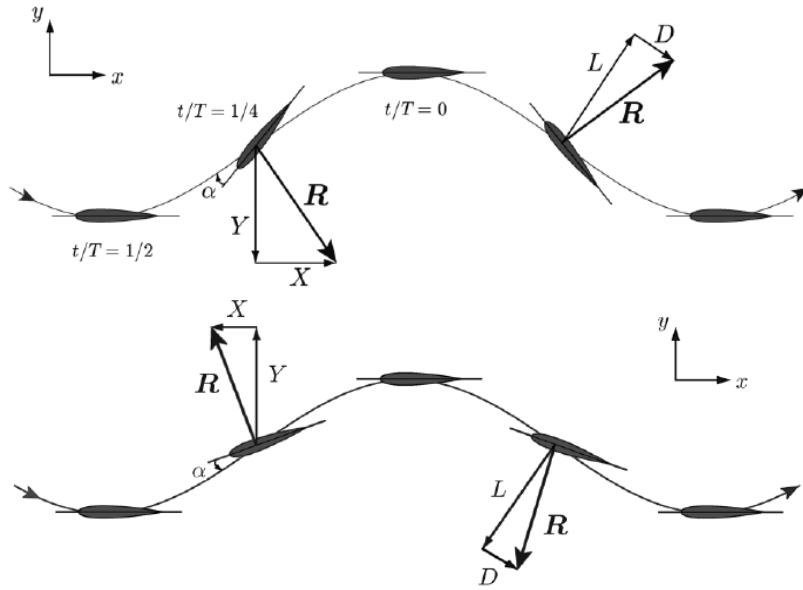
*Figure 1.4: Resultant forces of oscillations, energy extracting or drag (top), and thrust mode (bottom). Taken from [8].*
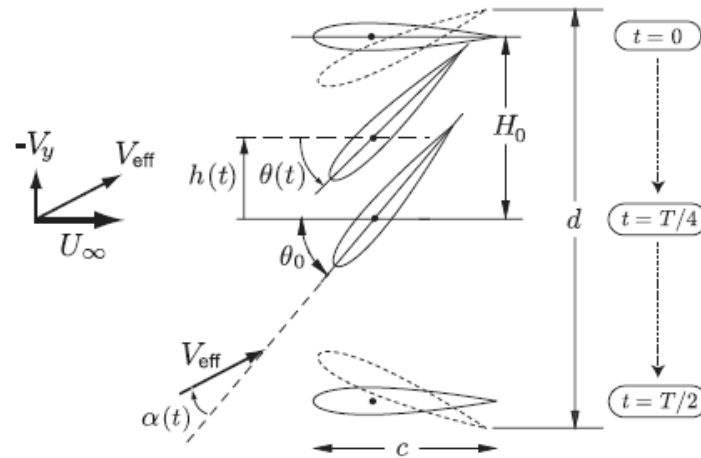


*Figure 1.5: Schematic taken from in Kinsey and Dumas, 2014 for the definition of total swept area, with a phase lag in pitch of 90°.*

*Figure 1.6: The reciprocating tandem-wing experimental prototype in the wind-tunnel at Laval University. Taken from [9].*

In 2010, Platzer et al. a study at the Naval Postgraduate School in Monterey California, on flapping wing energy extraction technology [10]. Similar to the studies done at Laval University, simulations were performed for prescribed sinusoidal motion of single and tandem NACA 0014 airfoils at a Reynolds number of $2.0\times10^4$, with a pitch amplitude of 73°, and a heave amplitude of 1.05 chord-lengths. The Computational Fluid Dynamics (CFD) package Fluent was used, with an unsteady incompressible solver. The simulations were comparable with the numerical results presented by Kinsey and Dumas, where the peak simulated efficiency was calculated to be 34%, for a single airfoil configuration with phase angles from 90° to 110° between the pitch and heave motions. It was discussed that if the heaving motion is always in the same direction as the aerodynamic lift, which implies a phase angle ∈(0°, 180°) between the pitch and heave motions. Work is then done by the air on the airfoil throughout one cycle [3].

An experimental analysis was conducted, where several prototypes were investigated. One notable prototype involved a swinging arm supported by a bearing, with restricted heave displacement. An L-shaped moment arm was used to reverse the pitch angle when it touched the stoppers. No motor was involved, the mechanism is totally free to oscillate, yet mechanically constrained. The pitching axis was located aft of the mid-chord, ensuring the foil to be statically unstable so that it would deflect to an increasing pitch angle until it was stopped by a mechanical restraint. As observed in Figure 1.7, a stroke-reversal is induced as the airfoil starts to rotate in the counter-clockwise direction. As a result, the lift is generated in the opposite direction, and the airfoil starts to slide. A square-wave type oscillation is thus generated. This prototype was designed to operate in water, and was tested in a water tunnel with flow speeds ($U_\infty$) ranging from 0.2 to 0.5 m/s, and up to 1 m/s in a towing tank.
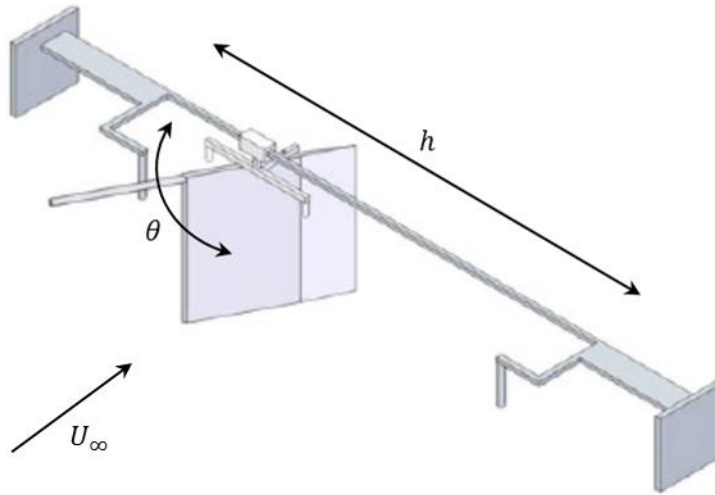
*Figure 1.7: Schematic of prototype tested by Platzer et al., adapted from [10]*

The numerical study by Kinsey and Dumas was repeated in 2014 for a Reynolds number of $5.0 \times 10^5$ using a two-dimensional Unsteady Reynolds Averaged Navier-Stokes (URANS) solver [6]. The maximum efficiency calculated was 43%. No correlation between LEVs and efficiency was found for the transitional Reynolds number case. In 2017, a similar study was conducted by the same group. The parameters of a fully-passive flapping NACA 0015 airfoil, with an elastic axis at a third the chord length, were varied in order to increase its aerodynamic efficiency at a Reynolds number of $5.0 \times 10^5$ [11]. The structural model was defined by an elastic airfoil in 2DOF, inspired by the aeroelastic rig used at the Royal Military College of Canada (RMC). Both pitch and heave motions are defined by the fluid-structure interaction between the structure and the aerodynamic loads. The fluid dynamics is simulated using a Boussinesq eddy-viscosity approximation in a Spalart-Allmaras URANS model, performed in the open-source CFD program *OpenFOAM-2.1x*. The parameters were varied until the values for oscillation amplitude, frequency, and aerodynamic efficiency matched their kinematically-constrained device. The maximum efficiency value obtained from simulations was 33.6%, indicated by the authors to show good potential for the use of fully-passive airfoils for energy extraction. From the simulated flow visualizations, it was inferred that the moments associated with airfoil-vortex interaction limited the oscillation amplitude, as well as improved power extraction from the flow. It was argued that the physical mechanism driving the LCOs was stall flutter due to the importance of large leading-edge stall vortices during periodic oscillations. Further discussion on the dynamics of the system to support this claim was not included.

While the oscillations produced by simulated prototype reciprocating energy devices are SHM, kinematically resembling flutter induced LCOs, the underlying aeroelastic nature of each study remains unclear. Much of the reciprocating device studies have focussed on simulating the resulting unsteady viscous flow, rather than on the overall dynamics of the fluid structure

interaction. Effort has been taken by previous numerical studies to understand the timing and influence of these shed leading-edge vortices on the aerodynamic efficiency. Different aeroelastic phenomenon may resemble each other qualitatively, however may have fundamentally different underlying physics that are defined by the properties of the structure. While Veilleux and Dumas argue that the vortical structures occurring from large amplitude LCOs are due to stall flutter, the same type of leading-edge separation behaviour may occur in large amplitude LCOs induced by coupled flutter [11]. Further analysis of the overall dynamics of the structure is required in order to understand the entire aeroelastic system. Since kinematically-passive devices are dependent on aeroelastic phenomena in order to extract energy from the flow, it stands to reason that a more thorough understanding of the overall dynamics may potentially lead to energy extracting devices with higher aerodynamic efficiencies.

## 1.3 Objectives

Since there is energy available to be extracted from the flow through dynamic aeroelastic instability, the potential for an alternative renewable energy extraction mechanism exists. Previous studies of reciprocating wind turbine devices have observed overall efficiencies to be up to 40%, which is comparable to traditional horizontal axis wind-turbines (HAWTs) [9]. Although the simulated and experimental studies for kinematically-constrained and kinematically-passive reciprocating wind turbines show promising results, a proper understanding of the underlying dynamics in these studies is missing. While the underlying physics for prescribed systems using SHM are different than an airfoil undergoing LCOs, a comparison of these aeroelastic systems remains to be explored. Gaining a more complete comprehension of how the energy transfer differs between aeroelastic phenomenon may improve the potential for increased energy extraction from a fluid flow. Due to the inherently non-linear nature of both coupled flutter and stall flutter induced LCOs, analytical solutions describing their response do not exist. Therefore, investigations exploring the difference in the energy extraction potential between different types of flutter induced LCOs are reliant on experiment.

In comparison to coupled flutter, there are a limited amount of studies investigating the behaviour of stall flutter. Therefore, it is of interest to further investigate how the physical behaviour of stall-flutter-induced large amplitude LCOs differs from other aeroelastic phenomena, specifically coupled flutter induced LCOs. Aeroelastic measurements within the transitional Reynolds number range at RMC to date have focussed on SAOs due to LSB behaviour [12-16]. Poirel and Mendes observed large amplitude LCOs due to coupled flutter, and 2DOF SAOs coexisting for the same flow conditions, for a NACA 0012 oscillating about an elastic axis set at 18.6% of the chord-length. While large amplitude symmetric LCOs in 1DOF were experimentally observed at RMC by Harris in 2007, and Mendes in 2016 for a NACA 0012 airfoil pitching about 35% the chord-length, the study conducted by Peristy et al. focussed on 1DOF LCOs due to stall flutter. The current investigation follows the work of Mendes, Peristy et

al., and expands on the work by the author (Goyaniuk et. al), who noted symmetric 1DOF SAOs and 1DOF LCOs due to stall-flutter coexisting as competing stable attractors [16-18].

Therefore, one objective of this thesis is to deepen the understanding of the differences in the physics between coupled flutter and stall flutter LCOs, the analysis will involve observing the sensitivity of the response to varying frequency ratios about one, and increasing Reynolds numbers. While deepening the physical understanding of different aeroelastic phenomena, one can determine the energy extraction potential of each. Another main objective is comparing which aeroelastic instability, stall flutter or coupled flutter, is more aeroelastically efficient in terms of energy extraction. Finally, it is the hope of the author that the results from this study may assist in determining the optimal configuration for a passive reciprocating device. The thesis is organized as follows. The remainder of Chapter 1 will present related analytical models, as well as relevant aeroelastic phenomena in more detail. The LCOs induced by coupled flutter are presented in Chapter 3, while Chapter 4 discusses stall flutter. Chapter 5 compares both types of flutter LCOs.

## 1.4 Linear Aeroelastic Systems

### 1.4.1 Two-Degree-of-Freedom Equations of Motion

An elastically mounted, 2DOF kinematically passive airfoil is described by structural damping and stiffness terms acting at the elastic-axis (EA). In the context of linear aerodynamics, the system can respond in pitch and heave to aerodynamic loads acting at the aerodynamic centre (AC). For a thin, symmetrical airfoil with span $l$ and constant chord, thin airfoil theory is assumed such that the aerodynamic centre is estimated to be located at the quarter-chord point assuming small displacements. The inertially coupled linear equations of motion derived from Lagrange's method are shown in Equations 1.2 and 1.3, modelled as a mass-spring-damper system. The free-body diagram with geometric and structural parameters is shown in Figure 1.8 with the coordinate system used in this study indicated. The structural mass, damping and stiffness terms are constants, while the pitch and heave position, velocity an acceleration terms are variable in time. For steady models, the lift and moment do not vary in time. Linear quasi-steady and unsteady model the lift as time dependant variables.

$$M_h \ddot{h} - \frac{M_\theta c x_\theta}{2} \ddot{\theta} + D_h \dot{h} + K_h h = L \qquad [1.2]$$

$$I_{EA} \ddot{\theta} - \frac{M_\theta c x_\theta}{2} \ddot{h} + D_\theta \dot{\theta} + K_\theta \theta = M_{EA} \qquad [1.3]$$
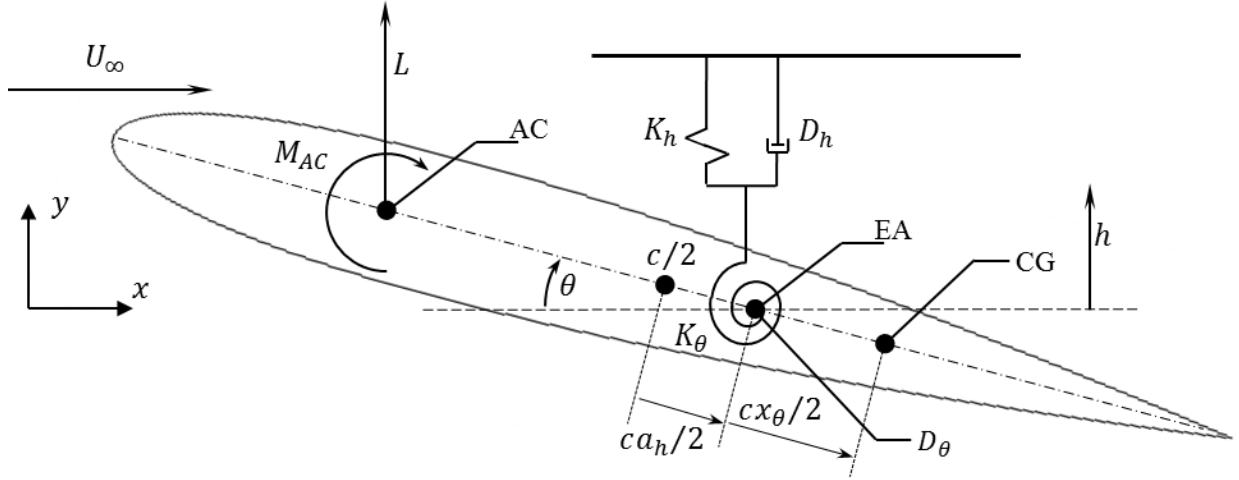
*Figure 1.8: A schematic of a two-dimensional, thin, symmetrical airfoil with degrees of freedom in bending and torsion.*

## 1.4.2 Steady One-Degree-of-Freedom Aerodynamic Moment

The steady aerodynamic loads on an airfoil are treated as constant for a given angle of attack subject to incompressible and attached flow. Considering only the steady aerodynamics in one-degree-of-freedom (1DOF), the representation of an airfoil with torsional stiffness $K_\theta$ about the EA is reduced to the schematic shown in Figure 1.9. The aerodynamic moment about the EA can be related to the lift and moment at the AC based on Equation 1.4. The aerodynamic centre, the location where the aerodynamic moment is independent of the angle of attack (AoA), is assumed to be at the quarter-chord point. Equation 1.4 is derived assuming small angles, thin-airfoil theory, incompressible attached flow, and a symmetrical airfoil.

$$M_{EA} = eL + M_{AC} \qquad [1.4]$$

where $e$ can also be represented in Equation 1.5, with $c$ being the chord length and $a_h$ the non-dimensional distance between the EA and the mid-chord:

$$e = \frac{c}{2}\left(\frac{1}{2} + a_h\right) \qquad [1.5]$$

Given that the aerodynamic moment $M_{AC}$ about the AC is zero for a symmetrical airfoil, the equation for the moment about the elastic axis of an airfoil can be reduced to:

$$M_{EA} = eL = e\frac{C_L}{2}\rho U_\infty{}^2 cl = \left[e\rho U_\infty{}^2 bl2\pi\right]\theta \qquad [1.6]$$

where $b = c/2$ and $C_l = 2\pi\theta$, and the AoA and pitch values are assumed to be equal to each other. Considering only the static terms in the equation of motion 1.3, the total static aeroelastic

stiffness can be expressed in Equation 1.7. One can see that if the location of the elastic axis is aft of the AC, its value being positive, the total aeroelastic stiffness decreases with increasing airspeed. The stability of the static term is discussed more thoroughly in section 1.5.1.

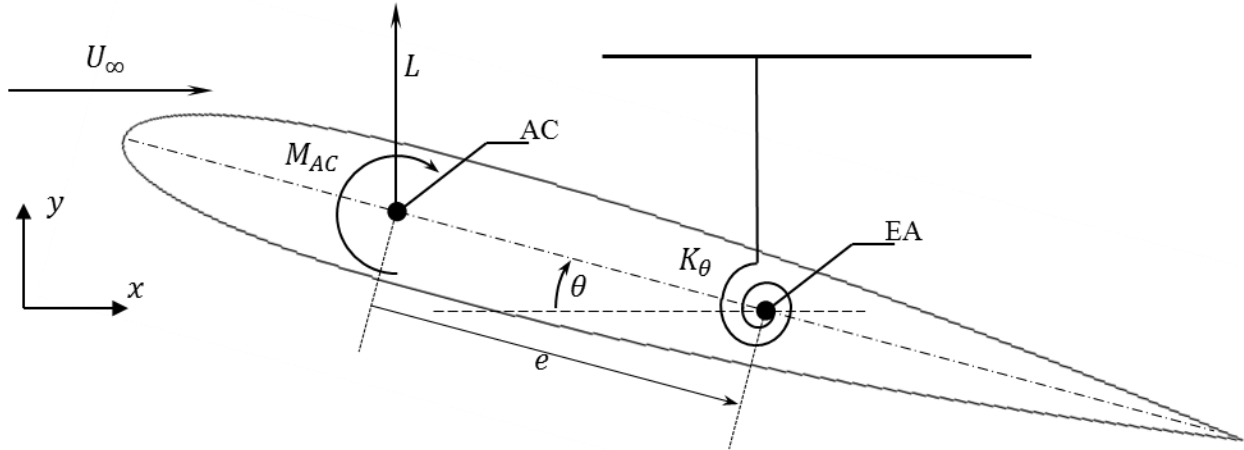$$\left[K_\theta - e\rho U_\infty{}^2 bl2\pi\right]\theta = 0 \qquad [1.7]$$



*Figure 1.9: Representation of a symmetrical elastic airfoil free to rotate in torsion*

### 1.4.3 Quasi-Steady Aerodynamics in Two Degrees-of-Freedom

Quasi-steady aerodynamics build on the classic steady model. The quasi-steady assumption dictates that at any instant in time, the steady aerodynamic loads occurring at a constant velocity in pitch and heave apply to the instantaneous values on an airfoil undergoing unsteady motions [3]. It is important to note, that the aerodynamic model is linear, and that there is no time lag between the airfoil motion and the associated loads. The aerodynamics are assumed to adjust to the airfoil motion instantaneously.

The instantaneous lift $L$ can be accounted for from the steady equation from thin-airfoil theory approximations in two dimensions, with span $l$:

$$L = \rho U_\infty{}^2\, cl\pi \alpha_{3c/4} \qquad [1.8]$$

The local AoA at $3c/4$ is used in this model, to represent the effective AoA experienced by the heaving and pitching airfoil. This effective AoA takes into account the resultant velocity due to translation $\dot{h}$ and rotation $\frac{1}{2}c(\frac{1}{2} - a_h)\dot{\theta}/2$, and is expressed in Equation 1.9 [3].

$$\alpha_{3c/4} = \theta - \frac{\dot{h}}{U_\infty} + \frac{c(\frac{1}{2}-a_h)}{2U_\infty}\dot{\theta} \qquad [1.9]$$

12

The quasi-steady lift is thus represented as:

$$L = \rho U_\infty{}^2 c l \pi \left[ \theta - \frac{\dot{h}}{U_\infty} + \frac{c(\frac{1}{2}-a_h)}{2U_\infty} \dot{\theta} \right] \qquad [1.10]$$

In addition to an induced AoA, the pitching motion induces a non-zero moment coefficient about the aerodynamic centre $C_{M_{AC}}$. This is represented by a damping couple proportional to the angular velocity [3].

$$C_{M_{AC}} = -\frac{\pi c}{8U_\infty} \dot{\theta} \qquad [1.11]$$

Where,

$$M_{AC} = \frac{\rho U_\infty{}^2}{2} c^2 l C_{M_{AC}} \qquad [1.12]$$

Substituting the terms in equations 1.10 and 1.13 into equation 1.4 defined earlier, the quasi-steady moment can be defined as:

$$M_{EA} = e\rho U_\infty{}^2 c l \pi \left[ \theta - \frac{\dot{h}}{U_\infty} + \frac{c(\frac{1}{2}-a_h)}{2U_\infty} \dot{\theta} \right] - \frac{\rho U_\infty}{16} c^3 l \pi \dot{\theta} \qquad [1.13]$$

## 1.4.4 Unsteady Aerodynamics

While computationally simple, the quasi-steady model fails to take the fluid inertia (added mass) as well as circulation history into account. The added mass terms represent the force that acts opposite to the acceleration of the airfoil. This term is considered the non-circulatory contribution to the unsteady aerodynamic loads, since it is independent of the viscous effects embodied by circulation. The *nc* subscripts in Equations 1.14 and 1.15 indicate the non-circulatory components of the aerodynamic lift and moment. For an airfoil undergoing pitch and heave motions in 2DOF, the added mass contributions in unsteady lift and moment are expressed as [3]:

$$L_{nc} = b^2 l \rho \pi \left[ -\ddot{h} + U_\infty \dot{\theta} - b a_h \ddot{\theta} \right] \qquad [1.14]$$

$$M_{EA,nc} = b^2 l \rho \pi \left[ -b a_h \ddot{h} - U_\infty b \left( \frac{1}{2} - a_h \right) \dot{\theta} - b^2 \left( \frac{1}{8} + a_h{}^2 \right) \ddot{\theta} \right] \qquad [1.15]$$

Modelling the circulatory unsteady forces acting on an airfoil undergoing periodic oscillations (or arbitrary motions) in non-separated and incompressible flow has been investigated by Wagner, Theodorsen, Küssner, von Kármán, Sears, and others [3]. The analysis of these forces is based on conceptualizing a continuous sheet of vorticity that is convected from

the trailing edge into the wake. In Wagner's problem, this vorticity arises from the growth of circulation when an airfoil undergoes an impulsive start from rest to a uniform velocity $U_\infty$. A vortex is shed from the trailing edge, and induces a vertical component of velocity in the flow. This induced velocity is known as downwash, and it is known to diminish the AoA of the airfoil, hence lift. The effect of the shed vortex is strongest when the vortex is at the trailing edge of the airfoil, its influence diminishing as it moves further downstream with velocity $U_\infty$.

The effects of aerodynamic lag and unsteadiness become more significant when the airfoil oscillates at high frequencies. The importance of unsteady effects can thus be evaluated from the reduced frequency, expressed in Equation 1.16. The oscillation frequency is represented by $\omega$. It is generally understood that unsteady effects become important for $k > 0.05$. For $k < 0.05$, unsteady effects are much less prevalent, and the flow can be modelled with a quasi-steady model.

$$k = \frac{\omega b}{U_\infty} \qquad [1.16]$$

The time-dependant effect of the shed trailing edge vortex on the lift can be described by Wagner's function $\varphi(\tau)$ [3]. The value of the function is represented in Figure 1.10 as an aerodynamic lag. Wagner's function quantifies the build-up of circulation resulting from an instantaneous finite change in freestream airspeed, and subsequent diminished lift. As can be observed in Figure 1.10, the amount by which the circulation reduces the overall lift decreases with time, as the airfoil moves upstream from the shed trailing edge vortex. The circulatory component of unsteady lift can therefore be represented by including Wagner's function with steady lift from thin-airfoil theory.

$$L_c = \frac{\rho U_\infty^2}{2} \, cl2\pi\theta\varphi(\tau) \qquad [1.17]$$

$$\tau = U_\infty t / b \qquad [1.18]$$

An approximate expression for Wagner's function was developed by R.T. Jones, represented below, where the constant $A_1$ and $A_2$ are equal to 0.165 and 0.335, and $B_1$ and $B_2$ are equal to 0.0455 and 0.3 respectively [3].

$$\varphi(\tau) = 1 - A_1 e^{-B_1\tau} - A_2 e^{-B_2\tau} \qquad [1.19]$$

Expanding on this model, one considers the infinitesimal discrete vortices in a conceptual vorticity sheet. If the change in angle of attack is infinitesimal, the shed vortex is infinitesimally small and the subsequent influence on the circulatory lift infinitesimal as well. A small increment in circulation will result in an incremental change in the downwash at the three-quarter-chord point $dw_{3c/4}$, and subsequent increment in lift $dL_c$. Downwash is created when a vortex leaves the trailing edge, it induces a downwards component of velocity on the flow, and diminishes the lift created, and therefore the AoA of the airfoil.
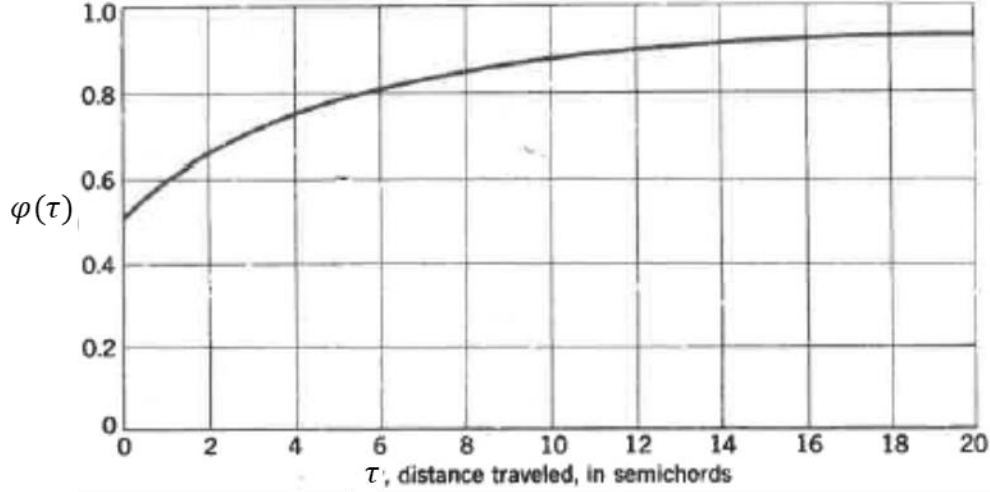
14

*Figure 1.10: Wagner's function for an incompressible fluid, adapted from [3]*

Wagner's function can thus be generalized into arbitrary airfoil motion by using the superposition principle (in the form of Duhamel's integral). The summation is represented below, and is valid for a linear aerodynamic model.

$$\mathrm{d}L_c = \frac{\rho U_\infty^2}{2} cl2\pi\varphi(t - t_0)\mathrm{d}w_{3c/4}(t_0) \tag{1.20}$$

$$L_c = \frac{\rho U_\infty^2}{2} cl2\pi\left[w_{3c/4}(0)\varphi(t) + \int_0^t \varphi(t - t_0)\frac{\mathrm{d}w_{3c/4}(t_0)}{\mathrm{d}t_0}\mathrm{d}t_0\right] \tag{1.21}$$

Determining the stability of a dynamic aeroelastic system involves solving for the complete set of differential equations of motion. In order to solve for the aerodynamic lag, a third degree of freedom can be introduced for use in a given aeroelastic model. This third degree of freedom is aerodynamic rather than structural, and considers unsteady effects. Developed by Poirel in 2001 [19], the downwash at the three-quarter-chord point can be represented by the aerodynamic states $z$ and $\dot{z}$.

$$\ddot{z} + (b_1 + b_2)\dot{z} + b_1 b_2 z = w_{3c/4} \tag{1.22}$$

where $b_1$ and $b_2$ are represented by $b_1 = B_1 U/b$ and $b_2 = B_2 U/b$. Implementing this third-degree of freedom into the derived Equation 1.21, the unsteady lift and moment due to the circulatory terms can be represented by the Equations 1.23 and 1.24.

$$L_c = \rho U_\infty bl2\pi\left[(1 - A_1 - A_2)w_{3c/4} + \dot{z}(A_1 b_1 + A_2 b_2) + zb_1 b_2(A_1 + A_2)\right] \tag{1.23}$$

$$M_{EA_c} = \rho U_\infty b^2 l2\pi(a_h + 0.5)\left[(1 - A_1 - A_2)w_{3c/4} + \dot{z}(A_1 b_1 + A_2 b_2) + zb_1 b_2(A_1 + A_2)\right] \tag{1.24}$$

where the downwash term is defined in [3] as:

$$w_{3c/4} = U_\infty\theta - \dot{h} + \dot{\theta}b\left(\frac{1}{2} - a_h\right) \tag{1.25}$$

15

Adding both added mass and circulatory terms, the total unsteady lift and moments are represented as follows.

$$L = b^2 l \rho \pi \left[ -\ddot{h} + U_\infty \dot{\theta} - b a_h \ddot{\theta} \right] +$$

$$\rho U_\infty b l 2\pi \left[ (1 - A_1 - A_2) w_{3c/4} + \dot{z}(A_1 b_1 + A_2 b_2) + z b_1 b_2 (A_1 + A_2) \right] \qquad [1.26]$$

$$M_{EA} = b^2 l \rho \pi \left[ -b a_h \ddot{h} - U_\infty b \left( \frac{1}{2} - a_h \right) \dot{\theta} - b^2 \left( \frac{1}{8} + a_h^2 \right) \ddot{\theta} \right] +$$

$$\rho U_\infty b^2 l 2\pi \left( a_h + \frac{1}{2} \right) \left[ (1 - A_1 - A_2) w_{3c/4} + \dot{z}(A_1 b_1 + A_2 b_2) + z b_1 b_2 (A_1 + A_2) \right] \qquad [1.27]$$

An alternative unsteady model which takes also into account the added mass and circulatory terms is Theodorsen's function, which models the frequency domain rather than the time domain [3]. Theodorsen's function can be decomposed into real and imaginary functions of the reduced frequency.

$$C(k) = F(k) + iG(k) \qquad [1.28]$$

The overall function can be approximated as,

$$C(k) = 1 - \frac{A_1 ik}{ik + B_1} - \frac{A_2 ik}{ik + B_2} \qquad [1.29]$$

For a wing undergoing SHM in pitch and heave, the lift and moment can be represented linearly by both the added mass and Theodorsen's function for the circulation term. Equation 1.25 is used for the downwash term.

$$L = b^2 l \rho \pi \left[ -\ddot{h} + U_\infty \dot{\theta} - b a_h \ddot{\theta} \right] + \rho U_\infty b l 2\pi w_{3c/4} C(k) \qquad [1.30]$$

$$M_{EA} = b^2 l \rho \pi \left[ -b a_h \ddot{h} - U_\infty b (0.5 - a_h) \dot{\theta} - b^2 (1/8 + a_h^2) \ddot{\theta} \right] +$$

$$\rho U_\infty b^2 l 2\pi (a_h + 0.5) w_{3c/4} C(k) \qquad [1.31]$$

These two equations are not mathematically consistent since $C(k)$ is in the frequency domain, and $h$ and $\theta$ are expressed in the time domain. However, it is implicit that the motion is harmonic.

## 1.5 Aeroelastic Phenomenon

Several types of aeroelastic phenomena exist, including static and dynamic instabilities. Each have fundamentally differing underlying physics. Of the dynamic instabilities for example, there are two important different types of flutter. These are coupled (classical or coalescence) flutter, and stall flutter. Coupled flutter occurs as a result of the coupling of two degrees of

freedom (e.g. heave and pitch), and is inherently a linear problem. In contrast, stall flutter may occur in one degree of freedom (e.g. pitch) and is a non-linear phenomenon. Stall flutter occurs as a result of the negative aerodynamic damping associated with large leading-edge separation in the stall regime. In both cases however, the growing oscillation can become limited by the aerodynamics to a dynamic stable state. LCOs are fundamentally non-linear and, in the context of this thesis, occur as the wing pitches in and out of leading-edge separation conditions at large pitch amplitudes. The following sections outline the theory surrounding different aeroelastic phenomena.

## 1.5.1 Divergence

The most basic aeroelastic problem is the static elastic deformation of a wing due to a steady lifting force and an aerodynamic moment. At relatively low airspeeds, the elastic deformation due to the aerodynamic moment is sufficiently small [3]. After a certain airspeed however, the aerodynamic moment can be sufficiently large to cause the wing to become statically unstable, and break. This static aeroelastic instability is known as divergence.

One can estimate the divergence speed from Equation 1.7 for a wing of constant chord, with a thin-symmetrical airfoil as its profile. If the location of the EA is ahead of the AC, based on the coordinate system in Figure 1.9, the value for $e$ will be negative and the total aeroelastic stiffness will always be positive. The system will be stable and divergence will not occur for this case. For the case where the EA is aft of the aerodynamic centre, the aeroelastic stiffness becomes zero at a certain airspeed. The theoretical airspeed for a wing of constant chord and finite span can be estimated by rearranging Equation 1.7 into Equation 1.32 for when the total aeroelastic stiffness becomes zero:

$$U_{div} = \left[\frac{K_\theta}{e\rho bl2\pi}\right]^{\frac{1}{2}} \tag{1.32}$$

If non-linear effects are considered in the static aerodynamic moment however, non-zero static equilibrium points may exist past the divergence speed. If the moment is modelled as a cubic hardening spring with a coefficient $k_3$, the static equilibrium in pitch may follow a supercritical pitchfork bifurcation for airspeeds above the analytical divergence speed. This is shown in Equations 1.34-1.36, where $K_{tot}$ is the total linear aeroelastic stiffness.

$$K_\theta\theta + k_3\theta^3 = \left[e\rho U_\infty^2 bl2\pi\right]\theta \tag{1.34}$$

$$(K_{tot} + k_3\theta^2)\theta = 0 \tag{1.35}$$

Where,

$$K_{tot} = K_\theta - e\rho U_\infty^2 bl2\pi \tag{1.36}$$

The solutions of which are given in Equation 1.37, where $\theta_{eq}$ is the static equilibrium point. There is the trivial case of the equilibrium point at zero. The second set of solutions only exists past $U_{div}$, and only when $K_{tot} < 0$, which occurs when the EA is negative and aft of the aerodynamic centre. The two sets of solutions are schematized in Figure 1.11. The solid lines indicate a stable state, while the dotted lines indicate an unstable state.

$$\theta_{eq} = 0, \ \theta_{eq} = \pm\sqrt{\frac{-K_{tot}}{k_3}} \qquad\qquad [1.37]$$
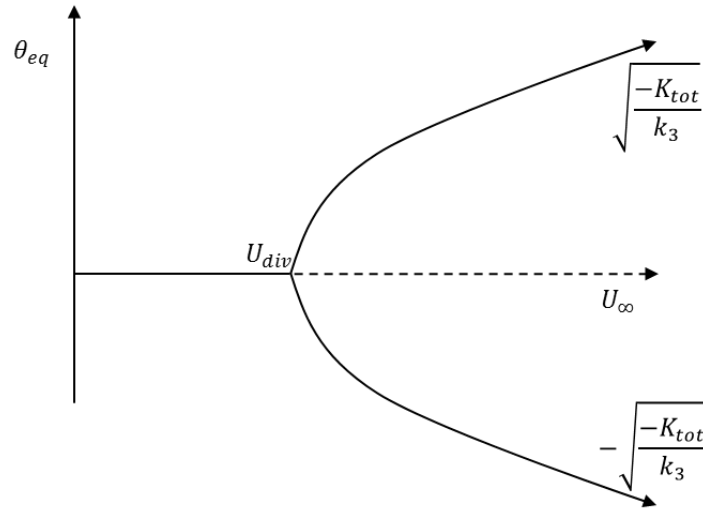


*Figure 1.11: Schematic of supercritical pitchfork bifurcation for non-linear analytical solutions to divergence.*

## 1.5.2 Coupled Flutter

Coupled flutter, or coalescence flutter, is the most studied type of flutter to date. It occurs as a result of a coupling of two degrees of freedom, where a dynamic aeroelastic instability arises at a critical speed termed the "critical flutter speed" [3]. At speeds above the critical flutter speed, energy is transferred to the structure as a wing begins to oscillate. The total aeroelastic damping of the system at this point also decreases below zero. The oscillations either become more violent and cause the wing to break, or are limited by the aerodynamics and enter an LCO regime. When the system is below the critical flutter airspeed, all perturbations settle since the overall damping remains positive.

The coupling between two degrees of freedom, most commonly pitch and heave, permits the transfer of energy from the flow to the airfoil. Positive work done by the flow on the airfoil indicates that the oscillations are not forced, and are self-sustained. The phase angle between the pitch and heave degrees of freedom is an important consideration in relation to the system's coupling behaviour. Assuming SHM and integrating the work, it was presented in Fung that for the overall work on the airfoil to remain positive, the lift and heave velocity be in opposite

directions for a large part of the cycle [3]. The phase difference between the two motions is therefore crucial to produce flutter.

When a 2DOF aeroelastic system approaches the critical flutter speed, the modal frequencies of each coalesce towards each other. As the resulting modal frequencies coalesce (coalescence of the modal frequencies is close but never exact), the decay rate of one of the modes becomes negative, inducing instability. The nature of these modes is illustrated by the results of linear modelling in Figure 1.12. Re-plotting the modal frequencies with decay rate in the Argand plane, the algebraic relation between the roots becomes more obvious. Here it can be observed that as the modal frequencies move towards each other, the decay rate of one branch becomes negative.

It can be inferred that the closer the structural natural frequencies are to each other, the sooner coalescence will occur and the lower the critical flutter speed will be [20]. The general trend of the frequency ratio ($\bar{\omega} = \sqrt{K_h/M_h}/\sqrt{K_\theta/I_{EA}}$) with critical flutter speed is illustrated in Figure 1.14, where a 'dip' occurs around a frequency ratio of 1. The behaviour of coupled flutter for a particular aerodynamic system can therefore be controlled by the stiffness characteristics of the airfoil.
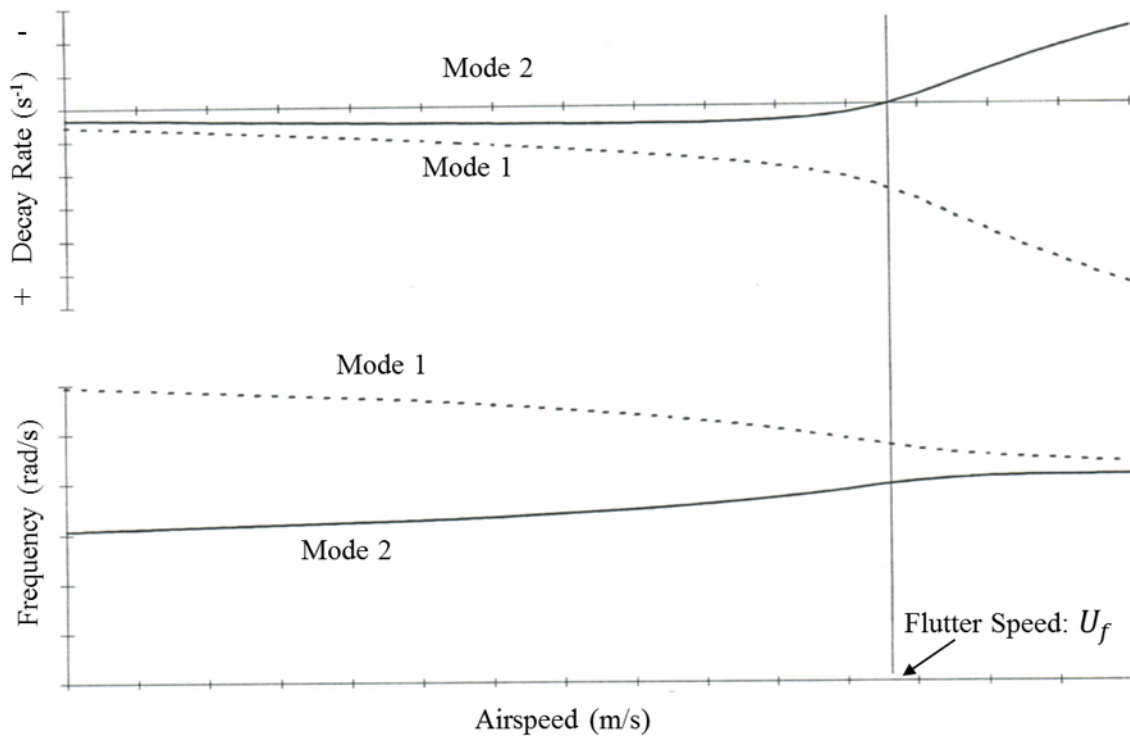


Figure 1.12: Schematic of coupled and damping-airspeed (top), frequency-airspeed (bottom), curves.
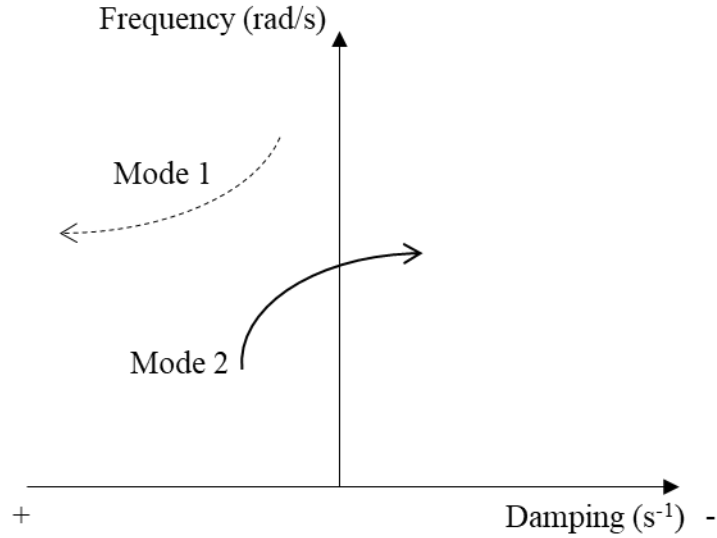
19

*Figure 1.13: Schematic of coupled frequency-damping curves in the Argand plane.*
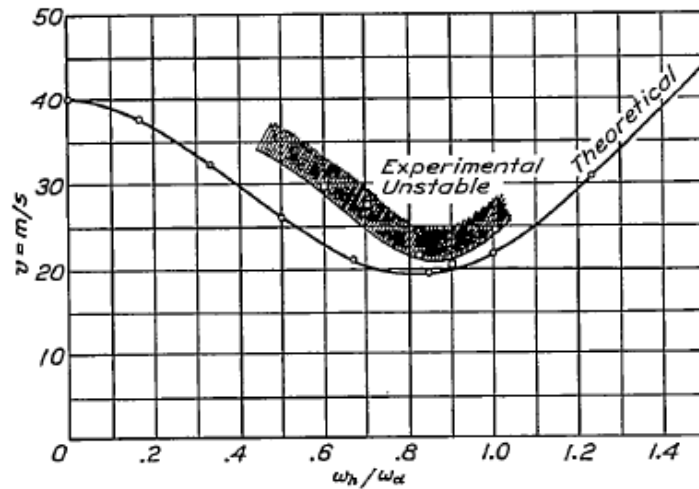


*Figure 1.14: Theoretical and experimental curves for flutter speed with varying frequency ratio, for a 2DOF system in bending and torsion. Taken from [20]*

Linear models covered in sections 1.4.3 and 1.4.4 can be used to predict the flutter behaviour until the flutter speed. Generally, an estimated reduced frequency value from the experimental flutter induced LCO is used to determine whether to use a quasi-steady versus unsteady model. Assuming quasi-steady flow for the purposes of this example, Equations 1.10 and 1.13, outlined in section 1.4.3, can be used to estimate the aerodynamic lift and moment about the quarter-chord point. Combining all terms and rearranging, the overall equation can be compactly simplified in matrix form.

$$[M]\begin{Bmatrix} \ddot{h} \\ \ddot{\theta} \end{Bmatrix} + [D]\begin{Bmatrix} \dot{h} \\ \dot{\theta} \end{Bmatrix} + [K]\begin{Bmatrix} h \\ \theta \end{Bmatrix} = \begin{Bmatrix} 0 \\ 0 \end{Bmatrix} \qquad [1.38]$$

In order to solve the system's equation of motion and determine the eigenvalues for a range of airspeeds, the equations are translated into the Laplace domain.

$$\left[s^2[M] + s[D] + [K]\right]\begin{Bmatrix}H(s)\\ \theta(s)\end{Bmatrix} = \{0\}$$

[1.39]

Where $s$ is the complex variable in the Laplace domain, and the matrices $M$, $D$ and $K$ are 2×2 for this case. Calculating the determinant of the above matrix will produce the characteristic polynomial shown in Equation 1.40. The roots of which give the eigenvalues, with $P_n$ being arbitrary real coefficients of the polynomial.

$$|[A]| = P_4 s^4 + P_3 s^3 + P_2 s^2 + P_1 s + P_0 = 0$$

[1.40]

The fourth order polynomial will have two conjugate pairs of complex roots, which are a function of airspeed. Each pair corresponds to a particular mode: two complex conjugate pairs for two modes. The complex solution is of the type presented in Equation 1.41, where $j$ is a number from 1 to 4. While this case is applied to quasi-steady models, the same process is used for different models. Unsteady models, such as Wagner's, produce two additional roots. From two equations of motion, the quasi-steady model produces four complex roots, while two real roots result from the third equation of motion associated with the unsteady aerodynamics.

$$s_j = -\beta_j \pm i\omega_{dj}$$

[1.41]

The coupled decay rate $\beta$ will be a positive number when the system is stable and the oscillations due to a perturbation are damped out. Once the decay rate reaches zero for one mode, there is zero damping and the system is said to have reached the critical flutter speed. The coupled eigen-frequency for each mode is represented by $\omega_{dj}$. Representative of coalescence flutter is the nature of the coalescence of the eigen-frequencies towards each other as the flutter speed is approached. The nature of the decay rate, as well as the coupled eigen-frequencies can be determined by plotting their values at varying airspeeds. The nature of the modal branch associated with the decay rate crossing the x-axis may dictate the occurrence and strength of the flutter [13]. Therefore there are two forms of coalescence flutter: hard and soft. A steeper branch slope may predict more explosive and energetic flutter. These linear models however fall short in predicting aeroelastic behaviour if oscillations stabilize to an LCO due to the non-linear dynamics. A comprehensive understanding of coupled flutter post-critical responses has not been achieved yet. In most cases, the studies refer to systems with mechanical non-linearities which blend with the aerodynamic non-linearities associated with leading-edge separation [21].

A notable study conducted by Pigolotti et al. investigate the influence of the position of the centre of mass, as well as the effect of varying frequency ratios and heave damping on the coupled flutter induced LCO response of a pitching flat plate [21]. It was found that a small static imbalance introduces an inertial coupling which enhances the vibration intensity, and energy extraction from the flow. The influence of frequency ratio was also found to be apparent, where

all configurations for a frequency ratio close to one show a similar response in the post-critical regime. At a frequency ratio close to one, both DOFs experience large oscillation amplitudes. Greater heave oscillation amplitudes were observed for frequency ratios below one, while the pitching amplitude was reduced. For a frequency ratio above one, the oscillations were in-phase, and reduced for both degrees of freedom. For all configurations other than for a frequency ratio of 1.24, an increase in the heave damping reduces the oscillation amplitudes. For a frequency ratio of 1.24 however, the oscillation amplitude in pitch is enhanced with increased structural damping in heave, while the heave response remains mostly unchanged. It was observed that the amplitude-velocity curves of all tested configurations originated from a common point, and resembled a supercritical Hopf bifurcation trend in the LCO amplitude with airspeed, as described by Dowell et al. [4].

### 1.5.3 Stall Flutter

Stall flutter is an aeroelastic phenomenon associated with dynamic stall as a wing pitches in and out of leading-edge separation conditions at large pitch amplitudes, thus inducing negative aerodynamic damping for part of the cycle [3, 22]. It is fundamentally a non-linear problem, and is triggered by a large amplitude disturbance if the wing is initially resting at a small AoA equilibrium. Because it is inherently non-linear, analytical linear models fall short on estimating its onset and behaviour. Unlike coupled (classic) flutter which requires two 2DOF, stall flutter may occur in 1DOF pitching motion. When instability is induced, the oscillation grows until it becomes limited by the flow. At this point the airfoil motion reaches an LCO.

While stall flutter is an aeroelastic occurrence, dynamic stall is an unsteady aerodynamic phenomenon. Characteristic of dynamic stall is an induced hysteresis in the aerodynamic loads of an airfoil undergoing forced SHM. The predominant feature of dynamic stall is the formation, shedding and convection over the surface of the airfoil of an energetic vortex-like disturbance. This convection induces a non-linearly fluctuating pressure field, and produces transient variations in forces and moments that are fundamentally different from steady-state aerodynamics [23]. Figure 1.15 presents a schematic of static aerodynamic moment coefficients with increasing AoA, along with superimposed moment coefficients for an airfoil undergoing forced SHM inside and outside the stall regime. As can be observed, a hysteresis loop in the aerodynamic moment for an airfoil with an elastic axis aft of the aerodynamic centre occurs when the wing pitches in and out of the stall regime, indicating non-linear behaviour.

A clockwise loop, and subsequent negative aerodynamic damping occurs in the stall region, where energy is transferred to the structure. In this region, positive work is done by aerodynamic forces, and acts in the direction of the airfoil motion. Positive aerodynamic damping, and negative work occurs when the airfoil motion exits the stall region. Counter-clockwise elliptical loops occur for linear and stable behaviour outside the stall region, while the flow is attached. As pointed out by Dimitriadis and Li, while an extensive amount of literature exploring the behaviour of dynamic stall exists, there remains much to be understood about the

aeroelastic response of stall flutter [24]. Due to the highly non-linear nature of stall flutter, its behaviour is difficult to model and as a result, previous work has been primarily experimental. Related studies investigated LCOs of NACA 0012 airfoils within the transitional Reynolds number ($10^4 \leq Re_c \leq 10^6$) regime, and for elastic axis locations at or aft of the aerodynamic centre (EA$\geq 0.25c$). Since stall-flutter is known to be associated with dynamic stall, cited studies have analyzed oscillations about a large non-zero AoA (asymmetric) [24-25]. Reports on oscillations about a zero AoA (symmetric) on the other hand, have been sparse. Of the most relevant studies, Dimitriadis and Li investigated 2DOF stall flutter induced LCOs, where the relative stiffness in heave was much higher than in pitch ($\bar{\omega} = 6.94$).
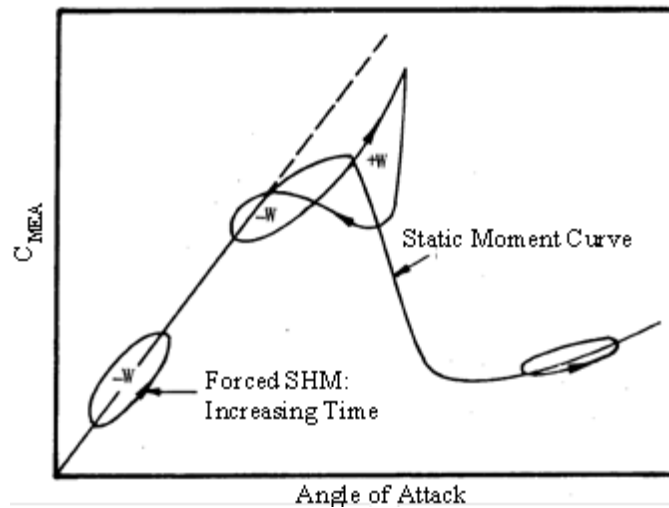


*Figure 1.15: Aerodynamic moment coefficient with AoA. Included are loops associated with the unsteady forced SHM in the laminar and stall regimes. Adapted from [22]*

The experimental set-up of the study conducted by Dimitriadis and Li in 2009 comprised of a rigid NACA 0012 with an elastic axis located at 38.3% of the chord length. The theoretical divergence airspeed was determined to be 17.9 m/s, which fell within the range of airspeeds tested 12 m/s $\leq U_\infty \leq$ 27 m/s ($2.4 \times 10^5 \leq Re_c \leq 5.4 \times 10^5$) [24]. Symmetric LCOs occurred until 18 m/s, after which asymmetric LCOs were observed. The asymmetric oscillations were theorized by the authors to be associated with the onset of divergence, since they occurred just past the theoretical divergence airspeed. Within this region, both symmetric and asymmetric oscillation coexisted, however the asymmetric LCOs acted as the stronger attractor. The amplitude and frequency of the symmetric oscillations increased in value until about 15 m/s, after which a constant amplitude plateau of 40° was reached. The unsteady aerodynamic moment was plotted with AoA at 16.8 m/s ($Re_c = 3.4 \times 10^5$) revealing stable and unstable regions: an inner loop enclosed by two outer loops. The lift with AoA was also plotted, and revealed a 'bow-tie' shape with oscillations. Asymmetry in the outer loops of the graph is thought to be attributed to the bias in the flow. Although the tests were conducted in the transitional region, no SAOs were observed in this study. The static lift and pitching moment coefficient measurements did not reveal any non-linearities, indicating the possibility of high free-stream turbulence in the experimental set-

up. Other studies include Bhat and Govardhan in 2013, where only asymmetric oscillation amplitudes of 2°, 4°, 6°, about a mean AoA of 15° were observed [25]. Measurements were conducted at Reynolds numbers on the order of $3\times10^4$, with a NACA 0012 airfoil oscillating about the quarter-chord. The net energy transferred to the airfoil was found to be positive when the AoA about which the LCOs occurred was greater than the airfoil stall angle. Particle Image Velocimetry (PIV) was also conducted to visualize the leading-edge vortex.

## 1.5.4 Lock – in

Lock-in is another aeroelastic phenomenon, usually occurring over elastically mounted bluff-bodies interacting with shed vortices. The resulting resonant vibration of a cylinder with diameter $D$ is induced through the aeroelastic interaction with its own shed vortices into the wake of frequency $f_s$. The shed vortices of alternating sign in the wake of a static cylinder is known as a von Kármán vortex street. The behaviour follows the Strouhal law ($St = f_s D / U_\infty$) at subcritical Reynolds numbers or shear-layer transition regime [26-27]. A typical value is $St = 0.2$.

The cylinder vibrates at a frequency $f$ when the vortices act as a forcing mechanism. For a cylinder elastically restrained with a restoring force, resonance occurs when the shedding frequency is close to the structural natural frequency $f_n$. As a result, a coupling occurs between the heave oscillation and the shedding frequency, a schematic for which is presented in Figure 1.16 below. The large amplitude response of the cylinder affects the behaviour of the vortex shedding, such that the shedding frequency becomes locked into the natural frequency of the cylinder. This is the point at which lock-in occurs. The oscillation amplitude and frequency behaviour are schematized below in Figure 1.17 The left graph shows the plateau in the ratio of the oscillation frequency over the natural structural frequency, characteristic of lock-in. The right graph represents the resonance peak in the non-dimensional heave amplitude at lock-in.
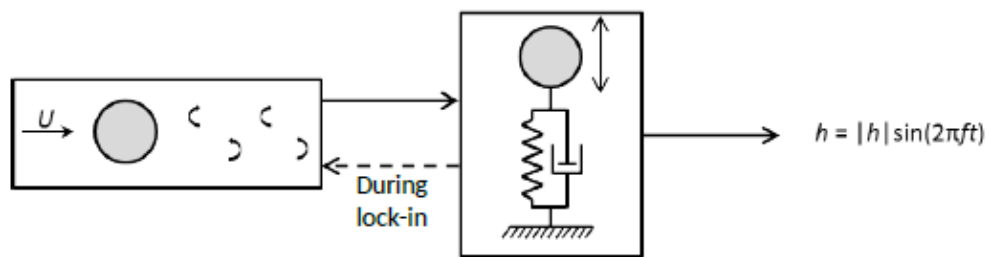


*Figure 1.16: Cylinder interacting in a feedback relationship with Kármán vortex shedding during lock-in. Taken from [28]*
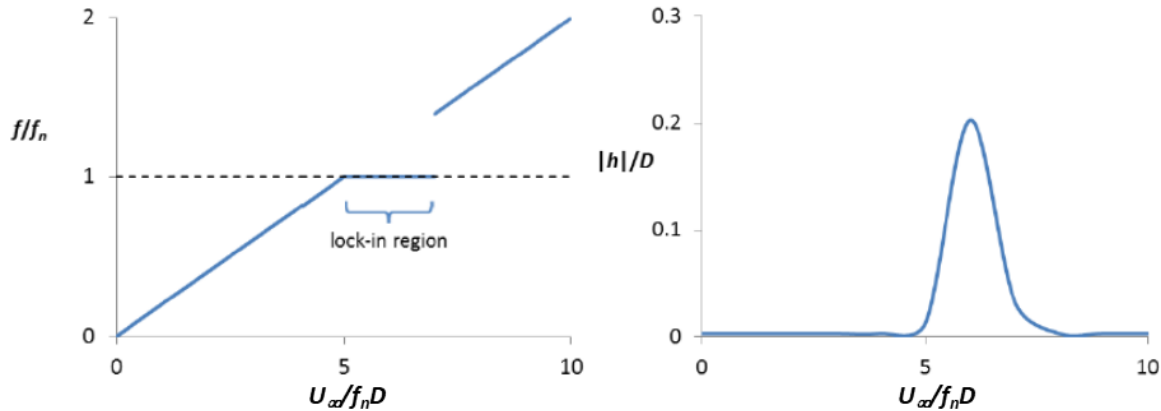
*Figure 1.17: Characteristic behaviour of an oscillating cylinder in and out of the lock-in region. Adapted from [28]*

## 1.5.5 Laminar Separation Flutter

Low to transitional Reynolds number effects have been shown to have a significant influence on an elastic airfoil. In flows with low free-stream turbulence, laminar boundary-layer separation can occur at AoAs below stall angles. Transition of the laminar shear layer, and subsequent turbulent reattachment leads to the formation of a laminar separation bubble (LSB) at small AoA [29-31]. A schematic of the LSB is shown in Figure 1.18. The resulting non-linear variation of the static aerodynamic lift and moment, due to the formation of an LSB at small AoA, is shown below in Figure 1.19. As previously investigated, small constant amplitude LCOs (SAOs), in either 1DOF or 2DOF, occur as a result of feedback coupling mechanism between the LSB behaviour and the structural response. Much of the previous work done was conducted at RMC, or collectively at University of Laval, Carleton, and NRC [32-33]. The resulting negative aerodynamic damping occurs in the static non-linear region at low AoA. It was found that adding roughness to an airfoil or increasing the free-steam turbulence levels repressed the existence of SAOs. From experimental results conducted at RMC, the amplitude and frequency of the SAOs do not differ much between 1DOF and 2DOF cases [13]. However, the introduction of the heave degree of freedom significantly increases the energy transfer from the flow to the structure, even though SAOs have been shown to be fundamentally a 1DOF problem.

In a 2010 study by Poirel and Yuan, the aerodynamic moment of a NACA 0012 airfoil undergoing 1DOF small amplitude LCOs was investigated at a Reynolds number of $7.7 \times 10^4$, with the EA set to 18.6% of the chord length [33]. The moment is calculated from experiment, as well as fitted empirically as a Duffing-van-der-Pol nonlinearity. Large eddy simulations (LES) of the flow about the airfoil undergoing prescribed SHM using the amplitude and frequency from experiment were also performed. The characteristics of the aeroelastic LCO are reminiscent of stall flutter, except that they occur at moderate AoAs, and show a strong sensitivity to Reynolds number. It was determined from the results that the aerodynamic stiffness is highly non-linear and behaves as a softening spring within the tested AoAs considered. Although the pitch motion

resembles SHM, the plotted aerodynamic moment, as shown in Figure 1.20, contains hysteresis effects associated with nonlinear content in the response. The contrast between linear and non-linear models can be seen by comparing the defined elliptical shape for the linear case, as well as the counter-clockwise direction of the loop indicating negative work done by the flow. Similar to stall-flutter, classical unsteady linear models fall short in predicting SAO behaviour, indicating a non-linear influence of the LSB.
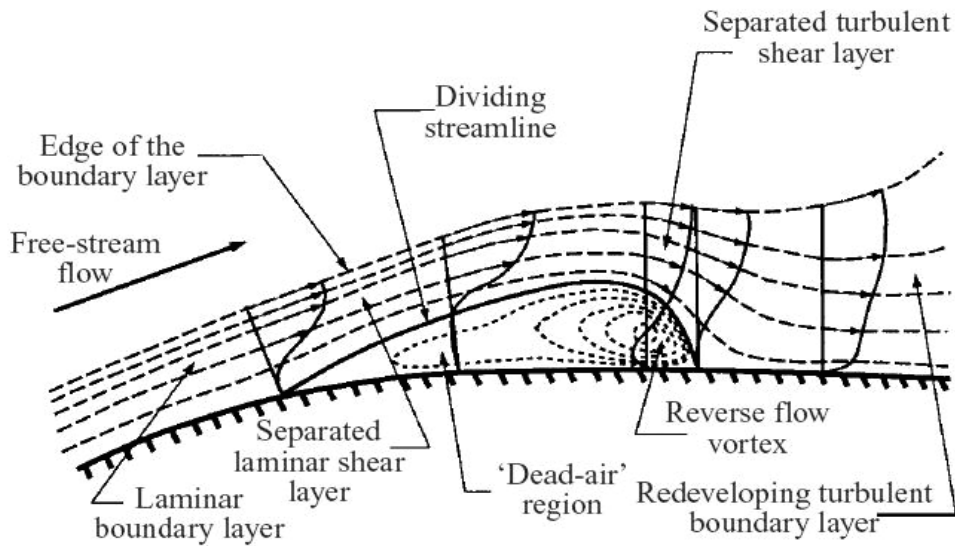


*Figure 1.18: Schematic of the Laminar Separation Bubble (adapted from [34])*
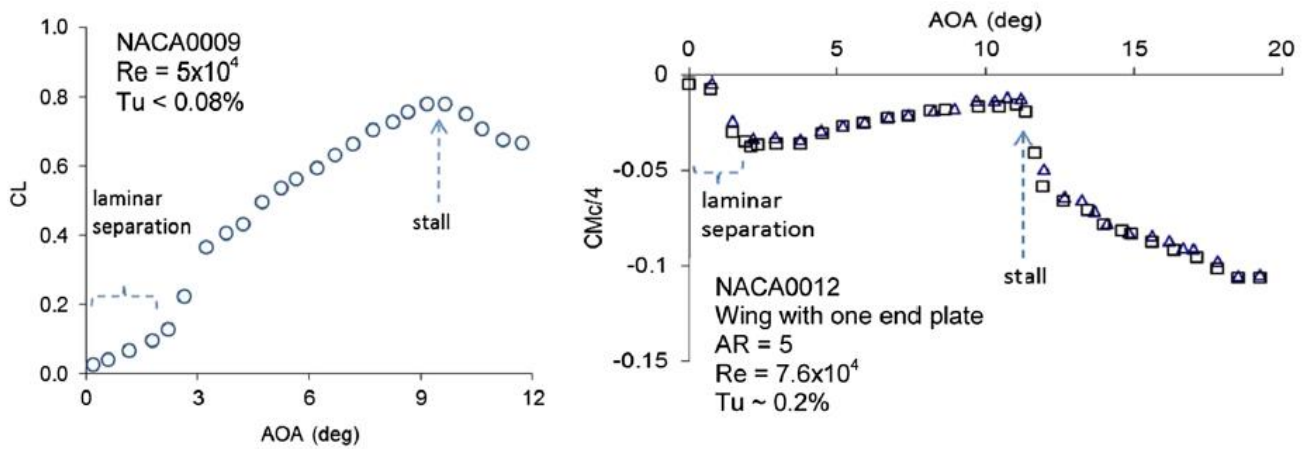


*Figure 1.19: Experimentally obtained aerodynamic coefficients for symmetrical airfoils and low free-stream turbulence (taken from [13])*
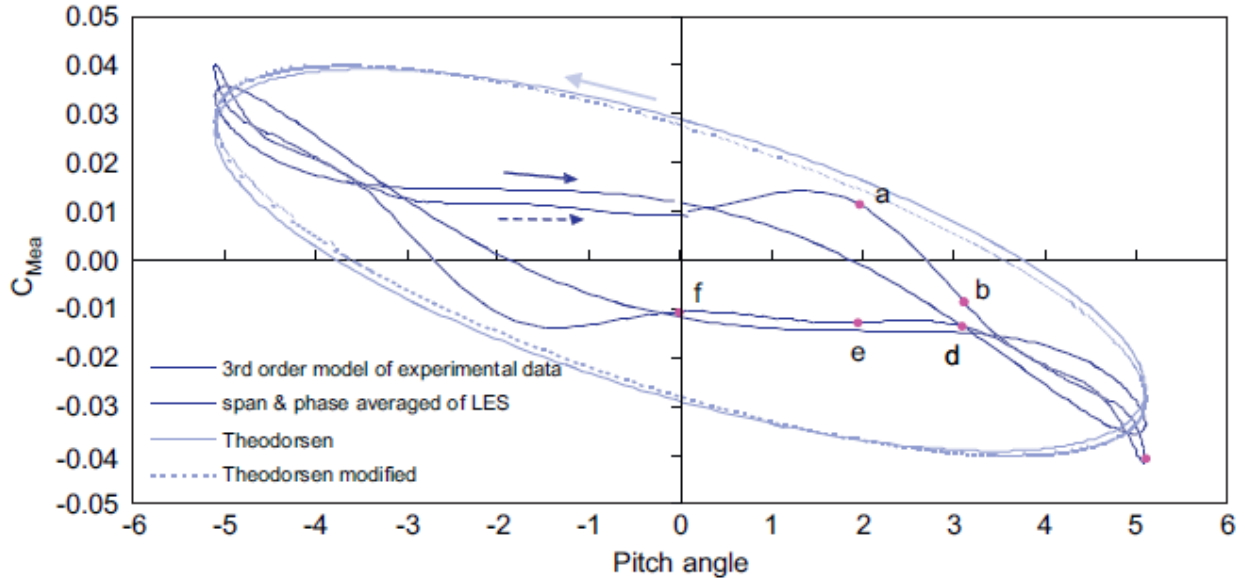
*Figure 1.20: Aerodynamic moment coefficient as a function of pitch angle during one cycle for linear and non-linear analytical models of laminar separation flutter (taken from [33]).*

## 1.6 Aerodynamic Work and Energy

For a 2DOF airfoil free to oscillate in pitch and heave, as defined in section 1.4.1, the work done by the aerodynamic loads can be calculated using Equation 1.42 below. Knowing the structural parameters of the system, as well as differentiating the position data to obtain the velocity and acceleration, the aerodynamic moment and lift can be calculated using the equations of motion 1.2 and 1.3. The aerodynamic loads can then be calculated at each time step. If the airfoil is undergoing nonstationary periodic motion, the calculated work is averaged to obtain the value done per cycle.

$$\overline{W} = \oint M_{EA}\, d\theta + \oint L dh \qquad\qquad [1.42]$$

Assuming SHM in pitch and heave, the subsequent linear aerodynamic moment and lift distributions with the pitch and heave follow elliptical distributions. These ellipses are visualized as schematics in Figure 1.21, where the total amount of work per cycle represents the area enclosed within the ellipse. The work calculation can be decomposed into the following integrals based on this concept.
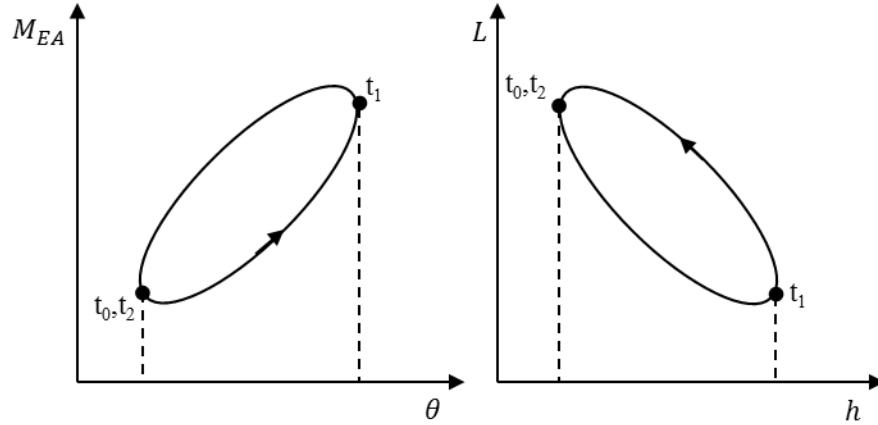
*Figure 1.21: Schematic of moment response with pitch and lift response with heave for a 2DOF aerodynamic system undergoing SHM. Both cases are counter-clockwise and therefore represent the structure expending energy into the flow.*

$$\bar{W} = \left[ \int_0^1 M_{EA} \, d\theta + \int_2^1 M_{EA} \, d\theta \right] + \left[ \int_0^1 L \, dh + \int_2^1 L \, dh \right] \qquad [1.43]$$

The calculation for work is path dependant. In Figure 1.21 the negative work done from $t_1$ to $t_2$ exceeds the positive work done from $t_0$ to $t_1$. The resulting loop is counter-clockwise, and the overall calculated work done by the aerodynamics from Equation 1.43 becomes negative, indicating a stable system. A clockwise loop would indicate instability, where positive overall work is transferred to the structure. Since the inertia and stiffness terms are conservative and do not contribute to the net-work per cycle, the analytical equation can be derived for SHM motion, as presented in Equations 1.44 and 1.45 [13]. Here, the pitch amplitude of the SHM is represented by $\theta_0$, the heave amplitude by $h_0$, while the circular frequency is $\omega$ and the phase $\varphi$.

$$\theta = \theta_0 \sin \omega t \qquad [1.44]$$
$$h = h_0 \sin(\omega t - \varphi) \qquad [1.45]$$

$$\bar{W} = D_\theta \theta_0^2 \omega \pi + D_h h_0^2 \omega \pi \qquad [1.46]$$

The cycle-averaged power can be determined from the loads, as well as from the cycle-averaged work. It can also be expressed analytically in Equation 1.48.

$$\bar{P} = \frac{1}{T} \int_t^{t+T} \left[ M_{EA} \dot{\theta} + L \dot{h} \right] dt = \frac{\bar{W}}{T} \qquad [1.47]$$

$$\bar{P} = \frac{D_\theta \theta_0^2 \omega^2}{2} + \frac{D_h h_0^2 \omega^2}{2} \qquad [1.48]$$

Despite several definitions for aerodynamic efficiency found in literature, the one used in this study corresponds to the analysis performed by Kinsey and Dumas in 2014 [6]. This definition of

efficiency $\eta$ is calculated by finding the percent of extracted power from the power available in the stream, and is expressed in Equation 1.49. The power available $P_a$ is defined as the flux of the kinetic energy flowing through the overall swept area. The span is $l$, and $d$ is the total length traversed by the oscillation, which includes the additional distance projected by the pitch motion as illustrated in Figure 1.5 in Section 1.2.

$$\eta = \frac{\bar{P}}{P_a} \tag{1.49}$$

$$P_a = \frac{1}{2}\rho U_\infty^3 ld \tag{1.50}$$

An alternative definition uses the heave amplitude rather than the overall swept area. Others express the efficiency as a percentage of the Betz limit ($\eta_{max} = 16/27$). The Betz limit is known as the theoretical maximum percent of extracted power from a flow, and is derived analytically assuming steady and inviscid flow through an actuator disk in a stream tube.

The averaged kinetic energy per oscillation cycle can also be calculated numerically with reference to the centre of gravity.

$$\overline{KE} = \frac{1}{T}\int_0^T \frac{M_h \dot{h}_{CG}^2}{2}\,\mathrm{d}t + \frac{1}{T}\int_0^T \frac{I_{CG}\dot{\theta}^2}{2}\,\mathrm{d}t \tag{1.51}$$

where,

$$I_{CG} = I_{EA} - M_\theta \left(\frac{x_\theta c}{2}\right)^2 \tag{1.52}$$

$$h_{CG} = h - M_\theta \frac{x_\theta c}{2}\theta \tag{1.53}$$

For SHM, and by considering the phase angle between $h$ and $\theta$, the equation below can be derived [13], where $h_{0_{CG}}$ is the heave amplitude about the CG.

$$\overline{KE} = \frac{M_h h_{0_{CG}}^2 \omega^2}{4} + \frac{I_{CG}\theta_0^2 \omega^2}{4} \tag{1.54}$$

# Chapter 2 – Experimental Methods

## 2.1 Experimental Test Rig

Experiments were conducted in the large recirculating wind tunnel at the Royal Military College of Canada, illustrated in Figure 2.1. The test section has cross sectional dimensions of 0.76 m x 1.08 m, and a maximum turbulence intensity level of 0.2%. Compressibility effects were not considered since the Mach numbers of the experiments did not exceed 0.05. As depicted in Figure 2.1, the test-section is located just after the contraction. The experimental apparatus of the test-section is composed of a rigid NACA 0012 wing of constant chord length, and smooth surface. Schematics of the aeroelastic test-section used are included below in Figures 2.2 and 2.3. The apparatus is capable of exhibiting fundamental linear and nonlinear aeroelastic phenomena, such as flutter and LCOs.
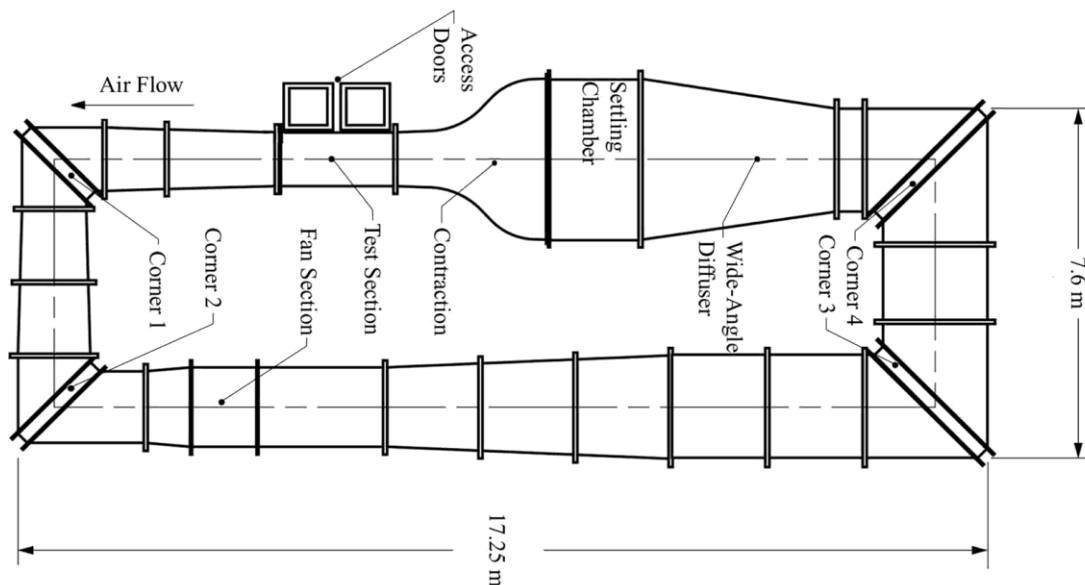


*Figure 2.1: Schematic of the Closed Circuit Wind Tunnel, taken from [14].*

As presented in Figure 2.2, the airfoil is mounted vertically in the test-section. The orientation of coordinate systems is included. A side view of the test section is presented in Figure 2.3, illustrating the location of the Pitot-static tube and thermocouple in relation to the direction of the airflow and aeroelastic set-up. Endplates are located above and below the wing to minimize three-dimensional effects. The airfoil is free to oscillate in 2DOF: pitch and heave. For stall-flutter induced LCOs in 1DOF, the airfoil was free to oscillate in pitch and constrained in heave. The motion is directed through pulley-spring assemblies in both pitch and heave degrees of freedom.
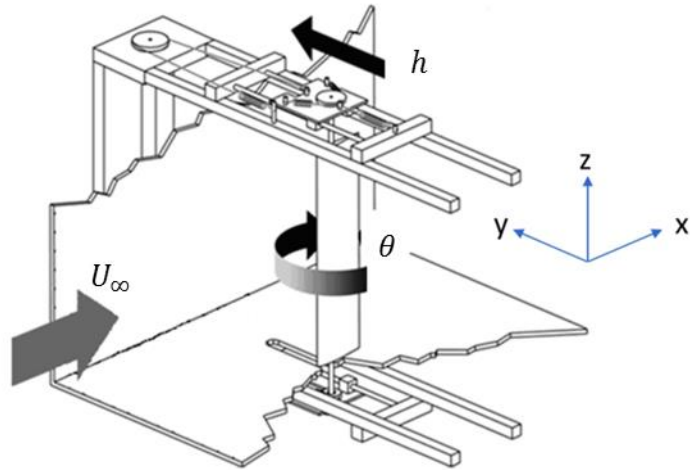
*Figure 2.2: Schematic of experimental set-up used for this study Schematic adapted [14].*
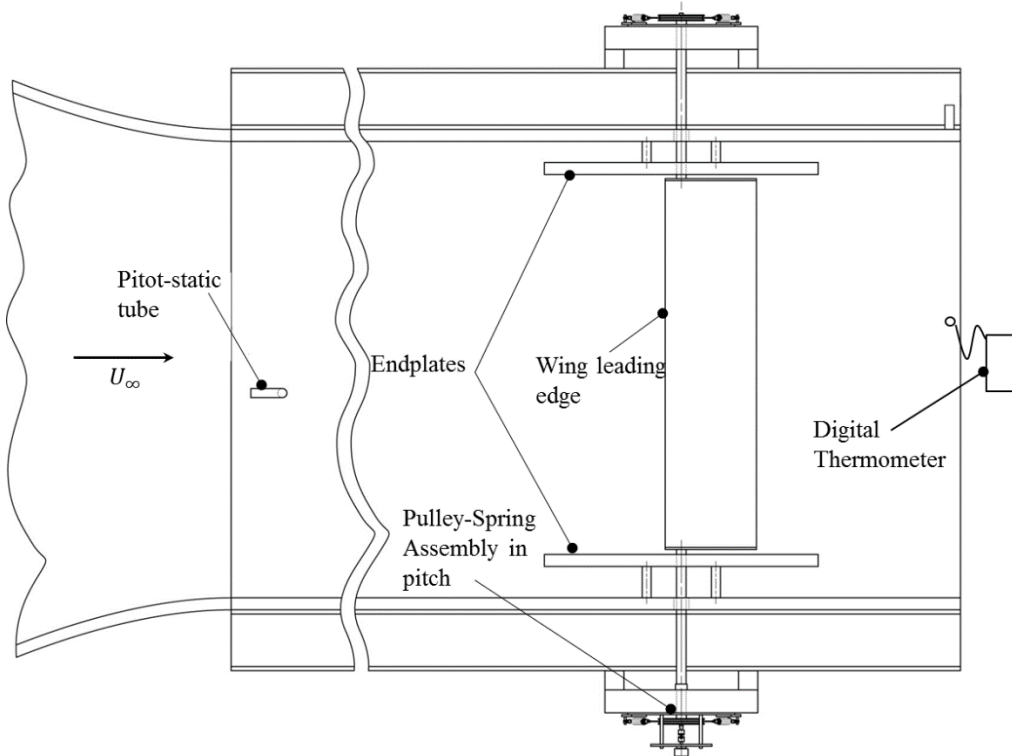


*Figure 2.3: Side-view of aeroelastic test-section*

Further details of the experimental system are illustrated from Figures 2.4 to 2.6. The wing is attached to two rods, one on each end, and connects to the test section through rotational bearings which permit movement in pitch. These rods pass through oblong openings cut into the endplates, and upper and lower sides of the test section. The ends of the rods are connected to mirrored pulley-spring assemblies on the bottom and top of the section, which themselves are attached to plates that translate the entire wing in heave. A set of rails permits the motion in

heave through roller bearing assemblies which are screwed into the plates. Like the pulley-spring assembly in pitch, the movement in heave is defined by a set of pulleys on the top and bottom of the test section, and are connected to each other through an external rod.

Each set of pulleys are connected to pairs of coplanar springs through the use of 1/32 inch wire rope. The springs provide an elastic restoring force, as well as the overall structural stiffness in both degrees of freedom. Spring extensions were added in order to ensure that the springs remain in tension during any experiment. The motion of the airfoil was recorded using rotary potentiometers in both pitch and heave. These potentiometers are attached to the bottom pitch and heave pulleys. A linear calibration curve was used in order to determine the position from a given voltage output.



*Figure 2.4: External rod on side of test section connecting heave spring/pulley systems*
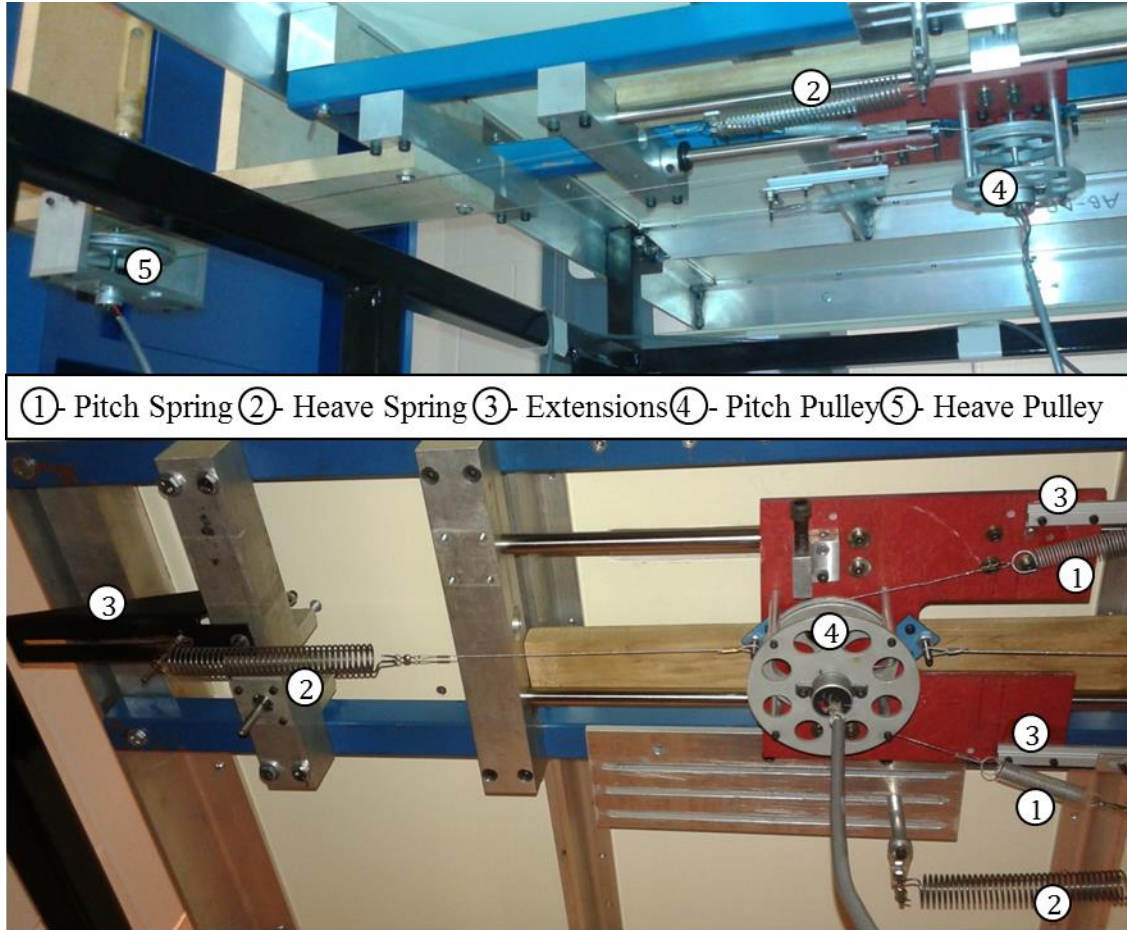
*Figure 2.5: Bottom side of test section, illustrating heave and pitch spring/pulley mechanisms*

## 2.2 Physical Parameters

### 2.2.1 Geometric and Structural Parameters

The equations of motion for the system analyzed in this study are derived for a two-dimensional thin, symmetrical airfoil with degrees of freedom in bending and torsion, as outlined in section 1.4.1. The Equations 1.2 and 1.3 in section 1.4.1 are thus obtained for the same coordinate system, and used in subsequent analysis. The frequency ratio of the system is defined as the ratio of the uncoupled structural natural frequency in the heave degree of freedom, over the pitch. For this system, it is defined by Equations 2.1-2.3.

$$\omega_h = \sqrt{\frac{K_h}{M_h}} \qquad [\,2.1\,] \qquad \omega_\theta = \sqrt{\frac{K_\theta}{I_{EA}}} \qquad [2.2]$$

$$\bar{\omega} = \frac{\omega_h}{\omega_\theta} \qquad [2.3]$$

Several parameters of the system remained unchanged for each experiment. These include the geometry of the wing, nominal spring stiffness in pitch, the mass of the heaving parts, mass of the pitching parts, and pitch pulley radius ($r_\theta$). Table 2.1 below presents a summary of constant structural values.

| Experimental Parameter | Value |
|:---:|:---:|
| $c$ (m) | 0.156 |
| $l$ (m) | 0.61 |
| $r_\theta$ (m) | 0.035 |
| $K_\theta$ (N·m/rad) | 0.3 |
| $M_h$ (kg) | 2.5 |
| $M_\theta$ (kg) | 0.77 |

*Table 2.1: Constant structural parameters for the aeroelastic system*
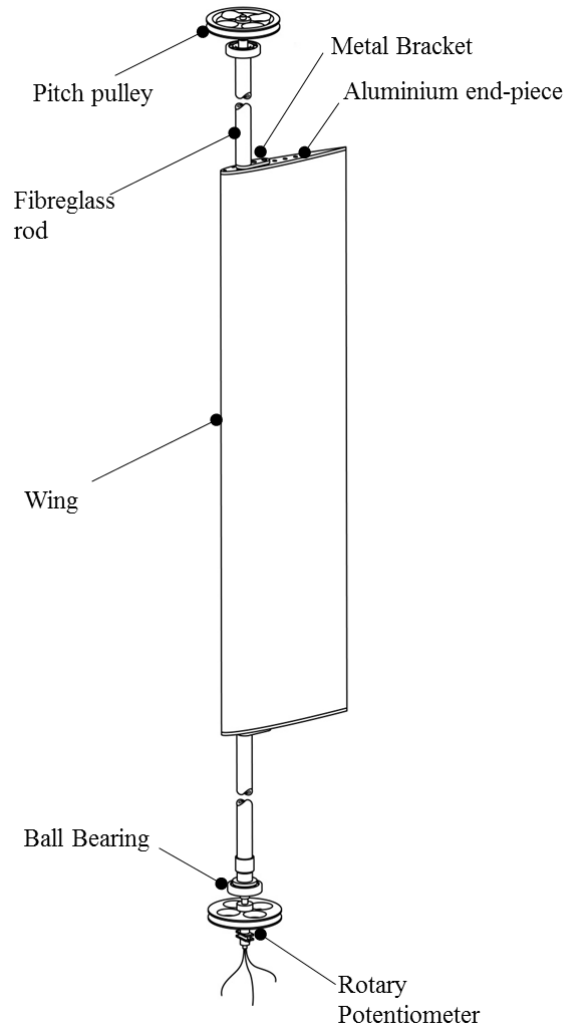


*Figure 2.6: Airfoil assembly with pitch pulley connection*

## 2.2.2 Uncoupled No-Flow Structural Constants

Using the no-flow dynamic response data, the structural parameters of the system can be estimated. The total stiffness in pitch and heave are calculated directly from the individual spring stiffness, for four springs in total, where $K_\theta = 4r_\theta^2 k_\theta$ and $K_h = 4k_h$. The individual linear spring stiffness coefficients were determined by measuring the linear extension of the springs, by hanging a certain amount of applied weight from one end. The following equations are used for each no-flow case, where the pitch and heave degrees of freedom were isolated resulting in two uncoupled equations of motion. For the each set of experiments in 2DOF, the stiffness in pitch was kept a constant 0.3 Nm/rad, whereas the springs in heave were varied to observe behaviours for a range of frequency ratios. Configurations tested varied overall heave stiffness from approximately 307.1 N/m to 1533.2 N/m. Experiments exploring 1DOF oscillations explored pitch stiffness values of 0.15 Nm/rad, 0.2 Nm/rad, 0.3 Nm/rad and 0.35 Nm/rad.

$$I_{EA}\ddot{\theta} + D_\theta \dot{\theta} + K_\theta \theta = 0 \qquad [2.4]$$

$$M_h \ddot{h} + D_h \dot{h} + K_h h = 0 \qquad [2.5]$$

Knowing both pitch and heave structural stiffness, the moment of inertia, mass of the heave components, as well as the structural damping in pitch and heave can be calculated from the above equations of motion, by assuming the characteristic Equation 2.6. The structural damping coefficients for each degree of freedom are assumed to be constant, the analysis is elaborated on in the following section. These can be determined from the equations of motion described above, where each term can be defined below.

$$\ddot{x} + 2\zeta\omega_n \dot{x} + \omega_n^2 x = 0 \qquad [2.6]$$

$$I_{EA} = \frac{K_\theta}{\omega_\theta^2} \qquad [2.7] \qquad\qquad M_h = \frac{K_h}{\omega_h^2} \qquad [2.8]$$

$$D_\theta = 2\zeta_\theta \omega_\theta I_{EA} \qquad [2.9] \qquad\qquad D_h = 2\zeta_h \omega_h M_h \qquad [2.10]$$

## 2.2.3 Free-Decay Procedure and Analysis

Three free-decay tests were carried out before and after each test in order to determine the structural parameters of the system, as well as to ensure that no changes to the system occurred. This process involved constraining one degree of freedom while recording the no-flow response in the other. Wooden blocks were used in order to prevent the roller bearings from sliding, constraining any motion in heave. The pitch pulleys were constrained by using a set-screw to prevent pulley rotation.

A perturbation was induced in either heave or pitch, during which data of the response was recorded. A linear oscillatory decay was observed, as can be seen in the example in Figure

2.7. The data was filtered using a second-order low-pass filter algorithm in MATLAB, with a cut-off frequency just above the estimated natural frequency in either pitch or heave. A peak-to-peak analysis was conducted, where the peaks of the local oscillation amplitude were located using an in-built function in MATLAB.

The natural and damped frequencies, as well as the damping ratios are determined experimentally by performing a peak-to-peak analysis of the no-flow free decay response. The damped natural frequency of either pitch or heave was calculated by determining the period of oscillation between the two peaks. The logarithmic decrement between peaks was used in order to calculate the damping ratio. The equations for the 1DOF pitch-only case are outlined below. Values where the damping ratio was observed to remain approximately constant were used to calculate the overall damping ratio and damping coefficient. An average of the values was taken in order to determine a constant value for the structural damping coefficient. A constant damping ratio indicates exponential decay and linear behaviour. The damping ratio was observed to vary inside the region where small amplitudes of the oscillation, in both pitch and heave, occurred. The varying damping ratio is theorized to be a result of dry-friction.

$$\omega_{d\theta} = \frac{2\pi}{\tau_{d\theta}} \qquad [2.11] \qquad\qquad \delta_{\theta} = \ln\frac{\theta_1}{\theta_2} \qquad [2.12]$$

$$\zeta_{\theta} = \frac{\delta_{\theta}}{\sqrt{(2\pi)^2 + \delta_{\theta}^2}} \qquad [2.13] \qquad\qquad \omega_{\theta} = \frac{\omega_{d\theta}}{\sqrt{1 - \zeta_{\theta}^2}} \qquad [2.14]$$
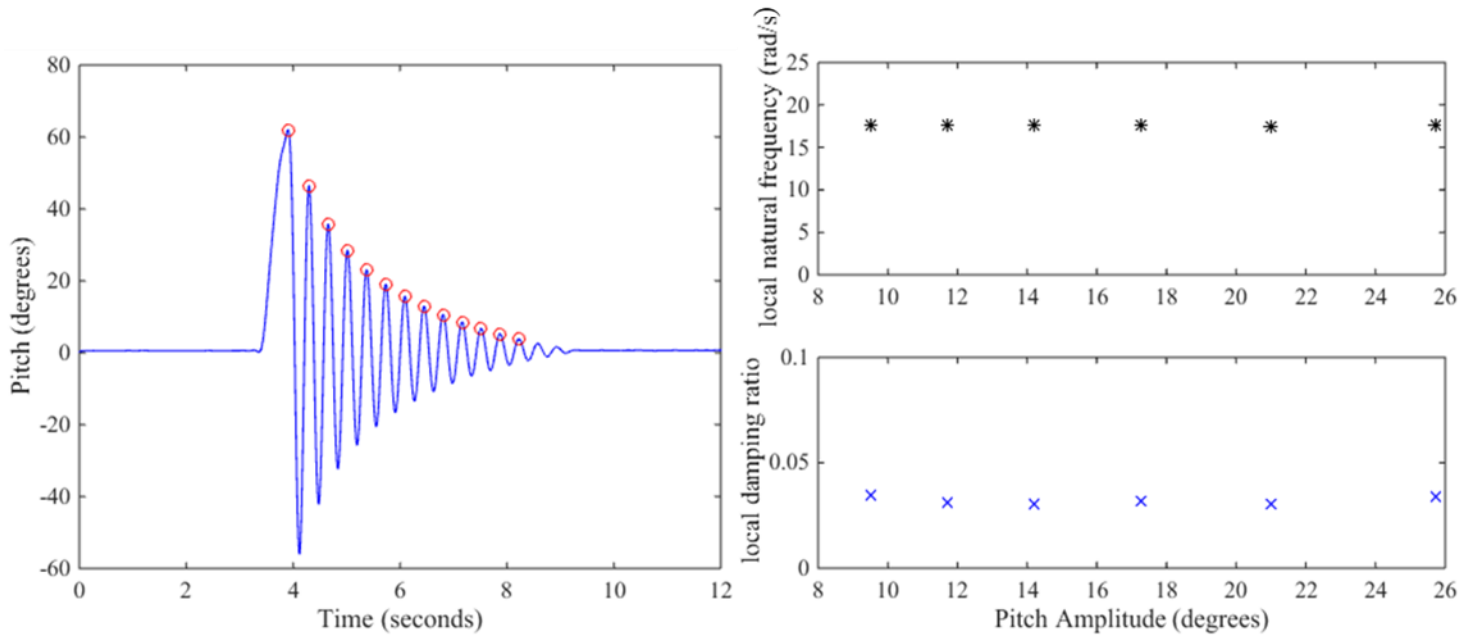


*Figure 2.7: Example of free-decay response of pitch only case (left), and local natural frequencies and damping ratios used to calculate structural coefficient values (right), for September 18th test.*
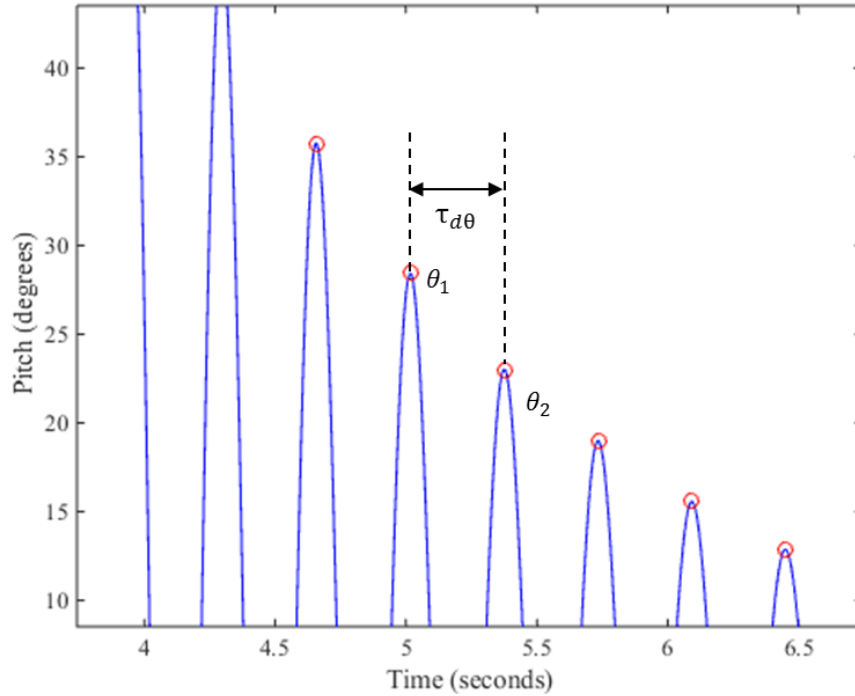
36

*Figure 2.8: Close up of peaks used in free-decay analysis for pitch only example case.*

## 2.2.4 Elastic Axis Location

Two sets of experiments, both with differing responses, were performed for elastic axis locations at 27% and 35% of the chord length from the leading edge. A schematic of the airfoil with the different elastic axis locations used in the study is included in Figure 2.9. A table with structural values corresponding to each elastic axis value is shown in Table 2.2. The values for static imbalance were taken from previous studies using the same set-up.
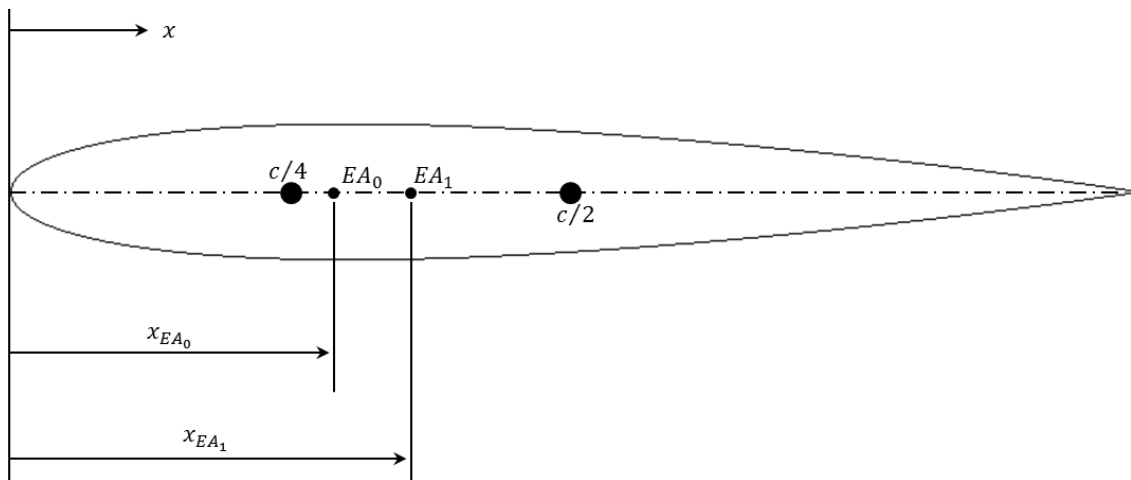


*Figure 2.9: Schematic of airfoil and relative positions of elastic axis tested. Not to scale.*

| | Elastic Axis Location | $I_{EA}$ (kg·m$^2$) | $x_\theta$ | $a_h$ |
|---|---|---|---|---|
| $EA_0$ | 27% chord length | 0.0011 | 0.093 | -0.46 |
| $EA_1$ | 35% chord length | 0.0010 | 0.004 | -0.3 |

*Table 2.2: Calculated structural values for each elastic axis location tested.*

## 2.3 Experimental Procedure

The springs were adjusted for each test in order to maintain extension during an experiment. This was ensured to avoid the motion of the airfoil to enter the compression region of the springs, which are associated with additional non-linearity of the system. Extra care was taken in order to align the wing in both pitch and heave, to minimize any additional biases.

LCOs were induced with an initial manual excitation in heave for 2DOF experiments. Manual excitations in pitch were performed for 1DOF stall flutter LCO experiments. Once the LCO amplitude and free-stream velocity reached steady state, data was recorded for at least 30 seconds using a sampling rate of 1 kHz. The voltage output from the rotary potentiometers were recorded by a NI PCI-6034E A/D card, using a Lab-View program. The maximum duration of data collected was 80 seconds, which corresponds to approximately 200 LCO cycles. These values were determined through a convergence study, elaborated in Appendix A. The RPM of the wind tunnel, thus airspeed, was subsequently increased, and the process repeated.

### 2.3.1 Temperature Measurement

The temperature inside the test section was measured using a thermocouple attached to a digital thermometer. The thermocouple was attached to the side opening of the test section, the probe was extended into the middle of the test section behind the trailing edge of the airfoil. The set-up is represented in the previous section (Figure 2.3). The ambient pressure was determined from a barometer located in the laboratory area. The density of the air was then calculated using Equation 2.15. The error in the atmospheric pressure was estimated to be about ±50 Pa from the barometer measurements, while the ambient temperature varied within ±0.1°K. The error in the density was estimated to be ±0.001 kg/m$^3$.

$$\rho = \frac{P_{atm}}{R_{air}T_\infty}$$ [2.15]

## 2.3.2 Airspeed

The airspeed was determined by using a pitot-static tube located at the inlet of the test-section, and was connected to a pressure transducer connected to a digital voltmeter. The output voltage from the pressure transducer was calibrated to give the dynamic pressure (pressure difference between the ambient pressure and the stagnation pressure in the pitot tube), from which the free-stream velocity in the wind tunnel can be calculated. The free-stream velocity was calculated once the oscillation of the airfoil reached steady-state, since there was a decrease in voltage while the wing was undergoing LCOs. This artefact is a result of kinetic energy being extracted from the flow. The following equations were used to calculate airspeed:

$$P_{dyn} = 673.7(V - V_0) \qquad [2.16]$$

$$U_\infty = \sqrt{\frac{2P_{dyn}}{\rho}} \qquad [2.17]$$

where $V$ is the measured voltage at a non-zero airspeed, and $V_0$ is the recorded no-flow voltage corresponding to the ambient pressure. The error in $V_0$ was estimated from the voltmeter to be $\pm 0.001$ V, while the error in $V$ was calculated to be $\pm 0.01$ V. The corresponding error in the dynamic pressure was determined to be approximately $\pm 7$ Pa, while the error in the airspeed was estimated to be $\pm 0.7$ m/s.

# Chapter 3 – Coupled Flutter

For the case where the elastic axis is located at 0.27c, both SAOs and large amplitude LCOs coexist. For instance, Mendes focussed on the behaviour of 1DOF and 2DOF SAOs for similar stiffness configurations [14]. While SAOs have been observed in this current study, the results and analysis in this chapter focus on the nature of the sustained large amplitude oscillations occurring when the EA is set at 27% of the chord length. These LCOs are due to coupled flutter rather than stall flutter, as will be discussed in the following sections. Note that the occurrence of SAOs indicate potential Reynolds number effects on the coupled flutter LCO behaviour.

## 3.1 Experimental Results for Coupled Flutter Limit Cycle Oscillations

Experiments were conducted for 3.65 m/s $\leq U_\infty \leq$ 14.0 m/s ($3.7\times10^4 \leq Re_c \leq 1.45\times10^5$). Error in the airspeed measurements was determined to be ±0.7 m/s. The analytical divergence speed for this configuration was calculated to be 16.37 m/s using Equation 1.32 for a pitch stiffness of 0.3 Nm/rad, and did not fall within the airspeeds tested. The pitch stiffness was kept constant for each test in this configuration. Frequency ratios tested included $0.67 \leq \bar{\omega} \leq 1.34$ for a range of heave springs. The static imbalance of this configuration is $x_\theta = 0.093$, indicating a larger degree of inertial coupling in the structural system compared to the case where the EA is set at 0.35c.

It will be shown in section 3.2 that the similarity in flutter speeds between model and experiment supports the assumption that the phenomenon observed is coupled flutter. In addition, no 1DOF oscillations were observed within the airspeeds tested as oscillations died out when blocked in either degree-of-freedom. On the other hand, while a linear model is used to determine the approximate airspeed at which flutter will occur, no analytical solution exists to predict the nature of the LCO response due to its non-linear nature.

All LCOs were induced with a perturbation from rest, except for the cases where $\bar{\omega} =$ 0.67 and $\bar{\omega} =$ 0.71. For these two configurations, the first couple of test points were obtained while the airspeed of the wind tunnel was decreased from the maximum. Whether this corresponds to a subcritical Hopf bifurcation as presented by Dowell et al remains unclear [4]. Data was collected until the intensity of the oscillations was deemed to approach the limits of the experimental rig. The behaviour of the oscillations for almost all configurations resembled well-behaved SHM about a near zero AoA. The offset in the oscillations for coupled flutter induced LCOs was found to fall at or below error, where the maximum offset was calculated to be about 1.3 degrees in pitch, and -0.049 cm in heave for frequency ratios below 1.34. The error in pitch and heave was found to be ±1.4 degrees and ±0.42 cm respectively. In addition, the standard deviation in pitch and heave was calculated to be 0.36 degrees and 0.05 cm respectively.

The most violent oscillations were observed for $\bar{\omega} = 1.34$, where the springs themselves shook so much that it became necessary to use extra securing mechanisms. The error for this case was found to be increased in heave rather than pitch. The values were calculated to be ±0.85 degrees in pitch, and ±1.7 cm in heave (50%). The standard deviation was also increased in heave, where it was determined to be 0.76 cm (25 %), while 0.34 degrees was calculated for pitch. The oscillation offset was calculated to be -4.2 cm in heave. Data recorded at the highest frequency ratio is therefore considered to be the least accurate.

## 3.1.1 Limit Cycle Oscillation Response

Typical results from a coupled flutter induced LCO response are included in Figures 3.1 to 3.5. The configuration presented is for a frequency ratio of 1.01, at an airspeed of 6.95 m/s ($Re_c \sim 7.2 \times 10^4$). Figure 3.1 shows the time history for both pitch and heave. The time response is filtered with a cut-off frequency set at 30 Hz. One can observe well-behaved periodic motion, with constant amplitude oscillation for both pitch and heave. Regarding the spectra (Figures 3.2 and 3.3), the first $2^{16}$ points were used to perform the FFT algorithm, which produced a frequency resolution of 0.0153 Hz.

The most prominent peak in both the pitch and heave power spectral densities (PSDs) correspond to the fundamental frequency of oscillation. The peaks of the super-harmonics are less prominent, as they are a full two decades lower than the fundamental peak. Even super-harmonics indicate asymmetry, while odd super-harmonics indicate non-linear content in the response. Compared to the heave PSD, the pitch frequency spectra contains much more pronounced peaks for super-harmonics beyond *3f*. This indicates that more non-linear content exists in the pitch degree of freedom than in heave. Stronger higher-order peaks were observed in the frequency content of the pitch response, across frequency ratios at similar airspeeds. The histograms of the pitch and heave data indicate clean data, with little asymmetry, indicating SHM-like behaviour. All configurations tested exhibited similar well-behaved response in the histograms.
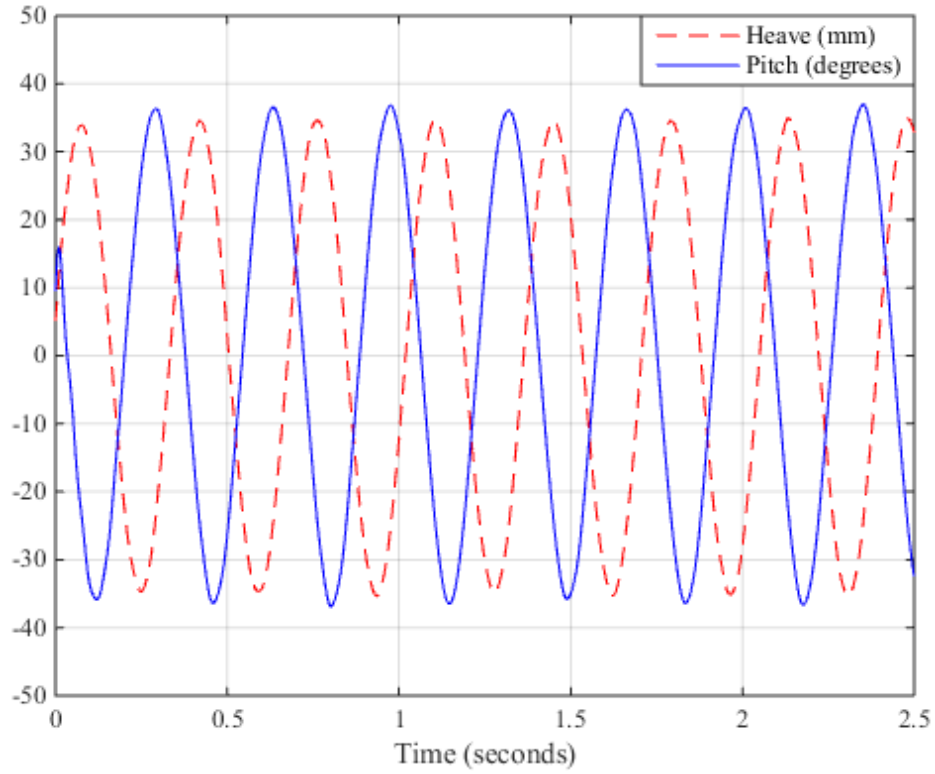
*Figure 3.1: Time-history response of both pitch and heave degrees-of-freedom, for $U_\infty = 6.95$ m/s & $\bar{\omega} = 1.01$ ($Re_c = 7.16 \times 10^4$)*



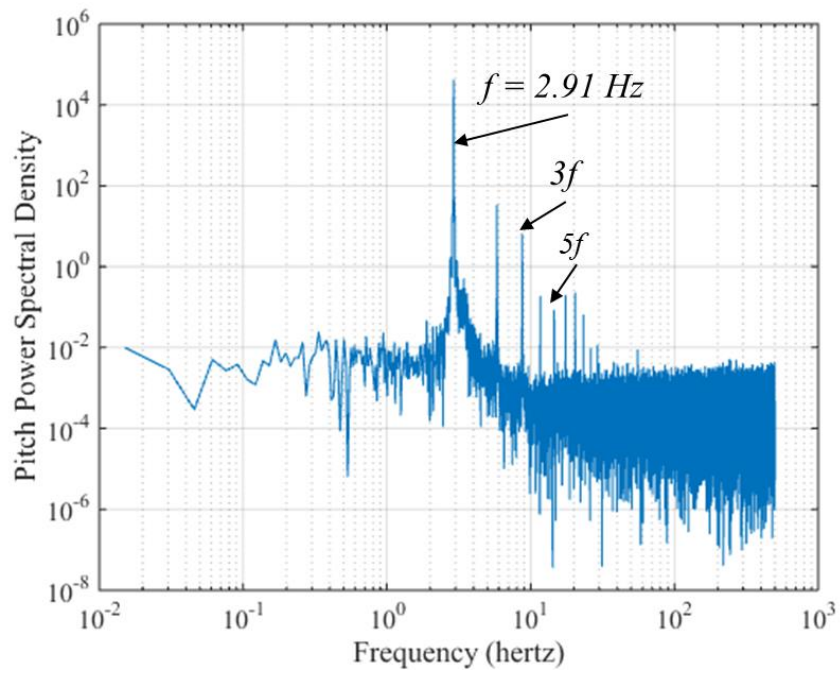*Figure 3.2: Frequency content for pitch response, for $U_\infty = 6.95$ m/s & $\bar{\omega} = 1.01$ ($Re_c = 7.16 \times 10^4$)*
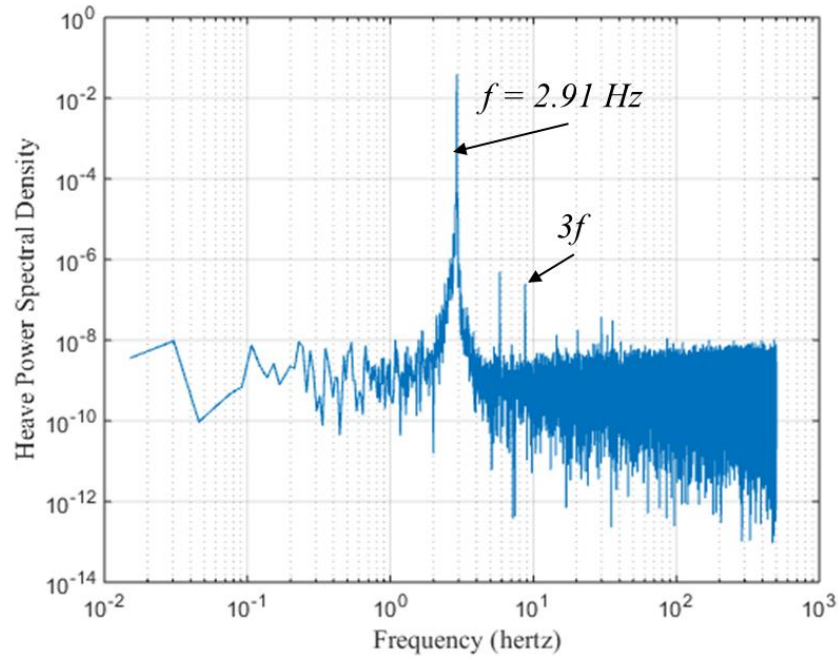
*Figure 3.3: Frequency content for heave response, for $U_\infty = 6.95$ m/s & $\bar{\omega} = 1.01$ ($Re_c = 7.16 \times 10^4$)*
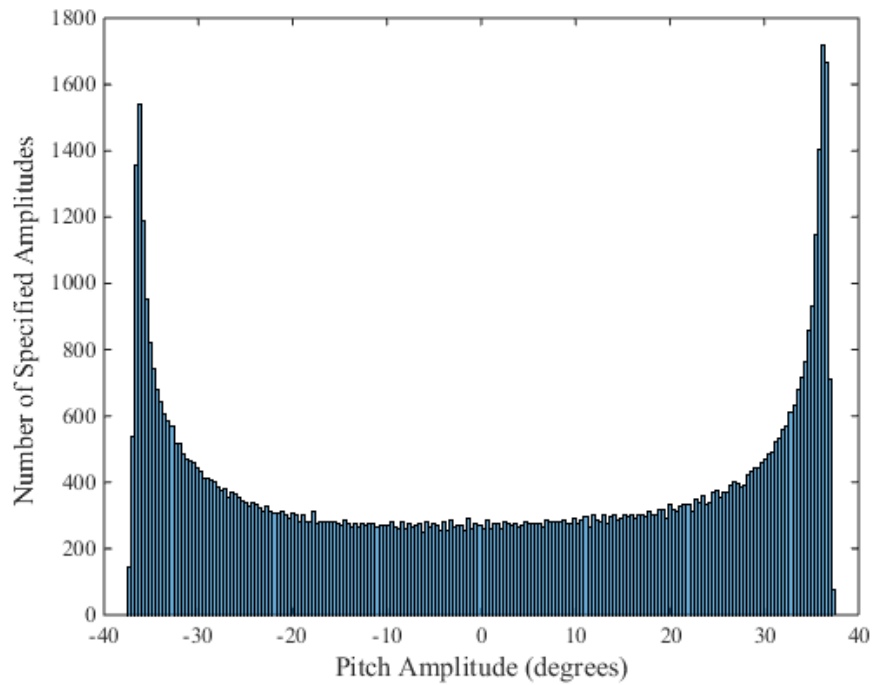


*Figure 3.4: Histogram for pitch data, for $U_\infty = 6.95$ m/s & $\bar{\omega} = 1.01$ ($Re_c = 7.16 \times 10^4$)*
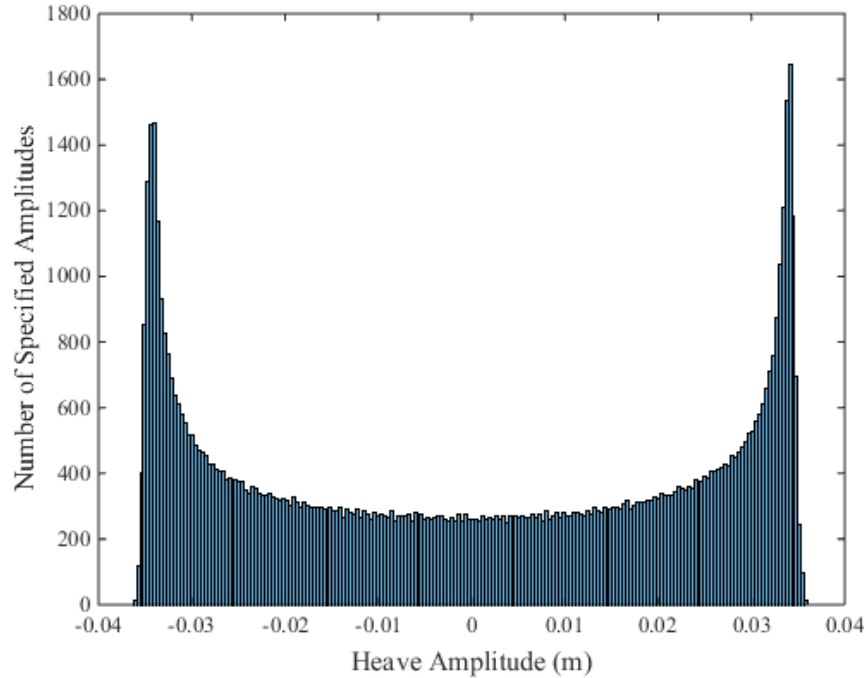
*Figure 3.5: Histogram for heave data, for $U_\infty = 6.95$ m/s & $\bar\omega = 1.01$ ($Re_c = 7.16 \times 10^4$)*

## 3.1.2 Limit Cycle Oscillation Behaviour Sensitivity to Reynolds Number

The pitch amplitude, phase angle, heave amplitude RMS, LCO frequency and reduced frequency (defined in Equation 1.16) values for each frequency ratio are all plotted for the range of Reynolds numbers tested, included in Figures 3.6 to 3.10 respectively. The amplitudes were calculated from the peaks of the calculated histograms from each set of experiments by taking an average of the positive and negative amplitudes. The phase angle was determined from the time difference between the peaks of successive pitch and heave oscillations, with pitch leading. The root-mean-square (RMS) was calculated using heave position data. This was done in order to properly compare with other aeroelastic behaviour, where modulatory responses were observed in the heave response (discussed in Chapter 4). The frequency values were obtained from the dominant peaks in the PSDs for each degree-of-freedom. The phase was determined by finding the average difference between the pitch and heave peaks, with pitch leading as defined in Equations 1.44 and 1.45.

The pitch amplitudes increase with a shallow slope with increasing Reynolds number for coupled flutter induced LCOs occurring at frequency ratios below one. For frequency ratios above one, the pitch amplitude decreases with increasing Reynolds number. It can be inferred that for the majority of the frequency ratios tested, the pitch amplitudes begin to converge to a single value at higher Reynolds numbers, which appears to be around 27°. The phase angle between the degrees of freedom also seems to converge to a value of approximately 160° with increasing Reynolds number, across all frequency ratios. The LCO heave RMS amplitude values

however, increase with Reynolds number for all frequency ratios. Since a 180° phase angle between pitch and heave indicates a forced system, the phase angles may tend towards this stable region with increasing Reynolds number.
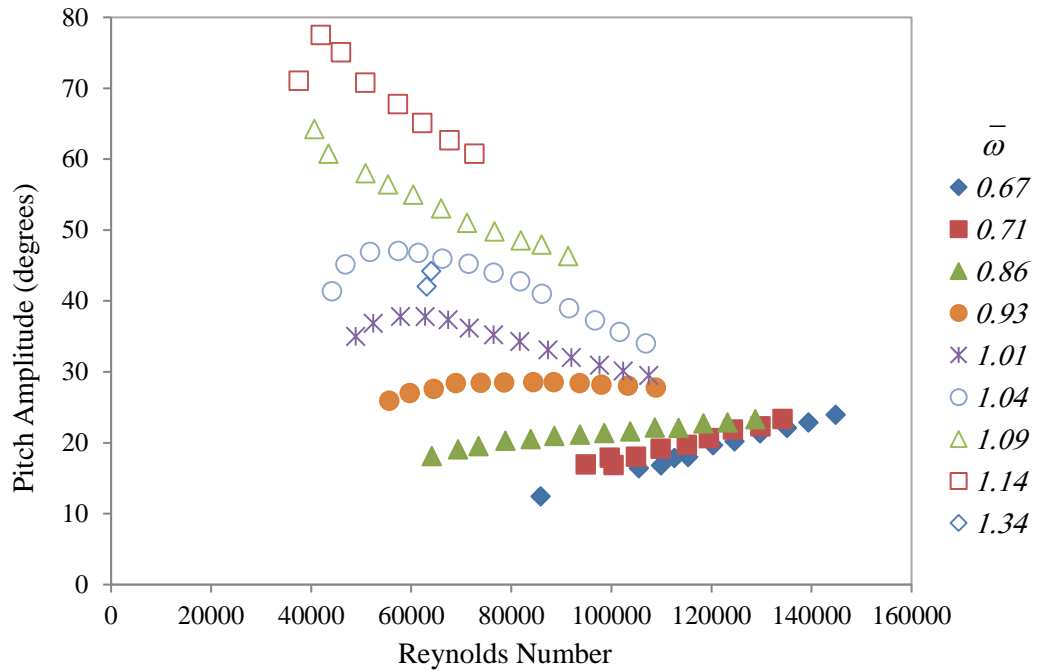


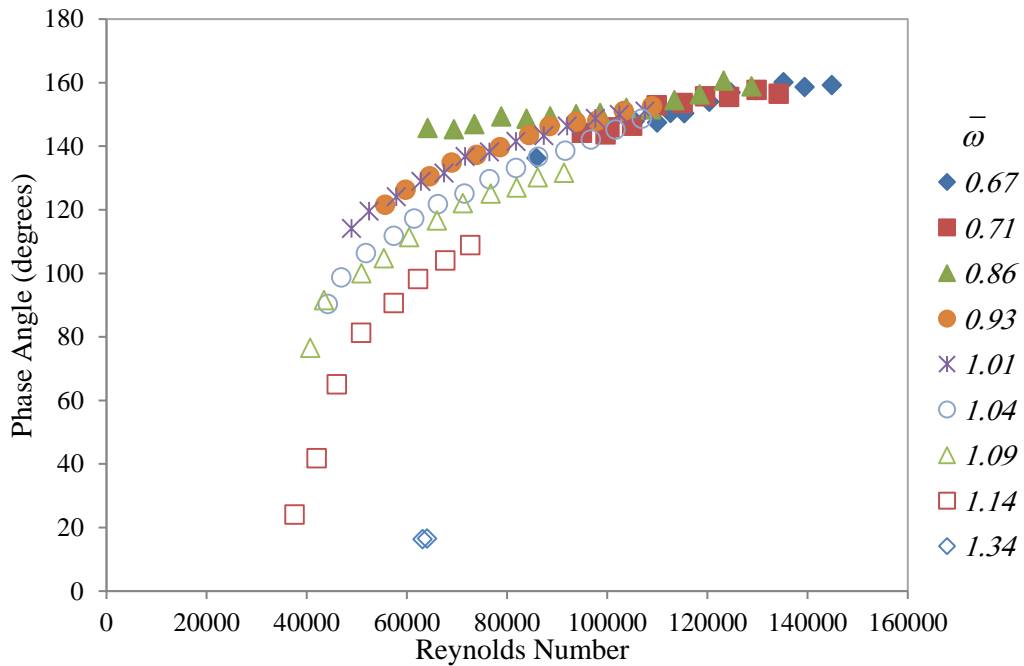*Figure 3.6: Pitch amplitude for each frequency ratio over increasing Reynolds Numbers.*



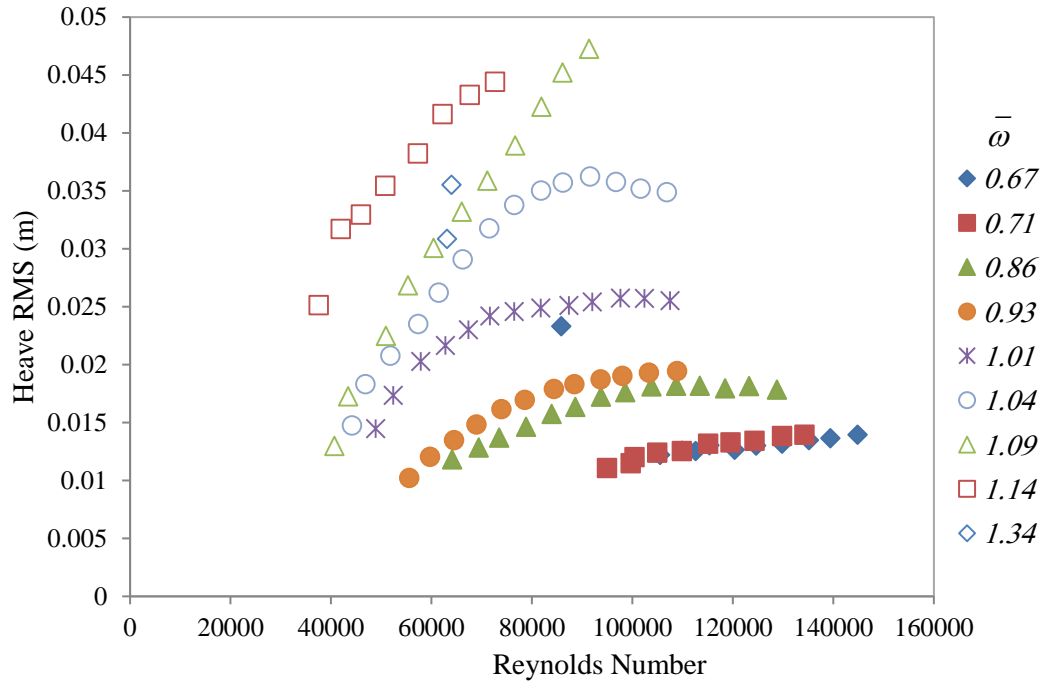*Figure 3.7: Phase angle between pitch and heave oscillations over Reynolds Number*

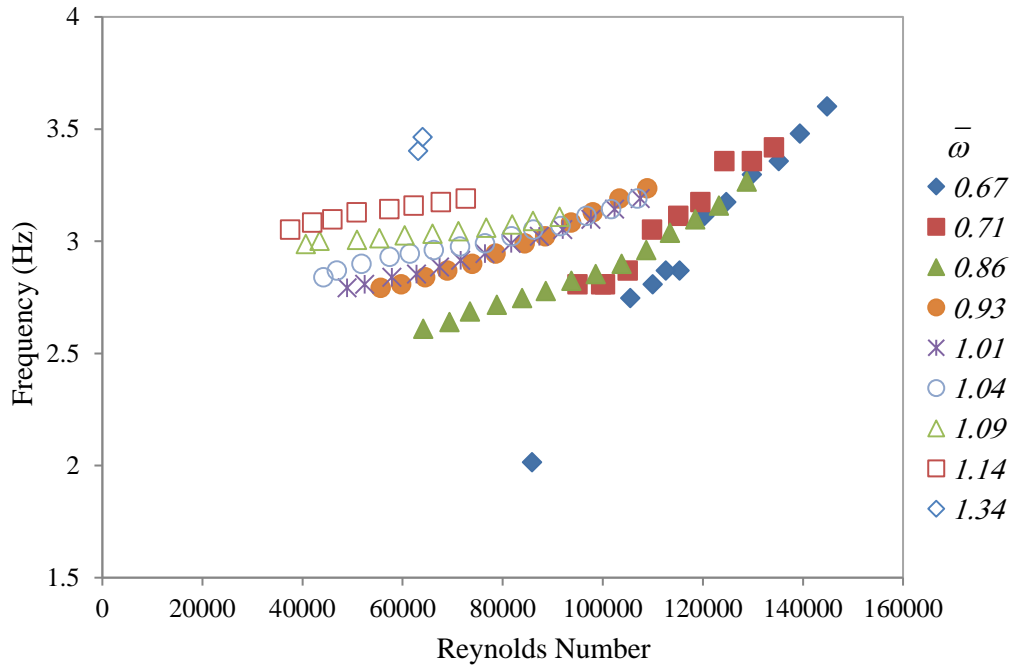*Figure 3.8: Heave RMS for each frequency ratio over increasing Reynolds Numbers.*



*Figure 3.9: LCO frequency for each frequency ratio over increasing Reynolds Numbers.*
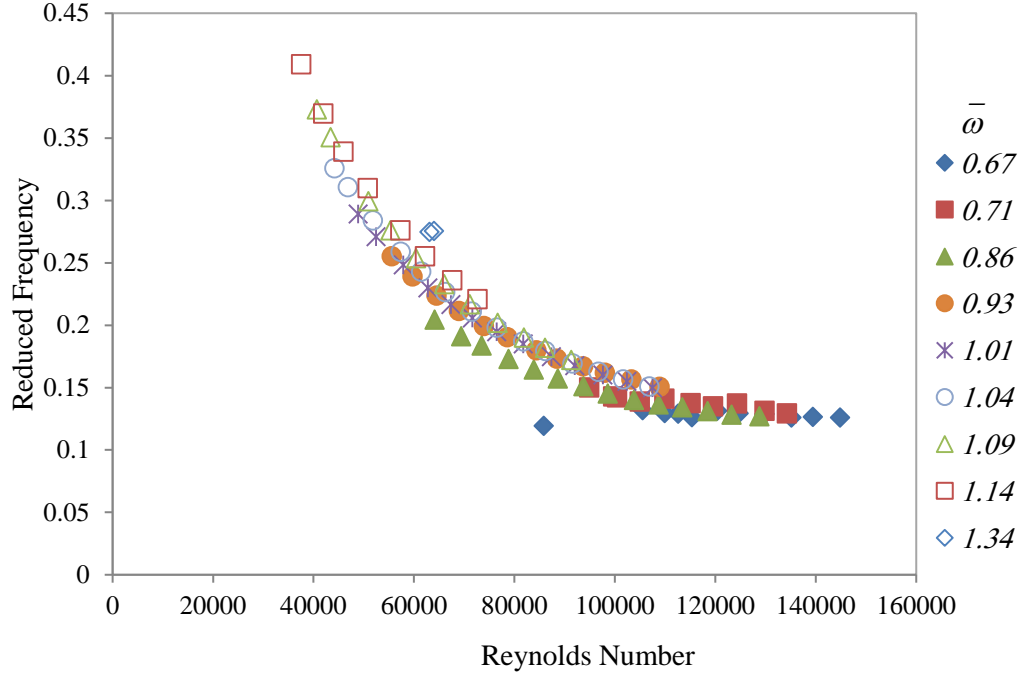
*Figure 3.10: Reduced frequency for each frequency ratio over increasing Reynolds Numbers.*

The observations in our study stand in contrast to the coupled flutter induced LCO response observed by Pigolotti et al. [21]. They observed the heave and pitch amplitude value branches increasing with airspeed and originating from a common point, that one may determine by extrapolating the sub-critical branches down to a null-amplitude. This behaviour was not seen in our study. The behaviour of LCO pitch amplitude with Reynolds number dos not follow the supercritical Hopf bifurcation trend described by Dowell et al., where in Figure 3.6 branches are seen to decrease with increasing Reynolds number for configurations with frequency ratios above one, and seem to converge to a common value [4]. It is unclear whether the heave RMS amplitude branches in Figure 3.8 originate from a null-amplitude common Reynolds number, without data points at lower airspeeds. Also unlike the study conducted by Pigolotti, oscillations did not become in-phase for oscillations above a frequency ratio of one.

Similar to the behaviour for the heave RMS, the LCO frequency also increases with increasing Reynolds number. Unlike the heave RMS behaviour, the LCO frequency values tend to converge to a single value with increasing Reynolds number. The behaviour for the reduced frequency also tend towards a constant value with increasing Reynolds number. Moreover all reduced frequency values collapse across all frequency ratios. The values decrease with increasing Reynolds number, and tend to a value of about 0.1. The reduced frequency values are well above 0.05, indicating a high level of unsteadiness in the LCO response.

## 3.2 Analytical Results

The analytical flutter speeds for the experimental configurations tested were calculated using a 3DOF linear aeroelastic model, the third degree-of-freedom representing unsteady aerodynamics. The unsteady model uses Wagner's function for aerodynamic lag, as defined in section 1.4.4. The justification for using the unsteady model is based on the experimental reduced frequency values for each test case, all of which are well above 0.05 and indicate a high level of unsteadiness. In order to maintain consistency between results, uniform structural damping constants were assumed, where $D_h = 2$ Ns/m and $D_\theta = 0.0011$ Nms/rad taken as averages from each test case. This was done because analytical flutter results were sensitive to varying the structural damping values.

As shown in Figure 3.11 the calculated flutter speeds are plotted against the first appearance of the experimental LCO for varying frequency ratios. The characteristic reduction in the flutter speed at a frequency ratio close to one as described by Theodorsen can be observed in both the experimental and analytical results [20]. It can be seen that there is some correlation between prediction and experiment. For frequency ratios below one, analytical predictions underestimate the experimental flutter speed. On the other hand, the experimental flutter speed is advanced for frequency ratios above one. This is consistent with the non-linear torsional stiffening effect of laminar separation flutter, as described by Poirel and Mendes for transitional Reynolds numbers [13]. The effects of torsional stiffening are not included in this analysis. For frequency ratios below one, torsional stiffening due to laminar separation increases the stiffness in pitch, therefore increasing the apparent frequency ratio and postponing the onset of flutter. A stiffening in pitch for frequency ratios above one decreases the apparent frequency ratio, and flutter occurs at airspeeds lower than predicted. Discrepancies between trends may also arise due to the variation in the true structural damping constants between configurations, as well as error associated with the frequency ratio for each spring set. The lowest calculated flutter speed occurs at a frequency ratio of 1.01, whereas experimentally this occurred at a slightly higher frequency ratio of 1.14.

Plots of the eigenvalues versus airspeed from the linear analysis for frequency ratios of 0.67, 1.01 and 1.14 are included in Figures 3.12 to 3.14. The graphs presenting the eigenfrequencies show the heave and pitch dominated branches, where the pitch-dominated branch crosses the x-axis close to the analytical divergence speed. The experimental LCO frequencies are also included in the eigenfrequency plots. The experimental frequencies do not correspond to linear predictions in the post-flutter region, indicating a high degree of non-linearity in the experimental LCO responses, and probable influence of large leading-edge separation on limiting LCO amplitudes.

The decay-rate includes five branches. The branch that first crosses the x-axis for each frequency ratio is the heave dominated branch, as such the calculated unstable mode for each frequency ratio is the heave dominated one. The slope of the negative decay-rate branch

associated with the heave-dominated mode does not vary much between configurations and is observed to be shallow for all cases. It is thus observed that the predicted nature of the flutter is soft, rather than explosive.
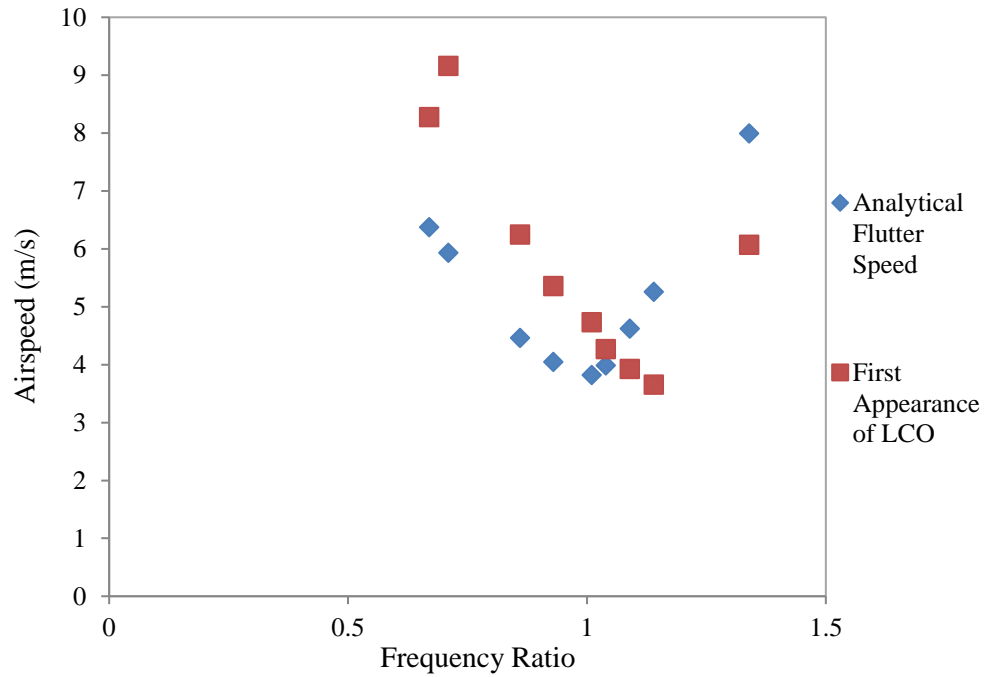


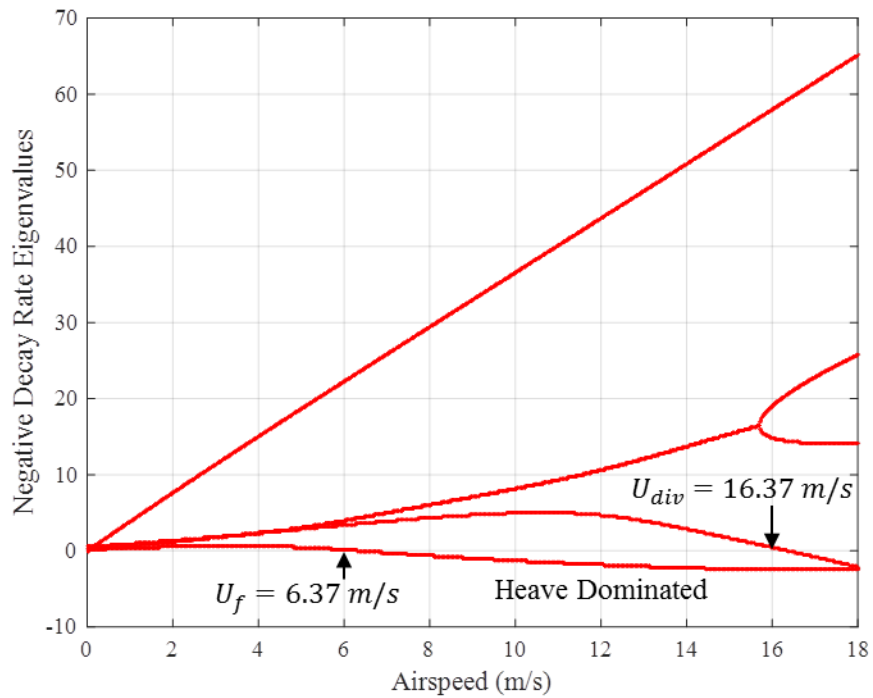*Figure 3.11: Numerically predicted and experimental onset of coupled flutter induced LCOs.*



*Figure 3.12A: Calculated decay rate eigenvalues for a range of airspeeds, $\bar{\omega} = 0.67$.*
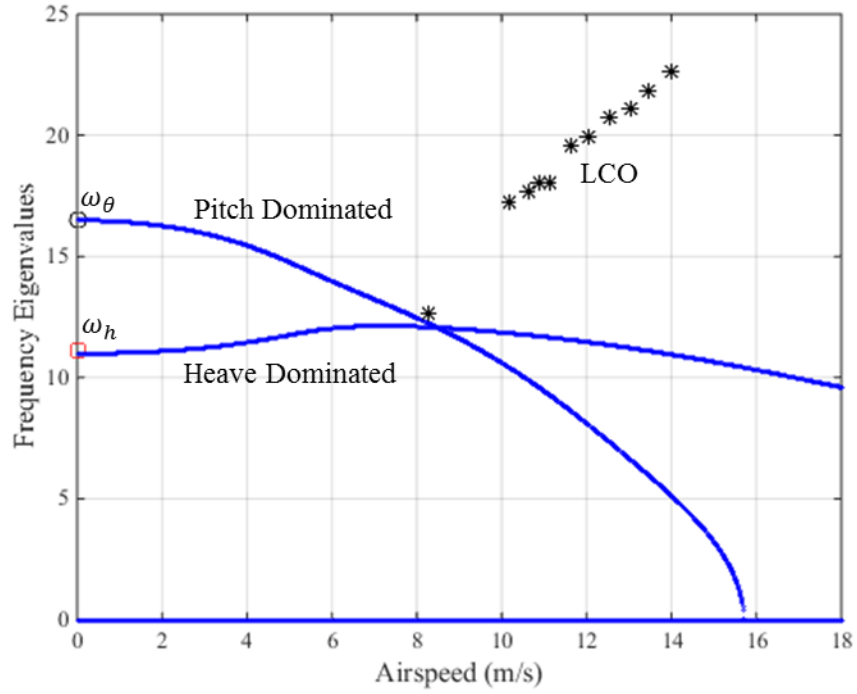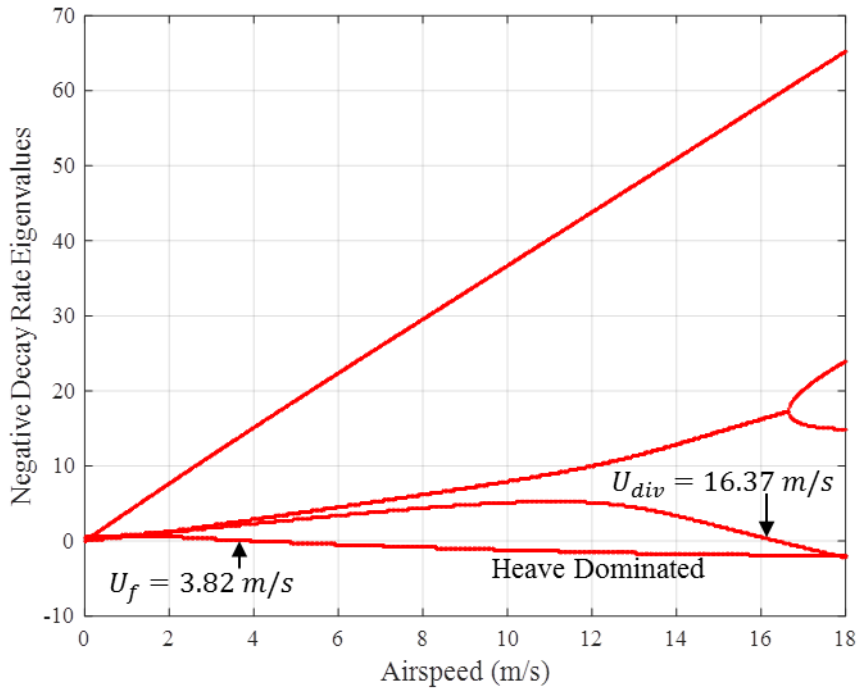
*Figure 3.12B: Calculated frequency eigenvalues for a range of airspeeds, $\bar{\omega} = 0.67$.*



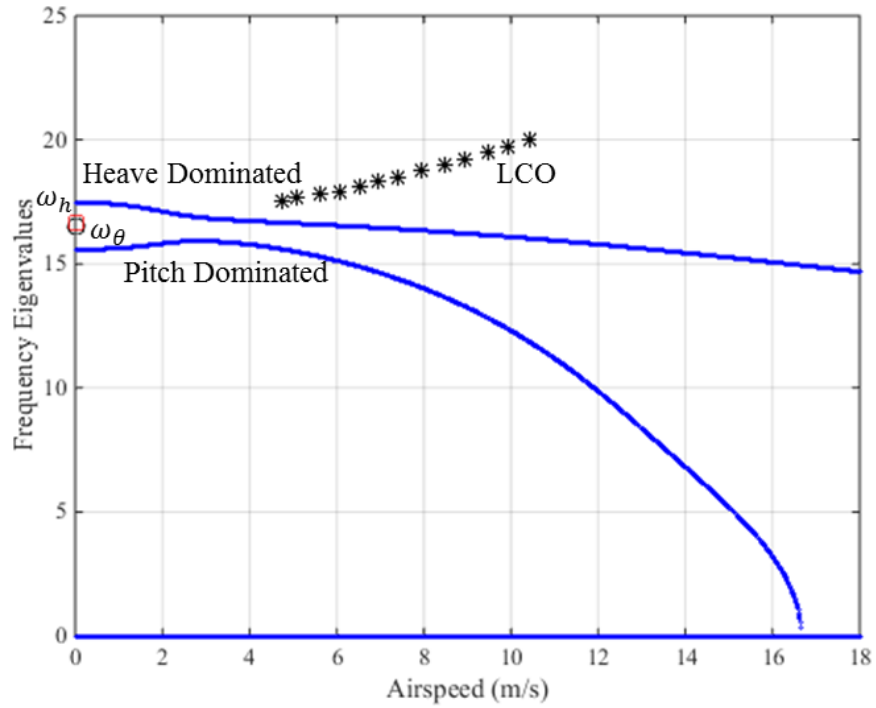*Figure 3.13A: Calculated decay rate eigenvalues for a range of airspeeds, $\bar{\omega} = 1.01$.*

*Figure 3.13B: Calculated frequency eigenvalues for a range of airspeeds, $\bar{\omega} = 1.01$.*
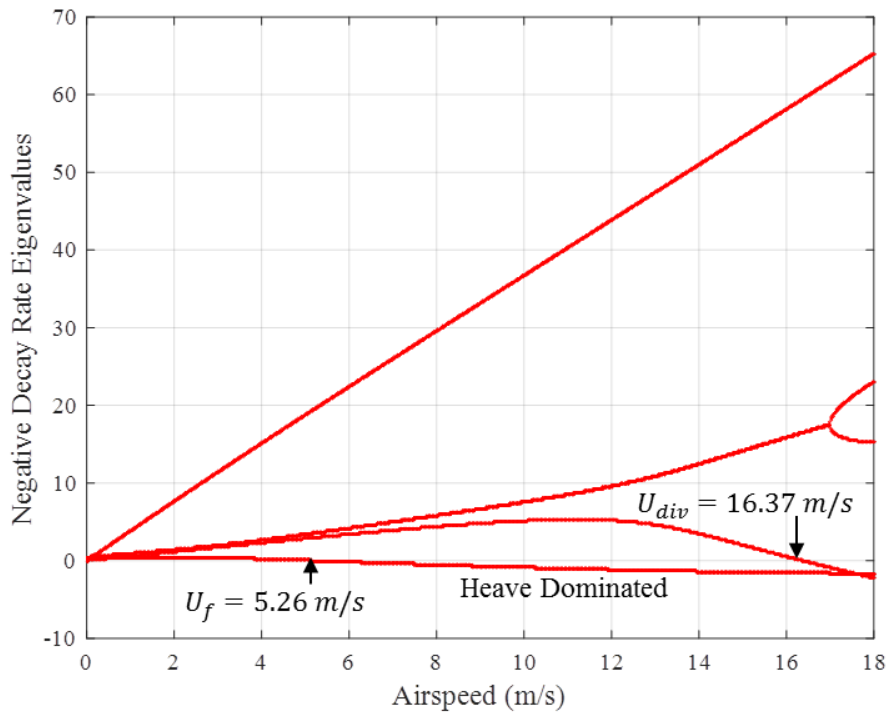


*Figure 3.14A: Calculated decay rate eigenvalues for a range of airspeeds, $\bar{\omega} = 1.14$.*
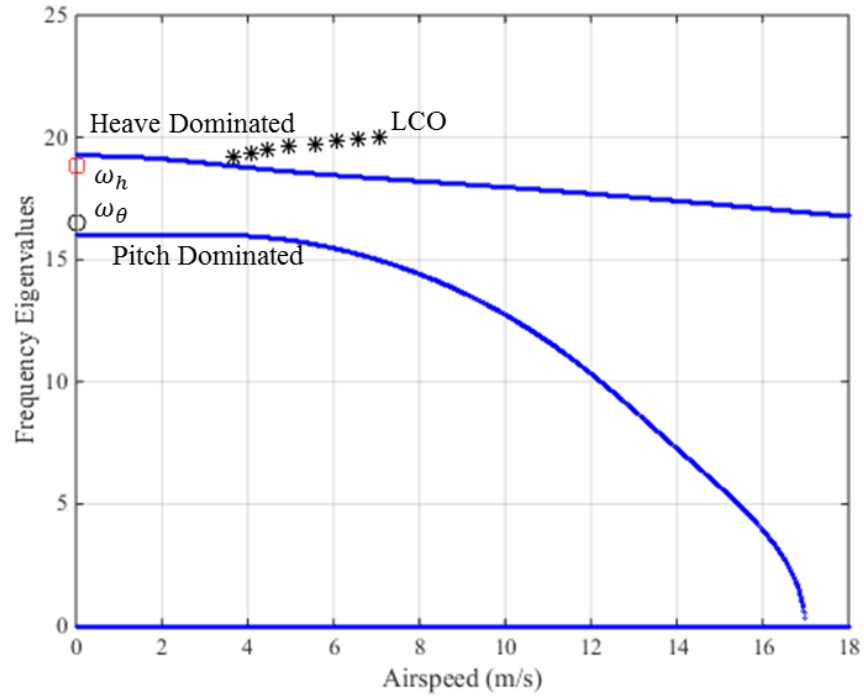
*Figure 3.14B: Calculated frequency eigenvalues for a range of airspeeds, $\bar{\omega} = 1.14$.*

The Eigenfrequency at the analytical flutter speed was taken from the heave-dominated branch for each frequency ratio. These were plotted with the experimental LCO frequencies in Figure 3.15. As can be observed, some correlation occurs, indicating the heave-dominated mode as being the unstable mode. Some discrepancies occur, most notably at a frequency ratio of 0.71. This point may not correspond to the analytical onset of LCO at this frequency ratio due to the delay in the experimental flutter speed associated with the stiffening effect of the LSB. The decay rate of the pitch-dominated branch also becomes negative at the analytical divergence speed. The two upper decay-rate branches in the results correspond to the aerodynamic degrees-of-freedom.
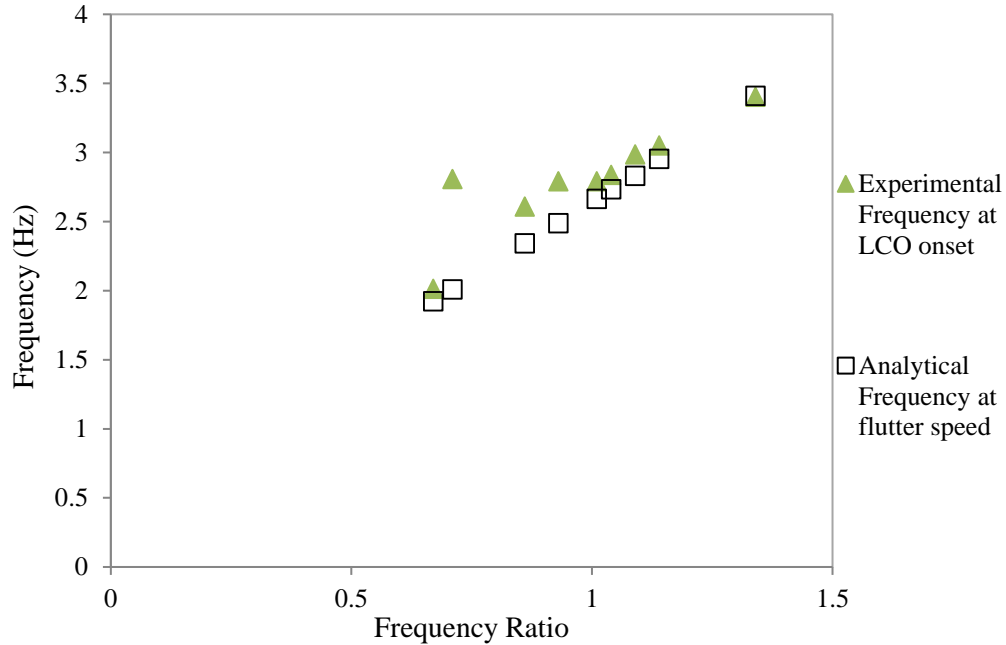
*Figure 3.15: Analytical and Experimental LCO frequency at onset of coupled flutter induced LCOs.*

## 3.3 Aerodynamic Load Analysis

The aerodynamic moment and lift coefficients were calculated for frequency ratios of 0.86. 1.01 and 1.14, at similar airspeeds ($Re_c \sim 7.2 \times 10^4$, $U_\infty \sim 6.9$ m/s). From the filtered position data, the velocity and acceleration for both the pitch and heave degrees of freedom were determined by using a five-point differentiation scheme [35]. In order to remove unwanted noise from high frequency content, the position data was filtered just above the *7f* super-harmonic. Lower cut-off frequencies seemed to omit important information in the responses. At the same time, the behaviour of the calculated moment did not change significantly if higher frequency content was included.

Knowing the moment of inertia, mass, structural damping and stiffness terms for each test case, the lift and moment is evaluated at each time-step using equations 1.2 and 1.3 defined in section 1.4.1. These equations of motion are re-stated below for reference. The calculated aerodynamic moment and lift were phase-averaged for at least 60 cycles, to produce more interpretable plots. Moment coefficient results are thus plotted with pitch position, and the lift coefficient with heave in Figures 3.16 to 3.18. The average work over each cycle was determined for each aerodynamic load calculated from experiment, and included in each plot. In addition, SHM equations based on the amplitude and frequency results were used in Theodorsen's equations to obtain the analytical linear behaviour. The static linear moment curve is also included in the moment plots for reference.

$$M_h \ddot{h} - \frac{M_\theta c x_\theta}{2} \ddot{\theta} + D_h \dot{h} + K_h h = L \qquad\qquad [1.2]$$

$$I_{EA} \ddot{\theta} - \frac{M_\theta c x_\theta}{2} \ddot{h} + D_\theta \dot{\theta} + K_\theta \theta = M_{EA} \qquad\qquad [1.3]$$

A high degree of variation exists between the moment coefficient curves for different frequency ratios. Hysteresis effects associated with non-linear dynamics can be observed, where clockwise and counter-clockwise regions both exist in the moment curves. As discussed in Chapter 1, the clockwise regions in both moment and lift curves indicate instability, and positive work (+W) being done on the structure. Counter-clockwise loops indicate stable regions (-W). While linear models can give an indication of the onset of flutter, the importance of non-linear dynamics on the subsequent LCO response becomes apparent when comparing the behavior of these curves with those predicted using linear assumptions. While regions of positive work exist in the aerodynamic moment, the majority of the LCO cycle seems to be comprised of stable regions of negative work. This is confirmed when calculating the contribution of work due to the aerodynamic moment, where the total work done by the aerodynamic moment is negative.

The lift in heave is also influenced by non-linear effects, as the curves do not follow regular elliptical shapes. However, the lift response is not as strongly non-linear as the moment with pitch. This corresponds to the reduced odd super-harmonic content found in the frequency content in heave. All lift responses follow the same clockwise direction as the predicted behaviour from Theodorsen's equations. While the moment curves comprise of mostly stable regions, the clockwise loops of positive work indicate that the majority of the work is done by the aerodynamic lift in heave. A similar observation was noted by Poirel and Mendes regarding 2DOF SAOs in pitch and heave [13]. The overall work done by the aerodynamic loads is positive, indicating that the flow feeds the LCO.
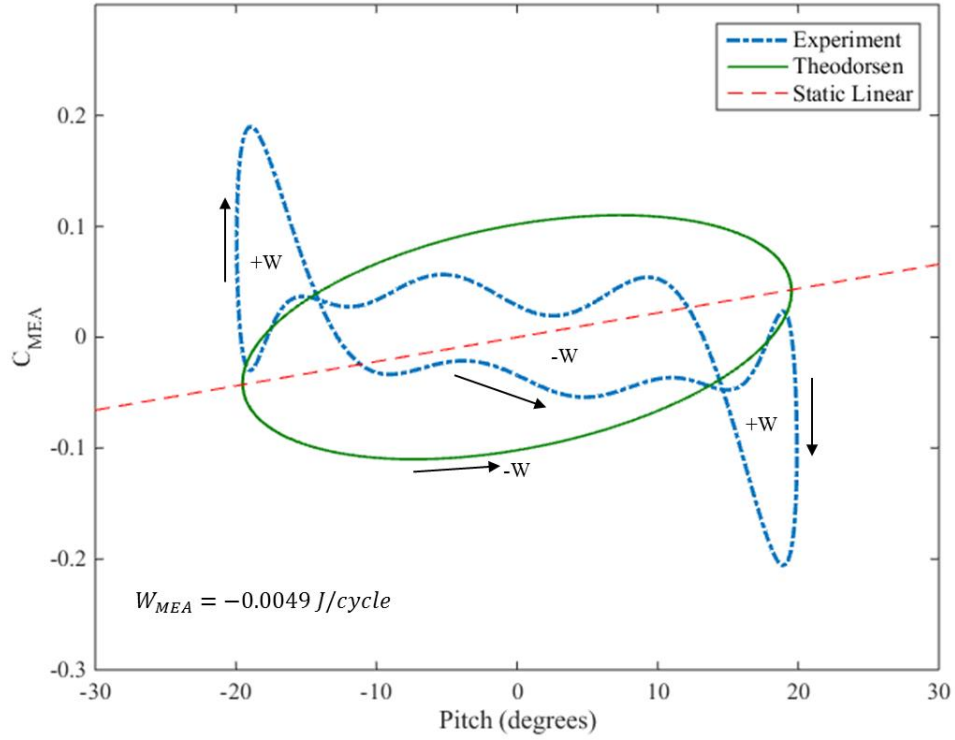
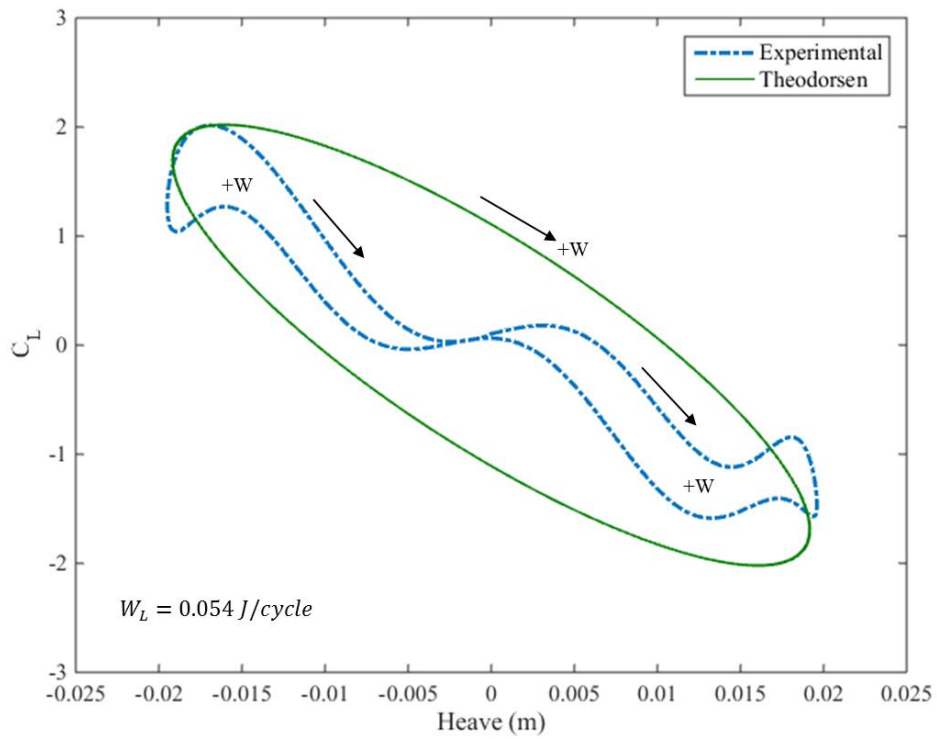*Figure 3.16A: Aerodynamic moment coefficient over pitch response, for $U_\infty$ = 7.17 m/s & $\bar{\omega}$ = 0.86.*



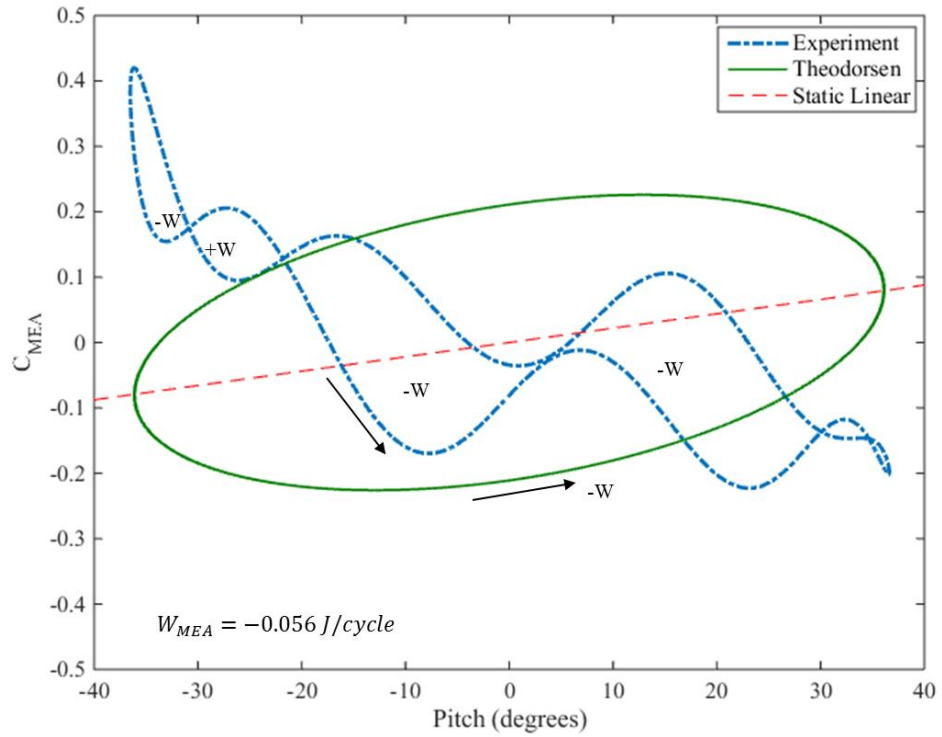*Figure 3.16B: Aerodynamic lift coefficient over heave response, for $U_\infty$ = 7.17 m/s & $\bar{\omega}$ = 0.86.*

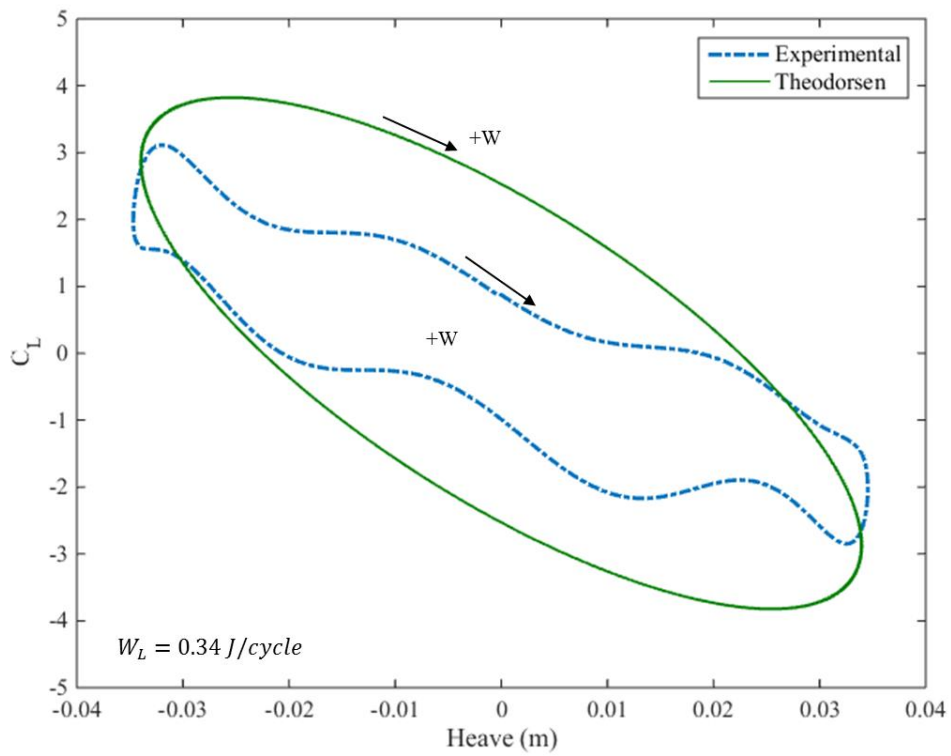*Figure 3.17A: Aerodynamic moment coefficient over pitch response, for $U_\infty = 6.95$ m/s & $\bar{\omega} = 1.01$.*



*Figure 3.17B: Aerodynamic lift coefficient over heave response, for $U_\infty = 6.95$ m/s & $\bar{\omega} = 1.01$.*

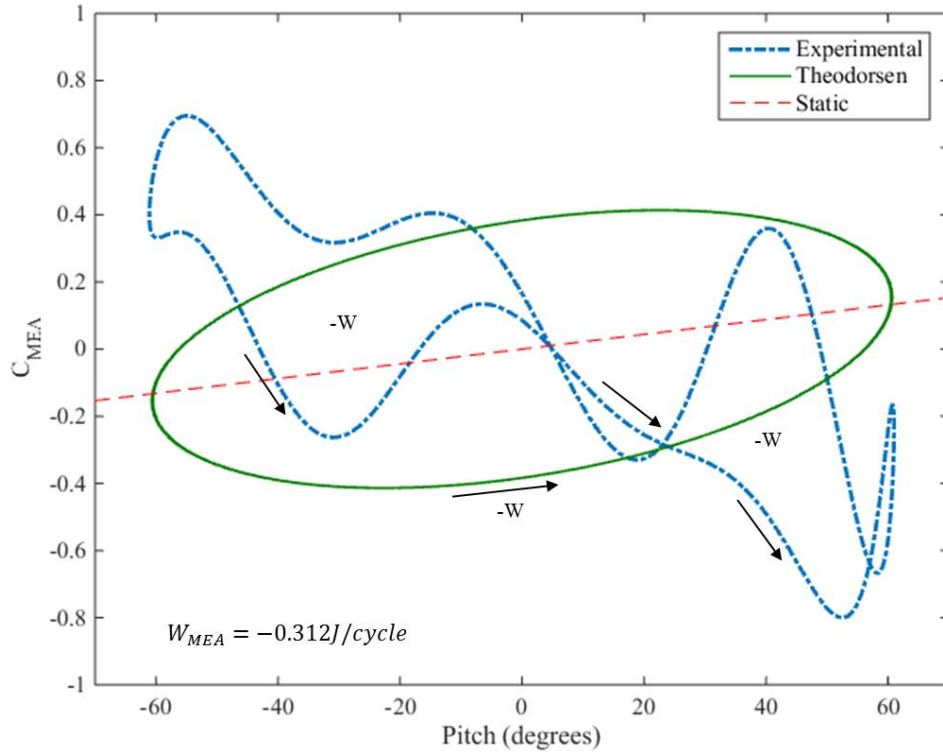*Figure 3.18A: Aerodynamic moment coefficient over pitch response, for $U_\infty$ = 7.08 m/s & $\overline{\omega}$ = 1.14.*
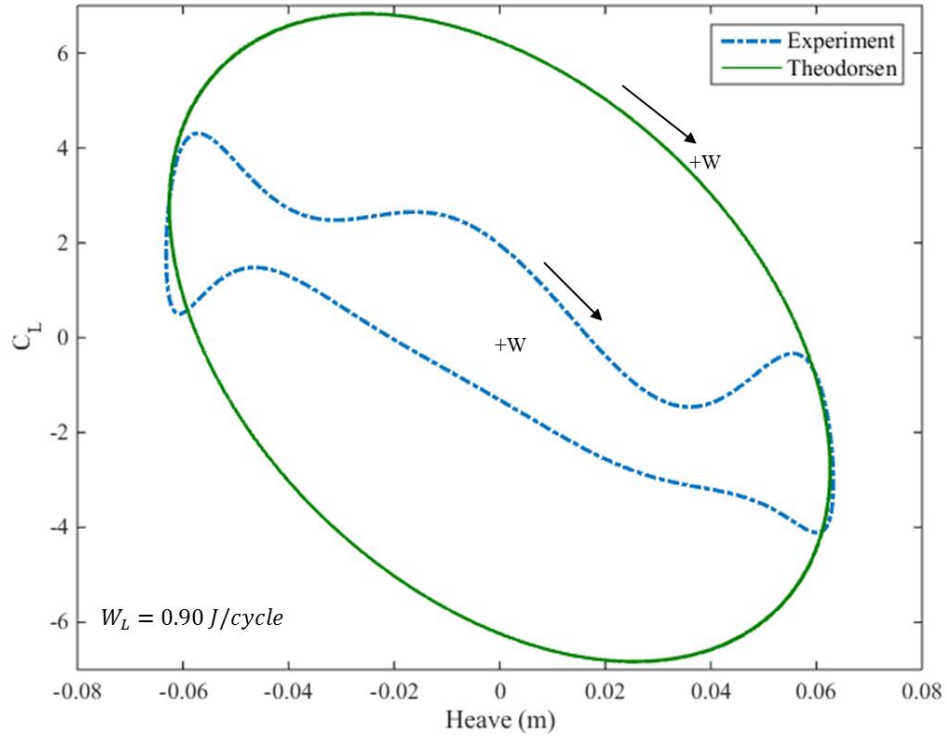


*Figure 3.18B: Aerodynamic lift coefficient over heave response, for $U_\infty$ = 7.08 m/s & $\overline{\omega}$ = 1.14.*

## 3.4 Energy Calculations

The cycle averaged work and power, as well as kinetic energy were calculated using the analytical methods outlined in section 1.6. The experimental moment and lift at each time step were used in Equation 1.47, the power being averaged over a number of cycles. Calculations were performed for at least 120 cycles. The efficiency was calculated using the definition outlined by Kinsey and Dumas in section 1.6. The equations are re-stated below for reference. As can be observed in Figure 3.19, the behaviour of the kinetic energy follows the trend of the heave RMS in Figure 3.8. As the majority of the work is done by the aerodynamic lift in heave, the heave kinetic energy constitutes the majority of the energy of the LCO. The aerodynamic efficiency follows a trend similar to the pitch amplitude, with all values decreasing and converging with increasing Reynolds number. The energy extracted by the system may also decrease as it approaches a forced, or stable regime. This correlates with the trend of phase angle between the 2DOFs with increasing Reynolds number, as it tends to converge towards 180°.

The highest values in aerodynamic efficiency were found to occur at the lowest airspeeds tested for frequency ratios just above one, at the onset of coupled flutter induced LCOs. Efficiency values close to 45% at an airspeed of about 4.0 m/s ($Re_c \sim 4.0 \times 10^4$) were observed. These values exceed those found in literature for a single wing experimental configuration, the most noted being 34% by Kinsey and Dumas [8]. The rapid drop in efficiency may be due to the fact that the oscillation frequency does not increase as quickly as the heave amplitude which influences the projected swept area. Therefore, the power extracted which is analytically dependant on the frequency squared, does not increase as quickly as the power available in the flow of the projected area.

$$\bar{P} = \frac{1}{T} \int_t^{t+T} \left[ M_{EA}\dot{\theta} + L\dot{h} \right] dt \qquad\qquad [1.47]$$

$$P_a = \frac{1}{2}\rho U_\infty^3 ld \qquad\qquad [1.50]$$

$$\eta = \frac{\bar{P}}{P_a} \qquad\qquad [1.49]$$

$$\overline{KE} = \frac{1}{T}\int_0^T \frac{M_h \dot{h}_{CG}^2}{2} dt + \frac{1}{T}\int_0^T \frac{I_{CG}\dot{\theta}^2}{2} dt \qquad\qquad [1.51]$$
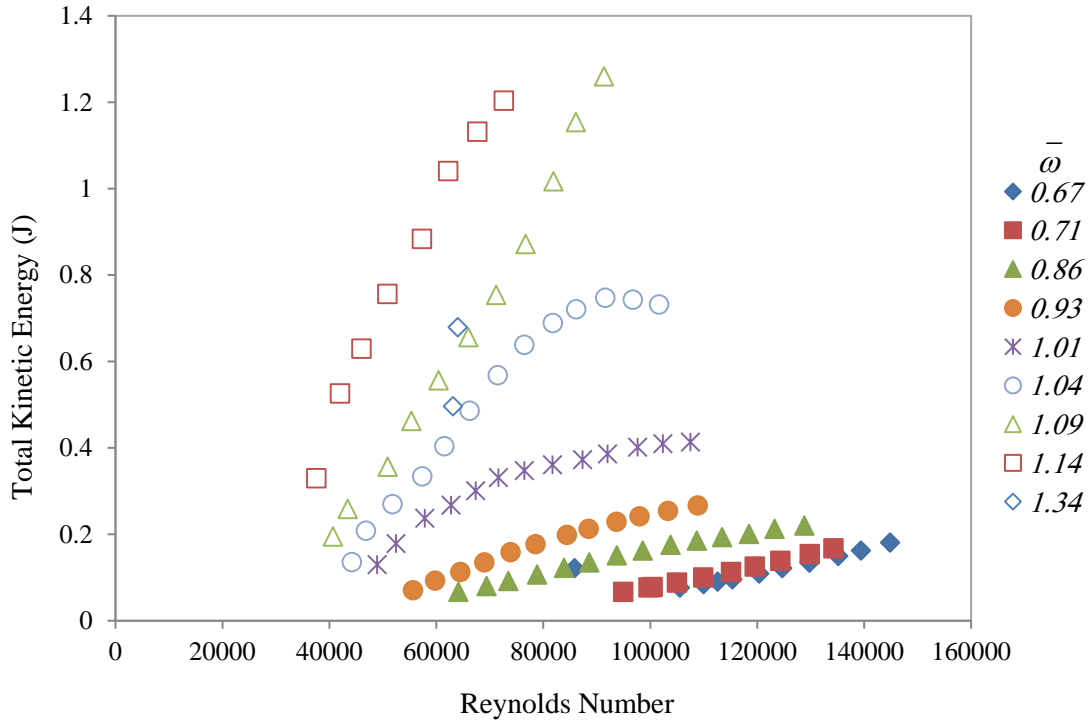
*Figure 3.19: Kinetic energy sum of pitch and heave oscillations for each frequency ratio tested, for increasing Reynolds Numbers*
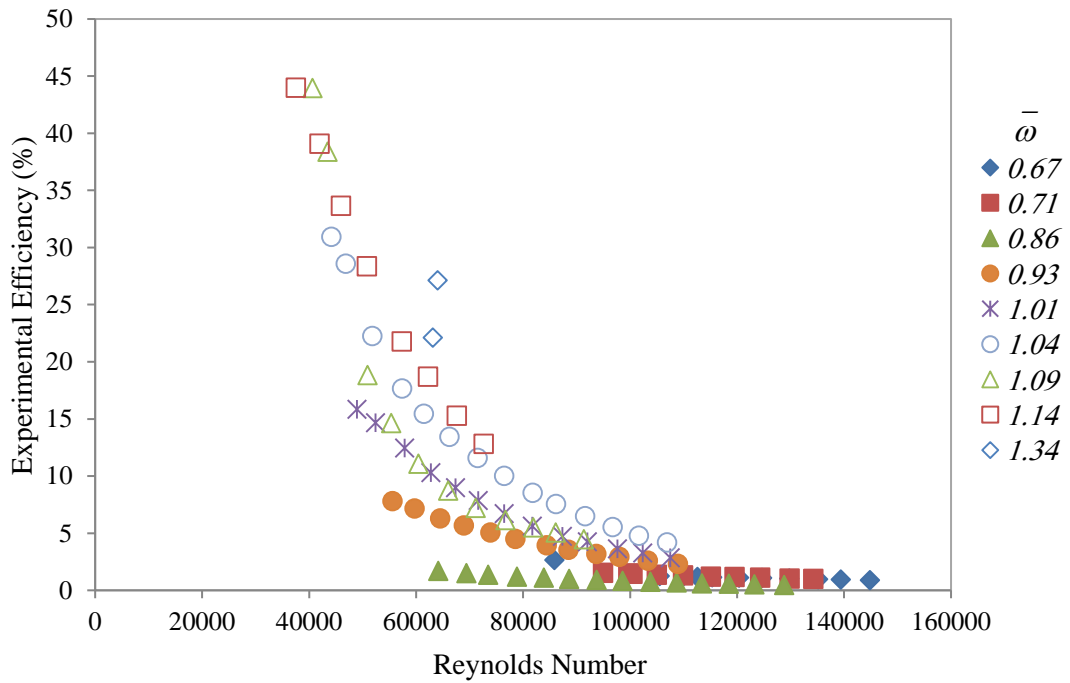


*Figure 3.20: Aerodynamic efficiency of each frequency ratio tested, for increasing Reynolds Numbers*

# Chapter 4 – Stall Flutter

When the elastic axis is moved aft to 0.35c, pitch driven large amplitude LCOs due to stall flutter appear. This is the focus of this chapter. In addition, other aeroelastic phenomena including SAOs, occur within the airspeeds tested for this configuration. Section 4.1 in this chapter includes an overview of the various 1DOF aeroelastic phenomenon observed within this transitional Reynolds numbers regime, where the heave was constrained. For the remaining sections the emphasis of the analysis is on both the 1DOF and 2DOF large amplitude LCOs. It is important to note that the center of mass is almost coincident with the EA, giving a very small value for the static imbalance, where $x_\theta = 0.004$. This indicates that the structural system is essentially uncoupled, and that any coupling occurs from the aerodynamics.

## 4.1 Multiple Stable Attractors in One-Degree-of-Freedom

Experiments were conducted for 5.4 m/s $\leq U_\infty \leq$ 12 m/s (5.7×10$^4 \leq Re_c \leq$ 1.3×10$^5$) in 1DOF in pitch. The error in the airspeed was estimated to be ±0.7 m/s. Note that the analytical divergence speed of the airfoil using a pitch spring stiffness set at 0.3 Nm/rad was calculated to be 7.3 m/s, using Equation 1.32. Similar to the study conducted by Dimitriadis and Li, but unlike the experiments conducted for Chapter 3 for coupled flutter, the predicted divergence speed fell within the range of airspeeds tested [24]. Note as well that no coupled flutter is predicted (analytically) for this configuration.

Similar to previous studies investigating stall flutter, multiple attractors coexist in 1DOF within the range of airspeeds tested for the constant pitch stiffness mentioned. For airspeeds below approximately the divergence airspeed, all perturbations would decay to a static equilibrium at zero AoA. After 7.3 m/s however, both static and dynamic aeroelastic phenomena appeared. Small amplitude oscillations associated with low-Reynolds number effects, occurred with small perturbations (~5°) for 7.8 m/s $\leq U_\infty \leq$ 9.3 m/s. No clear signs of divergence were observed, however non-zero equilibrium positions were seen to follow the static bifurcation behaviour occurring from the effects of non-linear static aerodynamics past the divergence airspeed. The main reason was theorized to be a result of the non-linear static stiffening in pitch due to the appearance of an LSB at these Reynolds numbers, as indicated previously by Poirel and Mendes [13]. This stands in contrast to the results obtained by Dimitriadis and Li [24], where SAOs were not observed, and static non-linear behaviour associated with the LSB was not present. The absence of low-Reynolds number effects in their study is thought to be related to higher turbulence levels in the free-stream airflow [24]. Also unlike the aforementioned study, no asymmetric oscillations were observed past the theoretical divergence speed. It is thus theorized that the absence of asymmetric LCOs could be related to the stiffening in pitch as a result of low-Reynolds number effects.

Specifically, four stable attractors were observed within a range close to 8 m/s. A qualitative schematic of the aeroelastic behaviour observed within the airspeeds tested is included in Figure 4.1. A time-history plot at 8 m/s is included in Figure 4.2, showing multiple aeroelastic phenomenon for the same airspeed tested. Large amplitude LCOs were observed for very large perturbations after 7.3 m/s. The perturbation in pitch required to induce large amplitude LCOs decreased in value with increasing airspeed, on the order of ~20°, until about 11.7 m/s. For airspeeds beyond 11.7 m/s, no perturbation was needed to induce large amplitude LCOs.
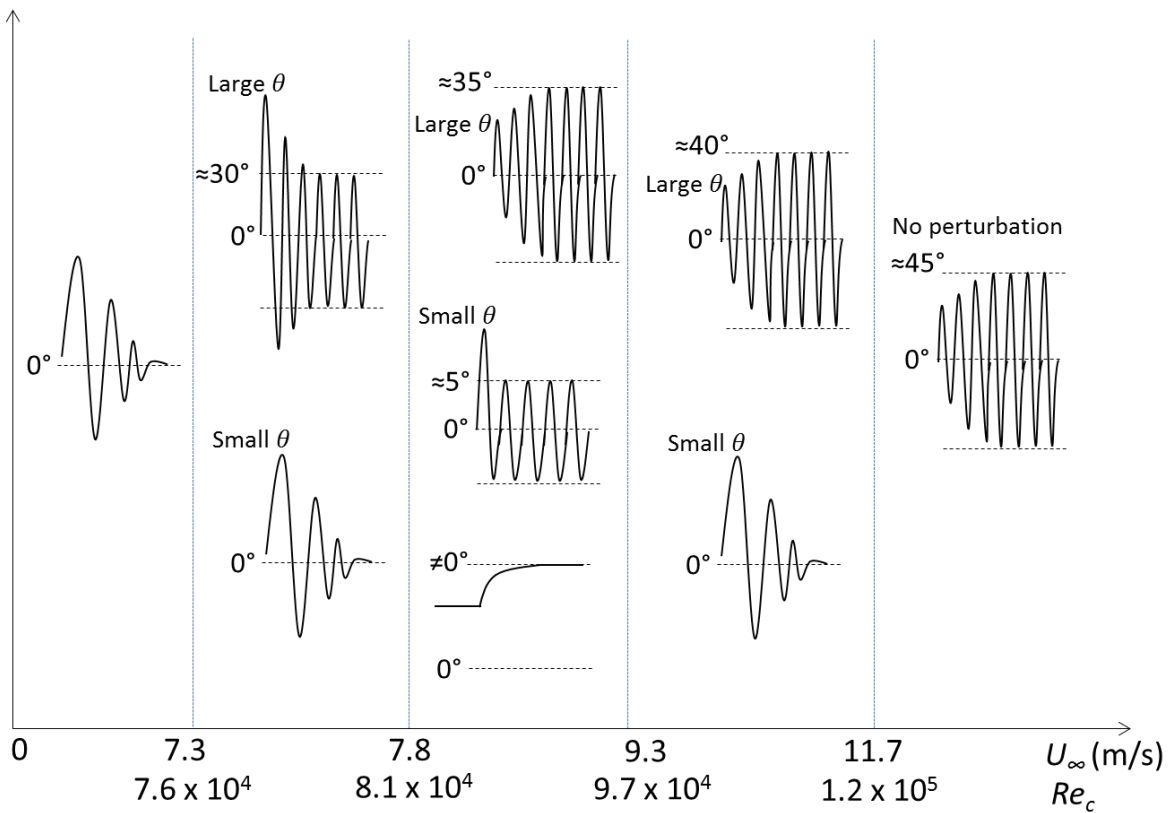


*Figure 4.1: Schematic of attractors observed within each sub-range of airspeeds tested. Taken from [18].*
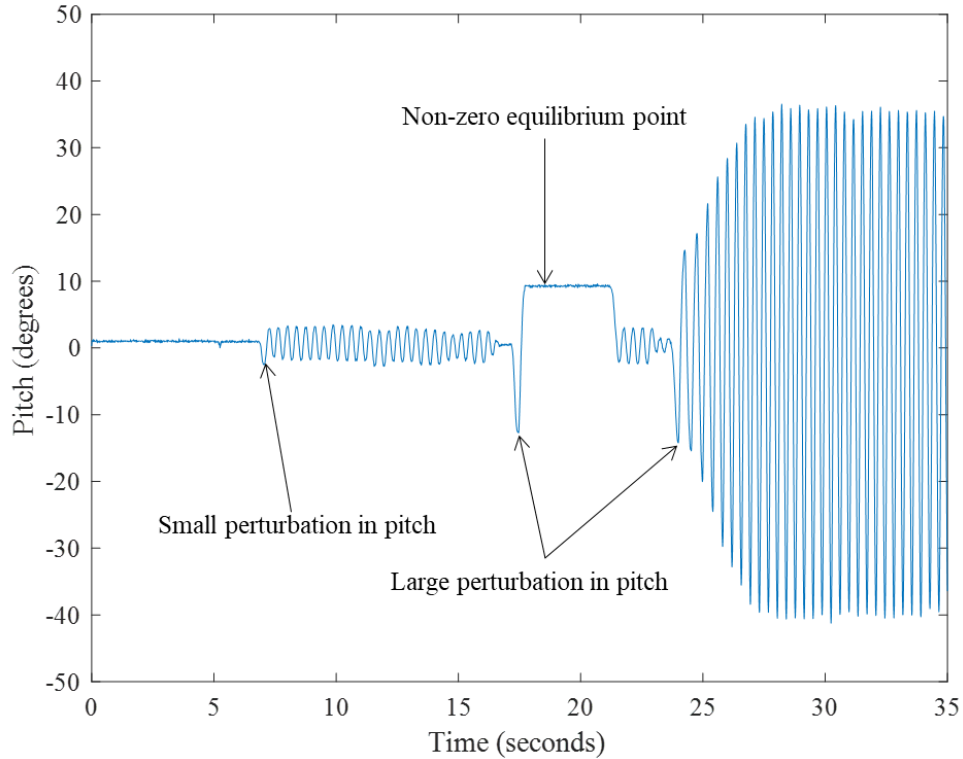
*Figure 4.2: Time history plot of multiple aeroelastic phenomena, $U_\infty$ = 8 m/s ($Re_c$ = 8.3x10⁴)*

## 4.2 One-Degree-of-Freedom Limit Cycle Oscillations

### 4.2.1 1DOF Limit Cycle Oscillation Response

For experiments conducted at 0.35c, it is concluded that the sustained 1DOF LCOs are due to stall flutter. This is based on two arguments. First, the LCOs needed only one DOF, which discards the possibility of coupled flutter. Second, no coupled flutter is predicted from the analytical results of a linear aeroelastic model with unsteady aerodynamics, for the configurations tested in this study.

Results from a stall flutter induced LCO for different pitch spring stiffness at this elastic axis location are presented below. A typical time-history response is included in Figure 4.3. Two time-history plots of the oscillation at 8.44 m/s, for a 1DOF LCO response with a pitch stiffness of 0.3 Nm/rad, over 30 seconds and 3 seconds are presented. The error was estimated to the ±2.4 degrees, and the standard deviation to be 0.6 degrees. The raw data was filtered with a cut-off frequency of 30 Hz. Well-behaved SHM of constant amplitude about a near-zero AoA can be observed. A slight bias of about -5° in the pitch exists. The value is above the calculated error in pitch, however it is not considered significant since it is much smaller than the LCO amplitude.
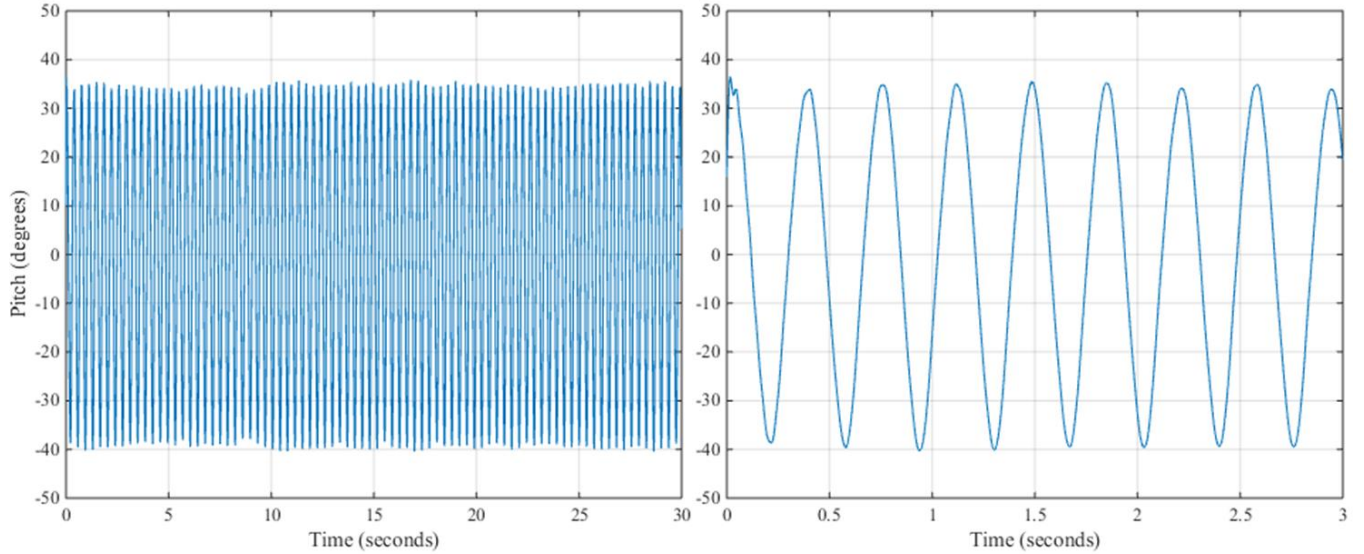
*Figure 4.3: Time history plots of stall flutter induced LCO, $U_\infty$ = 8.44 m/s ($Re_c$ = 8.8x10$^4$), $K_\theta$ =0.3 Nm/rad*

The power spectral density of this oscillatory response can be observed in Figure 4.4, where the dominant peak *f* represents the oscillation frequency. The first $2^{17}$ points were used to perform the FFT algorithm, which gave a frequency resolution of 0.0076 Hz. Relatively strong 2*f* and 3*f* peaks are also observed, however they are a full two decades lower than the dominant peak. Subsequent super-harmonic peaks are much less prominent. The more prominent even super-harmonics indicate an asymmetry in the response, while prominent odd super-harmonics reveal non-linearities. The histogram of the pitch data, shown in Figure 4.5, indicates a clean, symmetrical and SHM-like response. All pitch springs tested exhibited similar well-behaved 1DOF responses in the histograms over all airspeeds. No asymmetric oscillations occurred within the airspeeds tested, unlike the observations by Dimitriadis and Li in 2009 [24].
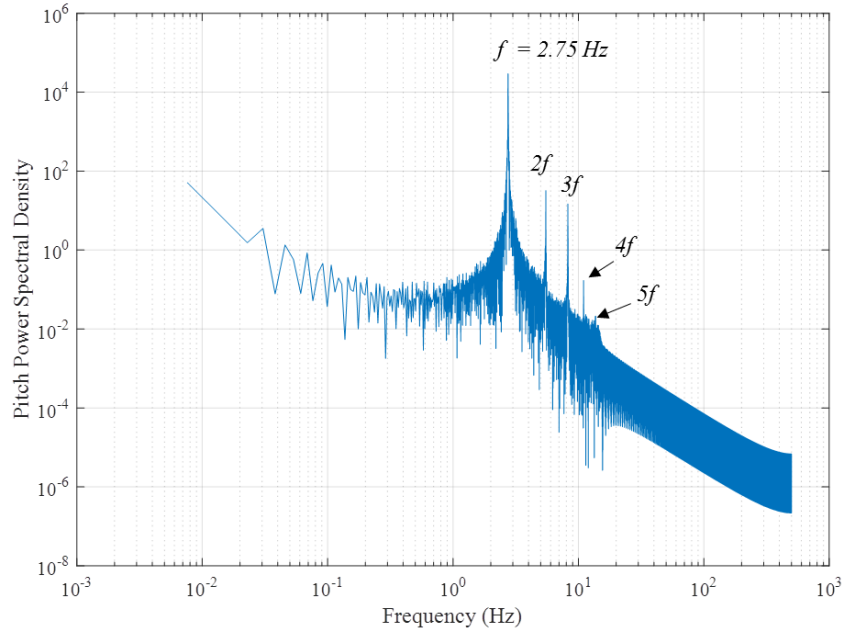
*Figure 4.4: Spectral density of stall flutter induced LCO, $U_\infty$ = 8.44 m/s ($Re_c$ = 8.8x10$^4$), $K_\theta$ =0.3 Nm/rad*



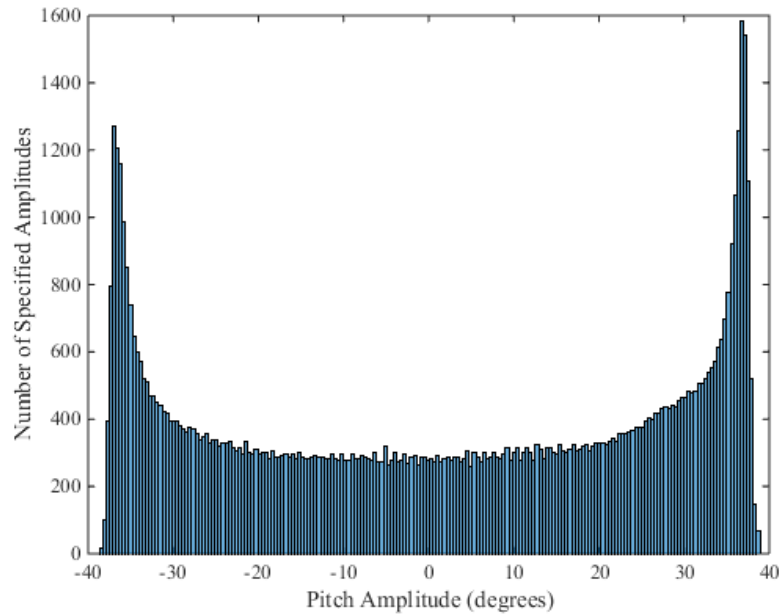*Figure 4.5: Histogram of LCO pitch data, $U_\infty$ = 8.44 m/s ($Re_c$ = 8.8x10$^4$), $K_\theta$ =0.3 Nm/rad*

## 4.2.2 Sensitivity to Reynolds Number and Stiffness

The 1DOF stall flutter LCO behaviour for increasing Reynolds number was investigated for a range of pitch stiffness. A table of each pitch spring stiffness tested, with the corresponding analytical divergence speed is shown in Table 4.1. The analytical divergence speed for each spring tested fell below or within the range of airspeeds tested. The pitch amplitude and frequency values, for various pitch spring stiffness, obtained from experiment are plotted as a function of Reynolds number, in Figures 4.6 and 4.7, respectively.

The pitch amplitude was determined from the peaks of the position data histograms. The frequency of oscillation was obtained from the dominant peak of the corresponding PSD. The airspeeds at which oscillations start to occur is seen to decrease with decreasing pitch stiffness. Similar to the findings of Dimitriadis and Li and Peristy et al., the LCO amplitude values for all cases are seen to increase until a constant value [17, 24]. The amplitude values reach a value close to 45°. Similar to the trend observed for coupled flutter, the LCO frequency values increase for all stiffness values. With increasing stiffness comes an increase in the oscillation frequency. Unlike the observations seen in Chapter 3 however, the trends appear linear and do not tend towards a certain value.

| $K_\theta$ (Nm/rad) | $U_{div}$ (m/s) |
|---|---|
| 0.15 | 5.18 |
| 0.2 | 6.00 |
| 0.3 | 7.32 |
| 0.35 | 7.91 |

*Table 4.1: List of pitch spring stiffness used for 1DOF Stall Flutter experiments.*

In order to highlight the non-linearity of the total system, the analytical linear static frequencies ( $f_{aero}$ ) are calculated using Equations 4.1 and 4.2, derived from the characteristic equation for the total aeroelastic system. The calculated values are presented in Figure 4.8. Since the elastic axis is aft of the aerodynamic centre, the theoretical static linear frequency is imaginary past the divergence speed. While the static term predicts decreasing and imaginary values for frequency, the increasing experimental values indicate a strong presence of non-linear behaviour in the aerodynamics. The trend for the reduced frequency is also linear, however are decreasing, as seen in Figure 4.9. This trend is similar to that observed in coupled flutter, where values are well above 0.05, indicating a high level of aerodynamic unsteadiness in the LCO response. Similar to the LCO frequency, higher pitch stiffness values correspond to increased reduced frequency at the same airspeed.

$$\omega_{aero} = \sqrt{\frac{K_\theta - e\rho U_\infty^2 bl2\pi}{I_{EA}}} \qquad [4.1]$$

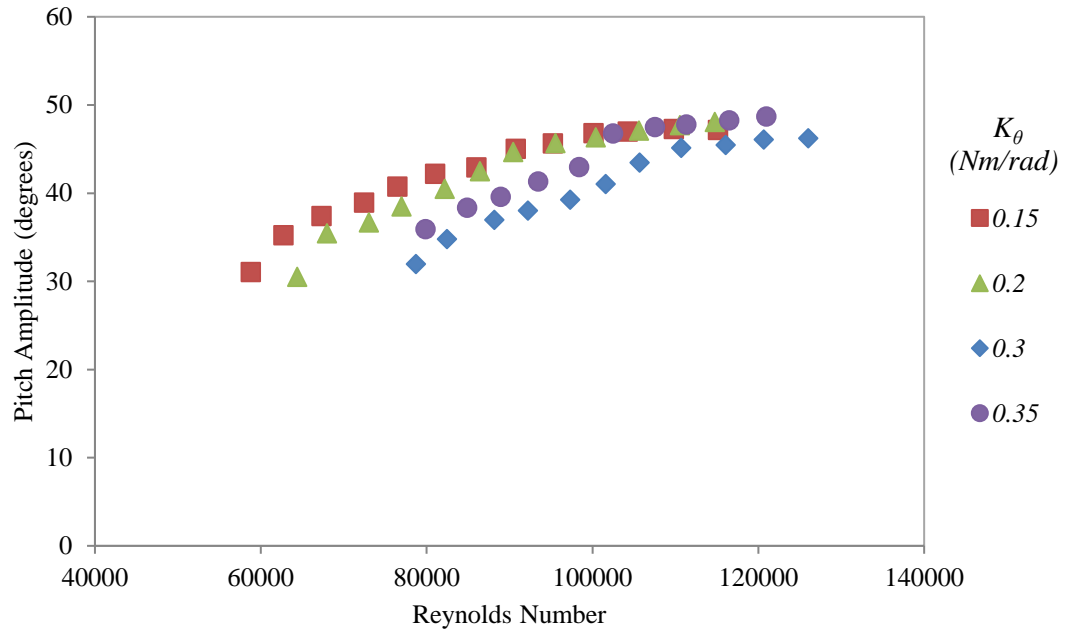$$f_{aero} = \frac{\omega_{aero}}{2\pi} \qquad [4.2]$$

*Figure 4.6: Experimental stall flutter LCO amplitude values with Reynolds Number, for different pitch stiffness.*
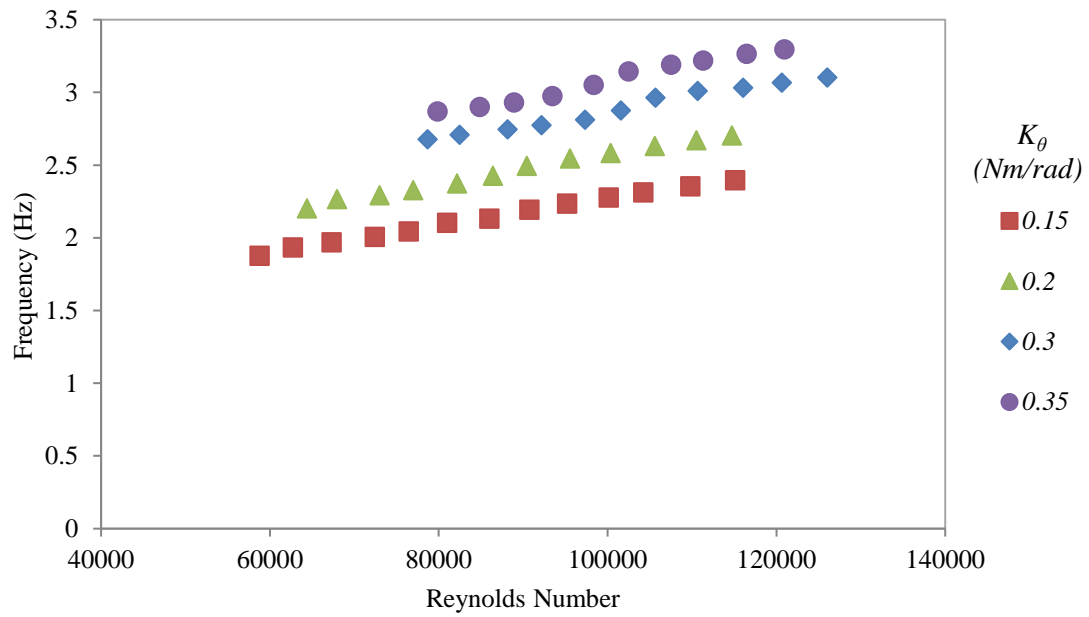


*Figure 4.7: Experimental stall flutter LCO frequency values with Reynolds Number, for different pitch stiffness.*
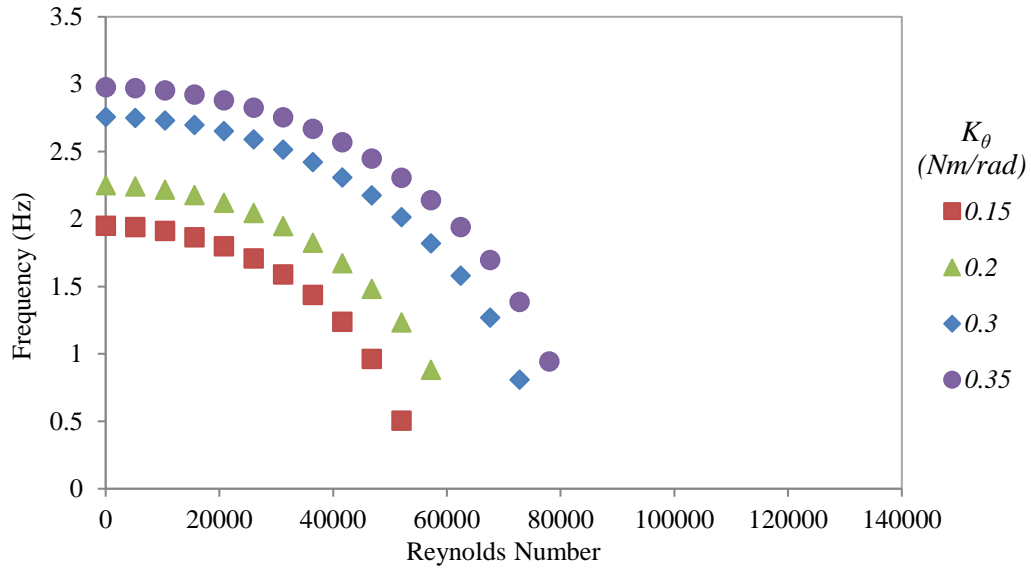
*Figure 4.8: Analytical static linear frequency values with Reynolds Number, for different pitch stiffness*
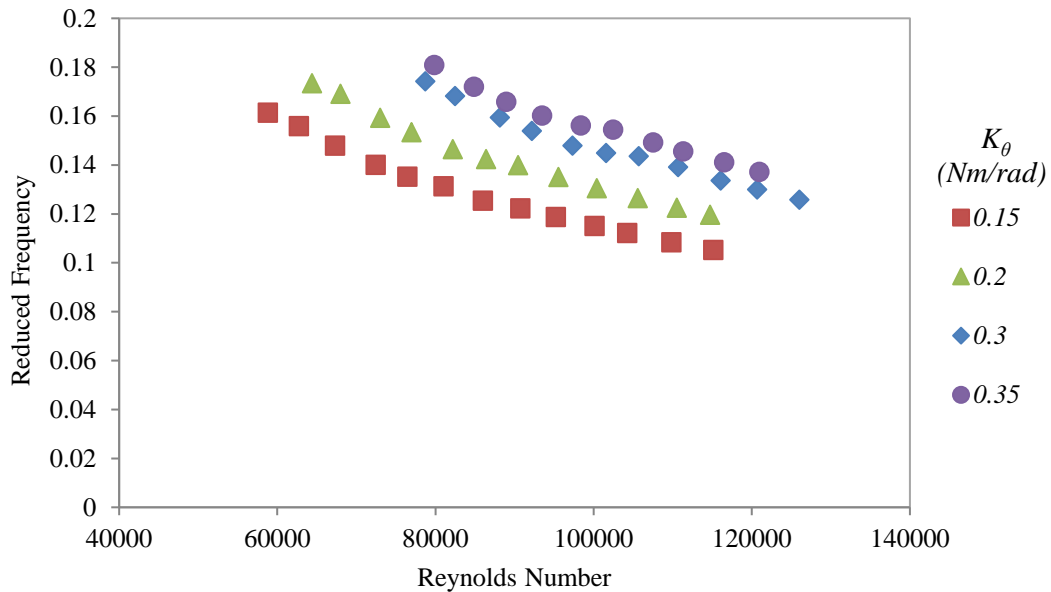


*Figure 4.9: Experimental reduced frequency values with Reynolds Number, for different pitch stiffness*

## 4.2.3 Effect of Boundary Layer and Airfoil Roughness

Adding surface roughness to the leading-edge of an airfoil causes earlier boundary-layer transition into turbulence, thereby reducing the presence of laminar flow within the transitional Reynolds number regime [37]. The importance of low Reynolds effects on the 1DOF stall flutter response was investigated by comparing the results taken with a clean airfoil versus one with

sandpaper attached along its leading-edge. For this case, the width of application is 9 cm, and the sandpaper is 80 grit P-grade. The pitch stiffness was kept at 0.3 Nm/rad for both tests. It is important to note that only 5 seconds of data was recorded of the LCO response with the tripped boundary layer, compared to 80 seconds for the clean–airfoil case.

Unlike the 1DOF case investigated with a clean airfoil, the case with the sandpaper did not produce any SAOs. The oscillation amplitude and frequency of the large amplitude LCO response were calculated using the same methods described in section 4.2.2. Results for both cases are plotted in Figures 4.10 and 4.11. As can be observed, there is little difference between the behaviour from a clean airfoil and a tripped boundary layer. Both cases are initiated at almost the same airspeed. The natural frequency of the airfoil with the tripped boundary layer was calculated to be about 17.2 rad/s, slightly lower than the clean airfoil case which was determined to be about 17.6 rad/s. Slightly higher amplitudes and lower frequencies occur for LCOs with sandpaper on the leading-edge. It can therefore be inferred that low-Reynolds number effects do not have a significant effect on the behaviour of stall flutter induced LCOs. This result had been suggested by McCroskey [23] from the point of view of dynamic stall.
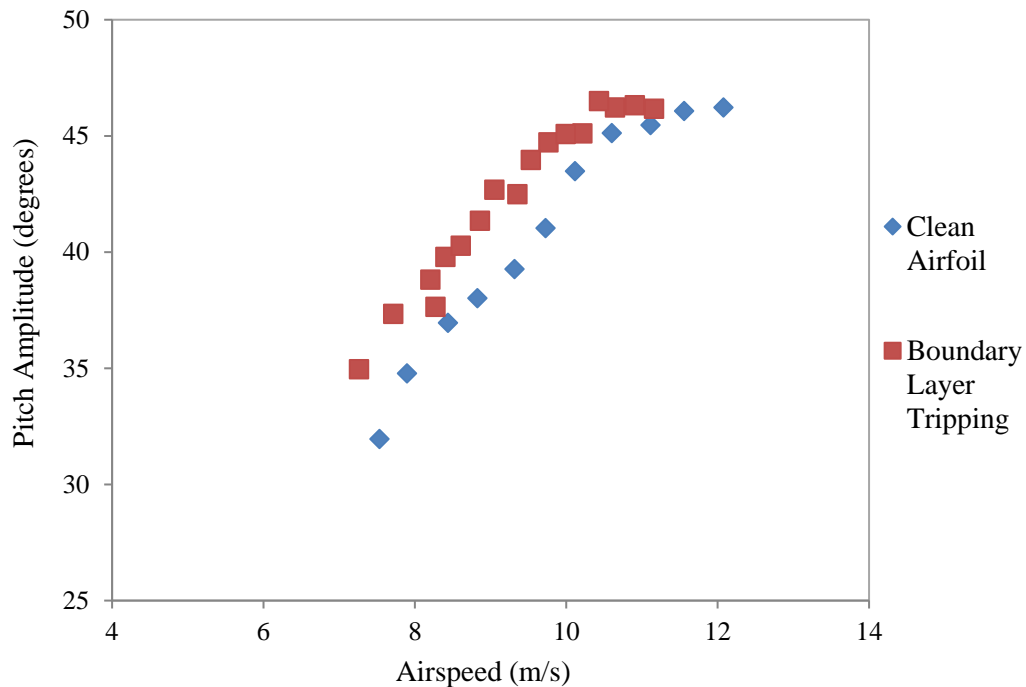


*Figure 4.10: 1DOF stall flutter LCO amplitude values for different leading-edge roughness.*
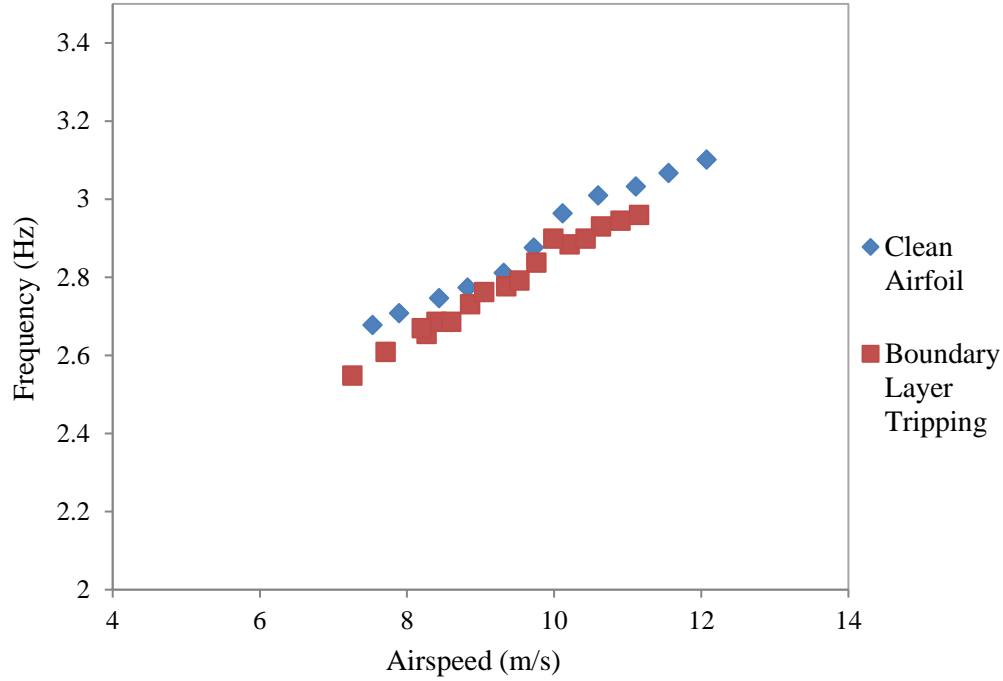
*Figure 4.11: 1DOF stall flutter LCO frequency values for different leading-edge surface roughness.*

## 4.2.4 Aerodynamic Load Analysis

The experimental phase-averaged stall flutter LCO moment coefficients at 8.44 m/s and 12 m/s for the nominal clean airfoil case (0.3 Nm/rad) were calculated using the equation of motion for the 1DOF case, shown below in Equation 4.3. The same five-point differentiation scheme used in Chapter 3 is re-used for this analysis. The calculated aerodynamic moment was phase-averaged for at least 60 cycles. The data was filtered with a cut-off frequency just above the 5*f* super-harmonic. The behaviour of the calculated moment did not change significantly if higher frequency content was included. However, the higher the filtering cut-off frequency, the more high-frequency content introduced noise into the aerodynamic moment response. The plotted analytical static linear moment, as well as the analytical unsteady response from Theodorsen's equations is included with the experimental values.

$$I_{EA}\ddot{\theta} + D_\theta \dot{\theta} + K_\theta \theta = M_{EA} \tag{4.3}$$

Whereas the analytical unsteady moment predicts negative work for the entire cycle, the total cycle averaged experimental work is positive, as indicated in the plots. Stable and unstable regions in the experimental LCO cycle can be observed in Figures 4.12 and 4.13. A stable counter-clockwise loop exists between two clockwise unstable hysteresis loops in the stall region. The non-elliptical hysteresis in the response confirms the inherently non-linear response of stall flutter induced LCOs. At 12 m/s, the stable region in the centre is reduced in its range of

pitch, and more complex behaviour can be seen with the addition of stable regions in the extremities of the loops. The stable region of the moment of the 12 m/s case is also close to the slope of the analytical static linear moment. This behaviour does not occur for the moment at an airspeed of 8.44 m/s.
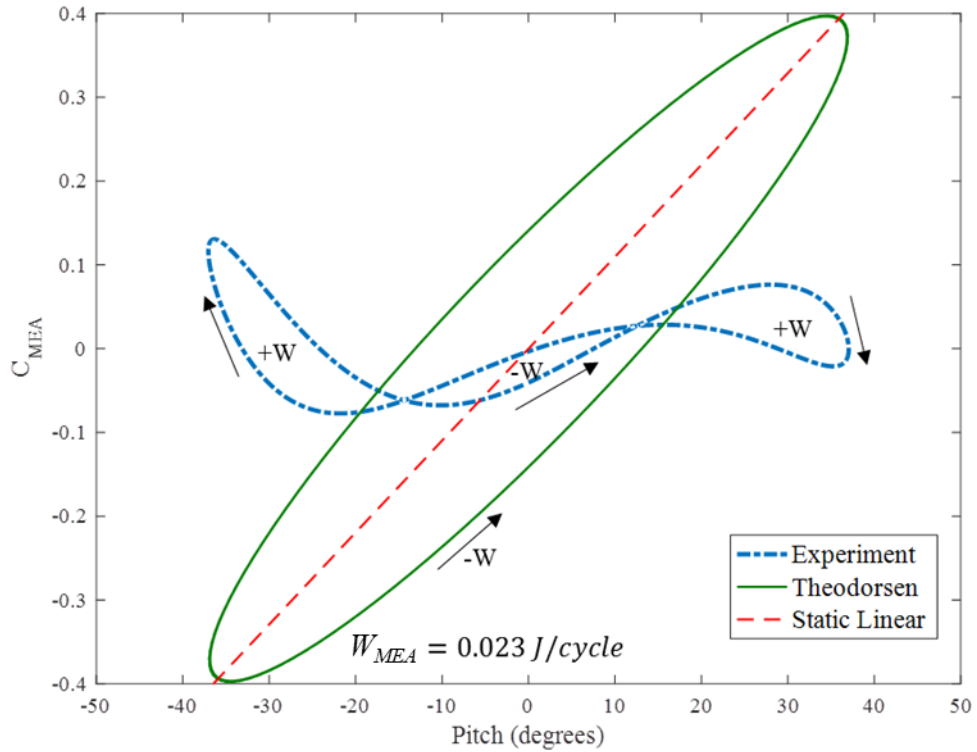


*Figure 4.12: Aerodynamic moment coefficient with pitch position, $U_\infty = 8.44$ m/s ($Re_c = 8.8x10^4$).*
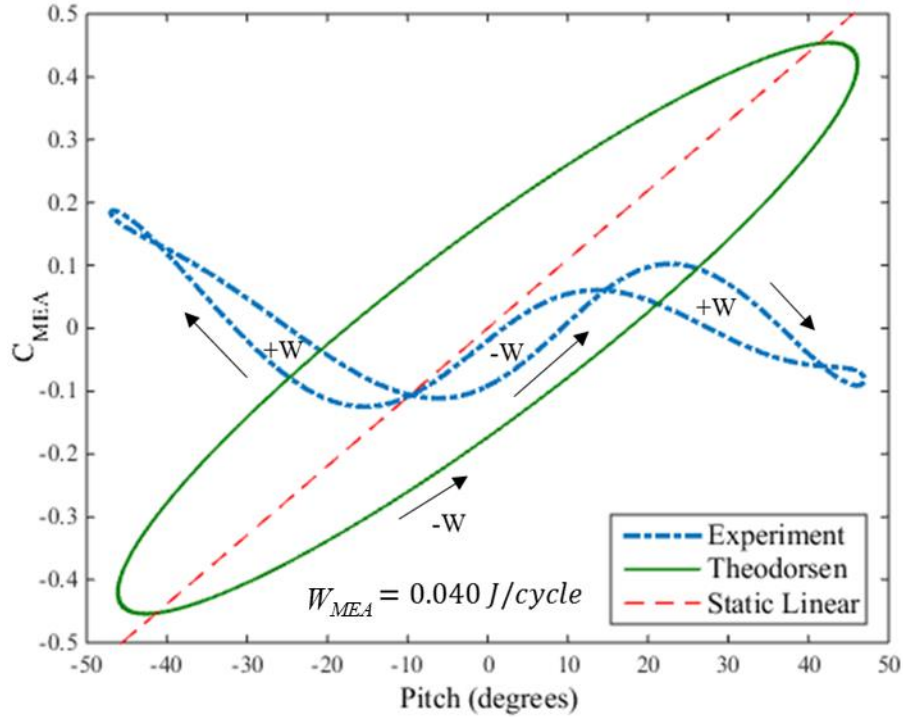
*Figure 4.13: Aerodynamic moment coefficient with pitch position, $U_\infty = 12$ m/s ($Re_c = 1.3x10^5$).*

## 4.3 Experimental Results for Two-Degree-of-Freedom Limit Cycle Oscillations

Sets of experiments were conducted where the heave degree of freedom was also free to oscillate. The sensitivity of the 2DOF LCO response to increasing Reynolds number was investigated, along with the effect of varying the frequency ratio from below to above one, $0.68 \leq \bar{\omega} \leq 1.43$. The pitch stiffness was kept at 0.3 Nm/rad for all tests. The experiments were performed for the range of airspeeds where 1DOF stall flutter was observed to occur. The Reynolds number was increased until the oscillation amplitude and frequency were deemed to approach the limits of the experimental set-up. The error in the oscillation amplitudes was calculated for responses resembling SHM only. The error and standard deviation in pitch for 2DOF responses was found to match that for 1DOF. The error and standard deviation in heave was calculated to be ±0.51 cm and 0.085 cm respectively. The offset in the heave oscillations was determined to be -0.63 cm.

### 4.3.1 2DOF Limit Cycle Oscillation Response

The behaviour of the oscillations for frequency ratios 0.68, 1.43, and 0.92 can be observed in the time histories, for the same Reynolds numbers, in Figures 4.14, 4.17, and 4.19 respectively. Also included are the PSDs of the two motions for these frequency ratios. As observed in the 1DOF case, 2DOF LCOs occur about a near-zero AoA. Plotting the oscillations for 2.5 seconds, one can observe SHM behaviour and phase difference for frequency ratios 0.68 and 1.43. Oscillations across most frequency ratios are well-behaved SHM, apart from a frequency ratio close to one, as will be discussed more in section 4.3.4. The pitch and heave motions are out of phase by about 150° (pitch leading) in Figure 4.14, while the motions are almost in phase in Figure 4.19. Similar to the observations for coupled flutter, one can observe more pronounced high frequency content in heave, for frequency ratios 0.68 and 1.43. Like the 1DOF case however, strong $2f$ and $3f$ peaks are observed for the pitch PSD. Super-harmonic peaks beyond $3f$ are much less prominent.

Plotting data over 30 seconds, one can observe periodic modulations which occur in the response for a frequency ratio of 0.92. These modulations are a beating phenomenon: an interference pattern resulting from the interaction of two very close fundamental frequencies. Similar behaviour was observed at a frequency ratio of 0.96. The presence of two frequencies is apparent when plotting the PSD of the oscillation in Figure 4.16. Two peaks, both heave and pitch dominated frequencies, are present. The corresponding natural frequency in pitch is 2.8 Hz, while the natural frequency in heave is 2.5 Hz. The peak associated with beat frequency ($f_{beat}$), the difference between the interacting frequencies, also appears in the PSD. This phenomenon is discussed in more detail in section 4.3.4, in terms of lock-in.

*Figure 4.14: Time history plot (top), frequency content for pitch response (bottom left), and frequency content for heave response (bottom right of 2DOF stall flutter, for $\bar{\omega}$ = 0.68 and $U_\infty$ = 8.47 m/s ($Re_c$ = 8.8x10⁴).*

*Figure 4.15: Pitch (top) and heave motion (bottom), for $\bar{\bar{\omega}} = 0.92$ and $U_\infty = 8.47$ m/s ($Re_c = 8.8x10^4$).*



*Figure 4.16: Spectral density of stall flutter induced LC, in pitch (left) and heave (right), at $\bar{\bar{\omega}} = 0.92$ and $U_\infty =$ of 8.47 m/s ($Re_c = 8.8x10^4$).*
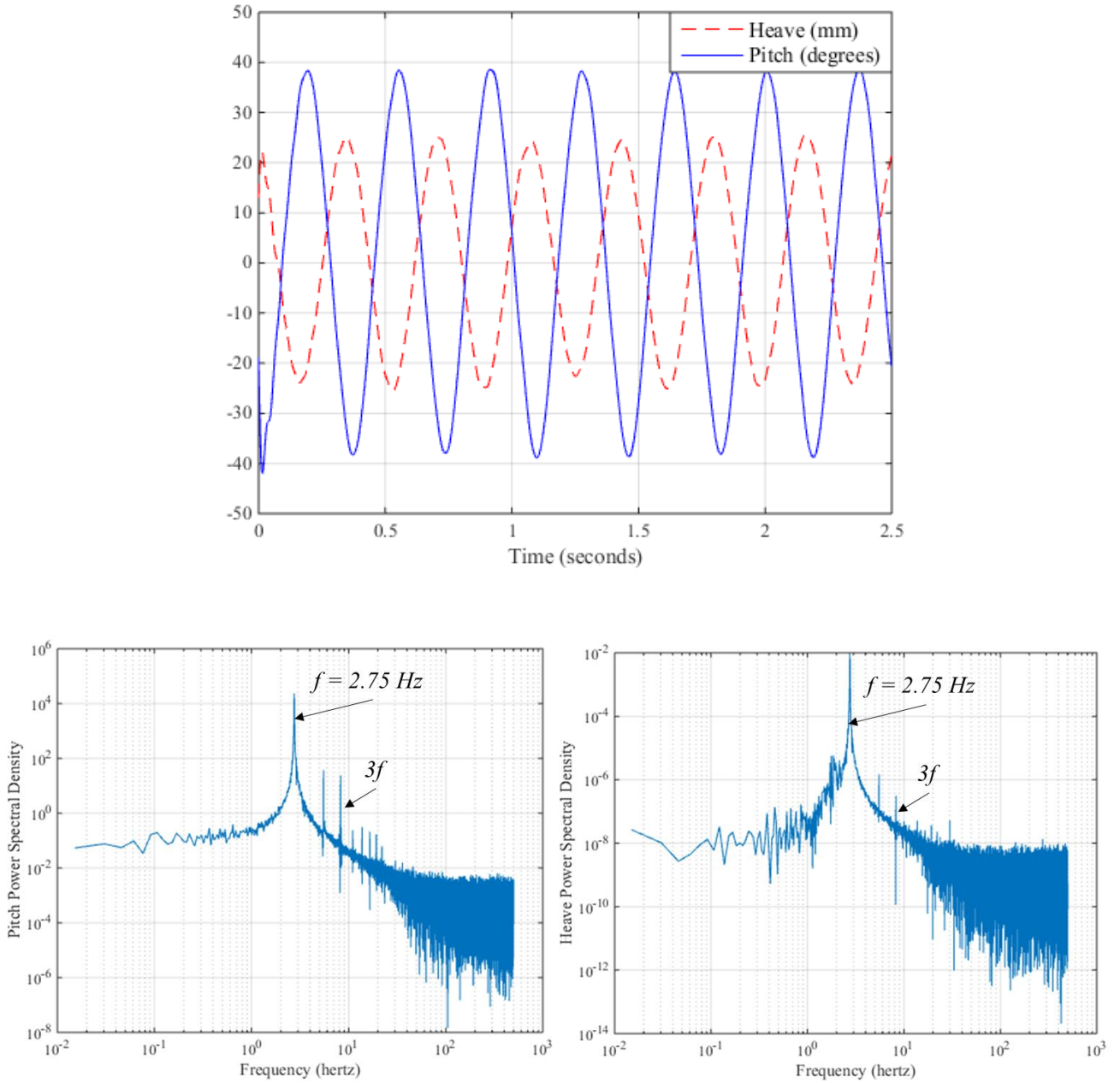
*Figure 4.17: Time history plot (top), frequency content for pitch response (bottom left), and frequency content for heave response (bottom right of 2DOF stall flutter, for $\bar{\omega}$ = 1.43 and $U_\infty$ = 8.39 m/s $(Re_c = 8.7x10^4)$.*
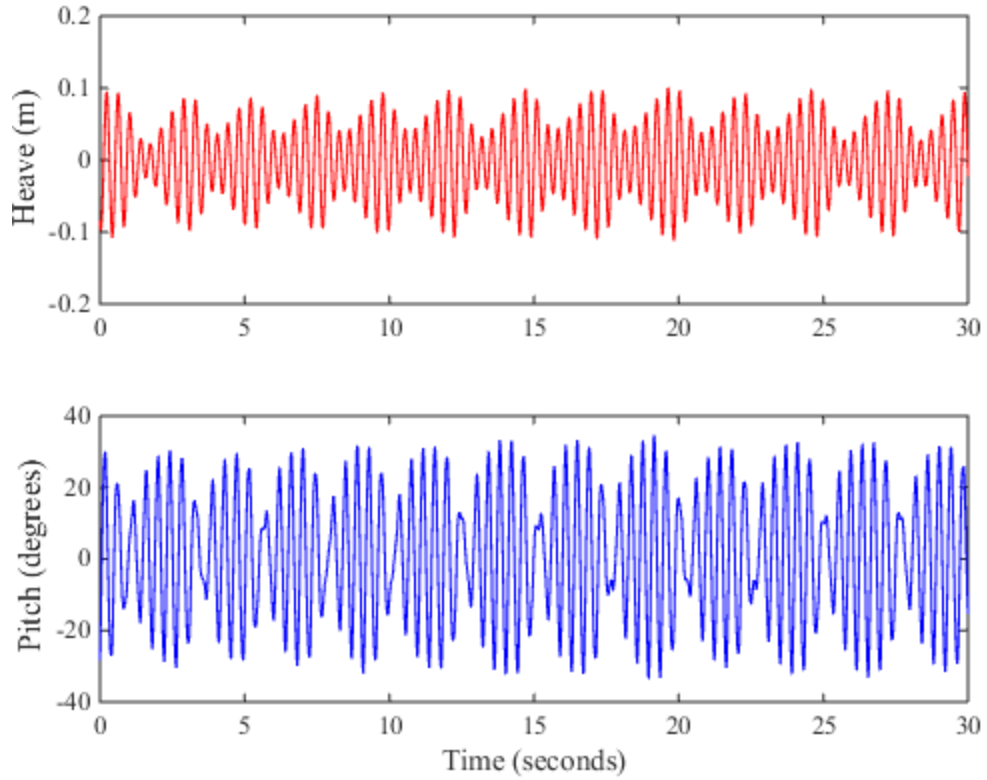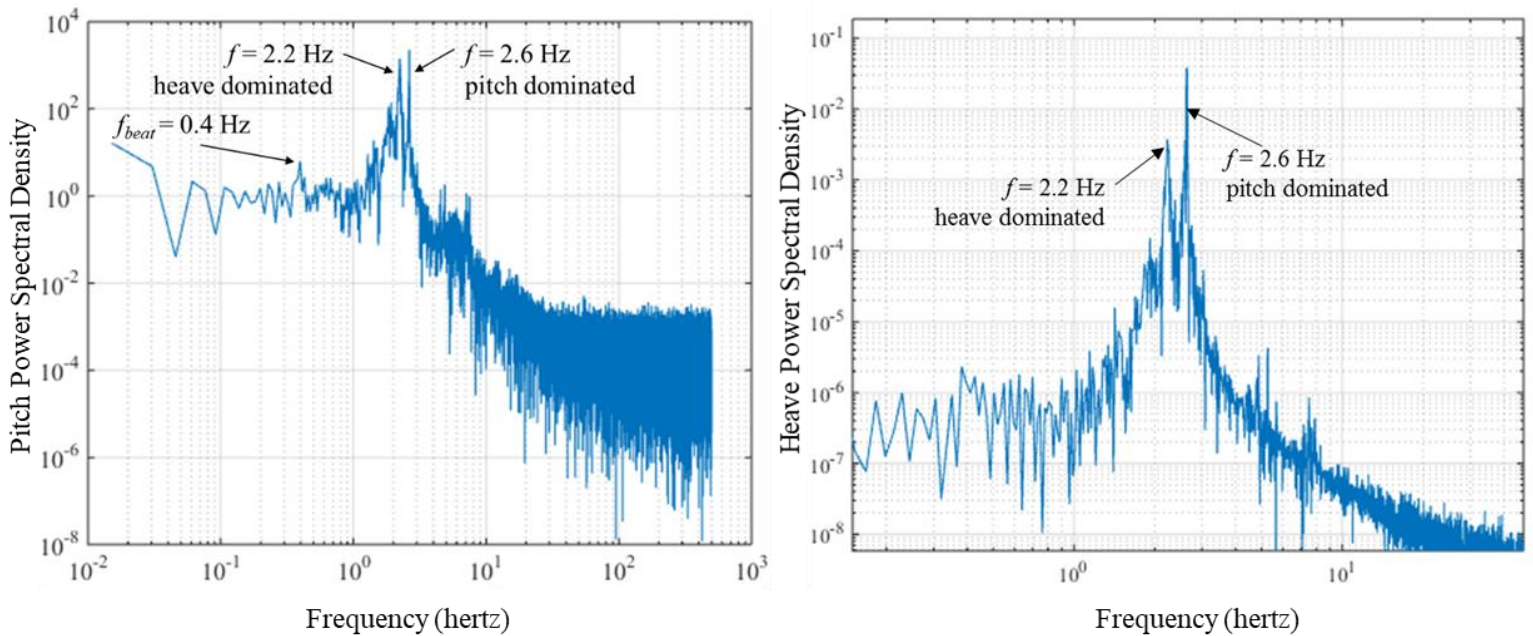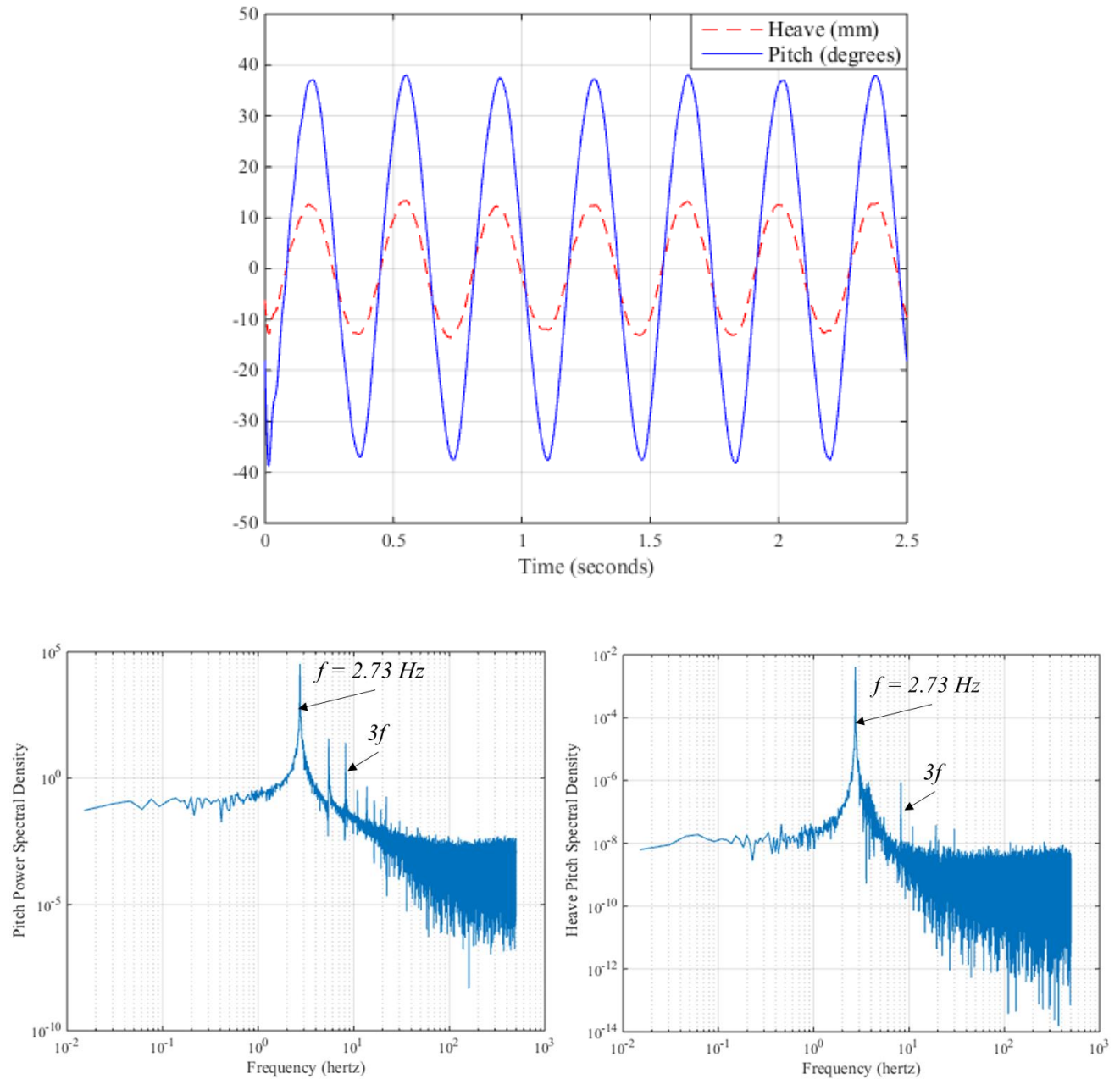
## 4.3.2 Sensitivity to Reynolds Number

The sensitivity to Reynolds number of stall flutter induced LCOs, free in heave and pitch, was investigated. The same methods of analysis used in Chapter 3 for coupled flutter are re-used in this section. The pitch amplitude of each 2DOF LCO response is plotted with Reynolds number. The values were determined from the histograms of SHM responses at differing frequency ratios. The phase was determined by finding the average difference between the pitch and heave peaks, with pitch leading as defined in Equations 1.44 and 1.45. It can be seen in Figure 4.18 that the inclusion of heave motion does not considerably affect the pitch amplitude response. The LCO frequency, determined from the FFT analysis used previously, is also plotted as a function of Reynolds number in Figure 4.19; its dependence on Reynolds number is also minimal. The behaviour of the frequency with increasing Reynolds number is also similar to the 1DOF case. In this analysis, 1DOF corresponds to a frequency ratio of infinity, where the heave motions are completely constrained. Unlike the coupled flutter case where the pitch and frequency tend towards a constant value across frequency ratios, all values for stall flutter induced LCO increase with Reynolds number as they closely follow the 1DOF case. Similar to the coupled flutter case, are the decreasing values for reduced frequency all close in value over Reynolds number. The reduced frequency values for stall flutter induced LCO, however, follow a much more linear trend than the exponential behaviour seen in coupled flutter induced LCOs.

The root-mean-square (RMS) of the heave oscillations was determined, since the responses of frequency ratios close to one experience varying degrees of modulation. These cases were not included in the plots for pitch amplitude and oscillation frequency with Reynolds number. All values for heave RMS increase with Reynolds number. For frequency ratios close to one, the heave amplitude increases sharply with increasing Reynolds number, as can be observed in Figure 4.21. The amplitudes themselves are large in value, approaching the physical limitations of the experimental rig. This sharp increase in the amplitude values around a frequency ratio of one resembles a resonance-like behaviour, and will be further analyzed in section 4.3.4. On the other hand, the response in heave appears to settle on relatively small amplitudes for frequency ratios away from one. The phase angle between the pitch and heave oscillations at each frequency ratio was found to vary insignificantly with increasing Reynolds number. However, as observed in Figure 4.22, the phase difference is close to about 150° below a frequency ratio of one, becoming in-phase above a frequency ratio of one.
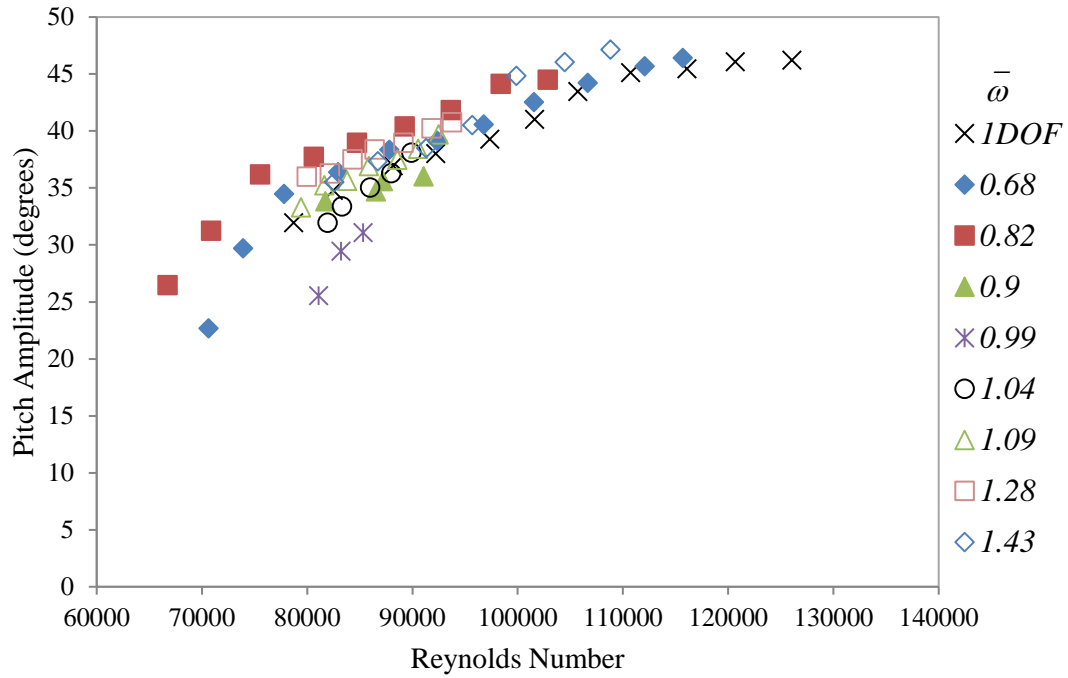
*Figure 4.18: Pitch amplitude for each frequency ratio over increasing Reynolds numbers.*
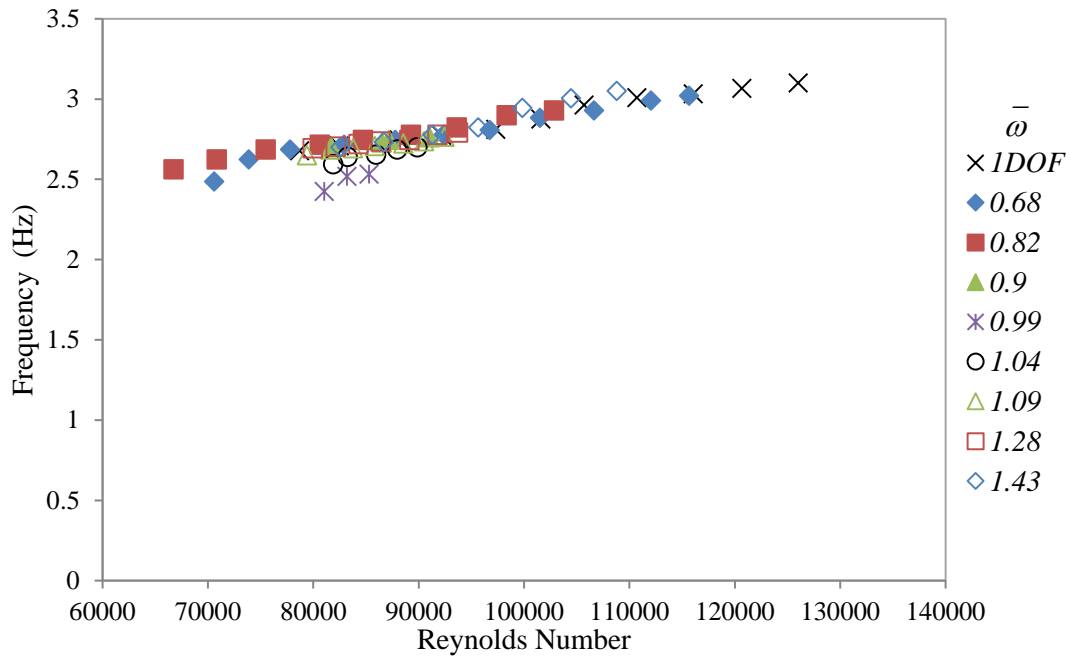


*Figure 4.19: LCO frequency for each frequency ratio over increasing Reynolds numbers.*
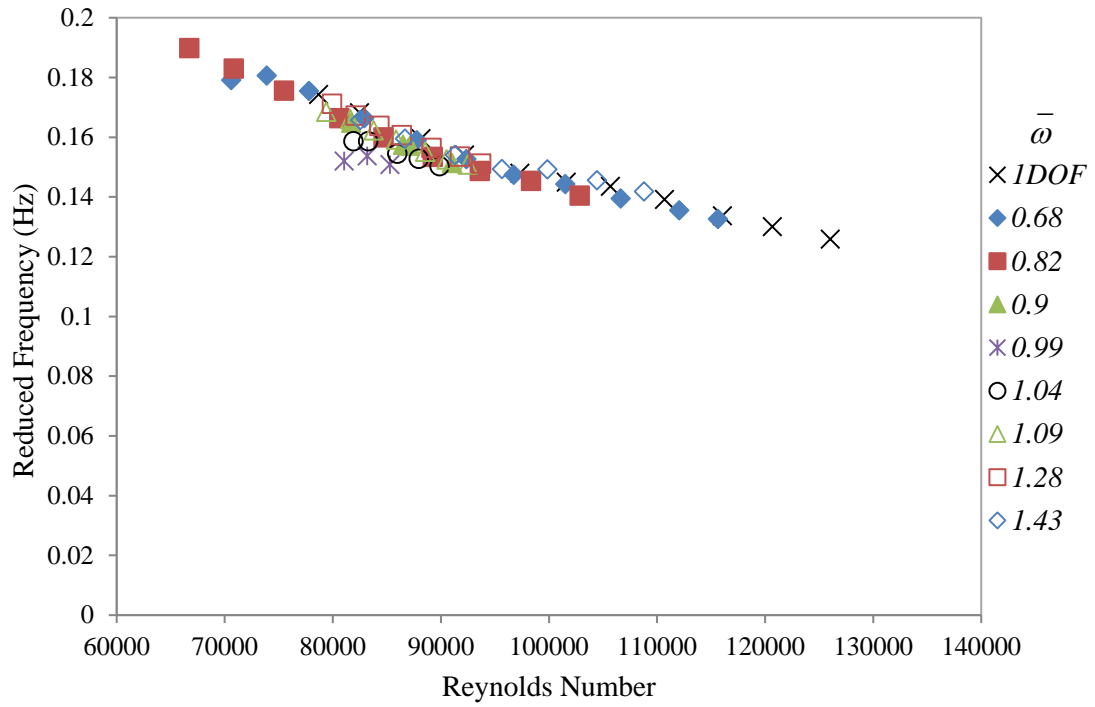
*Figure 4.20: Reduced frequency for each frequency ratio over increasing Reynolds numbers.*
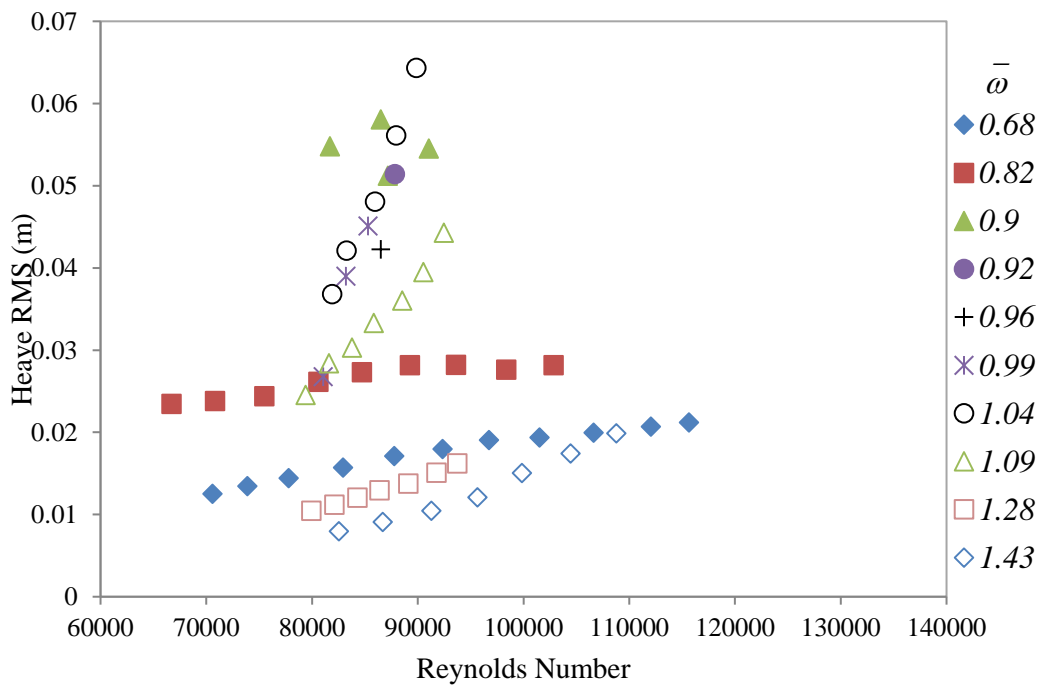


*Figure 4.21: Heave RMS for each frequency ratio over increasing Reynolds numbers.*
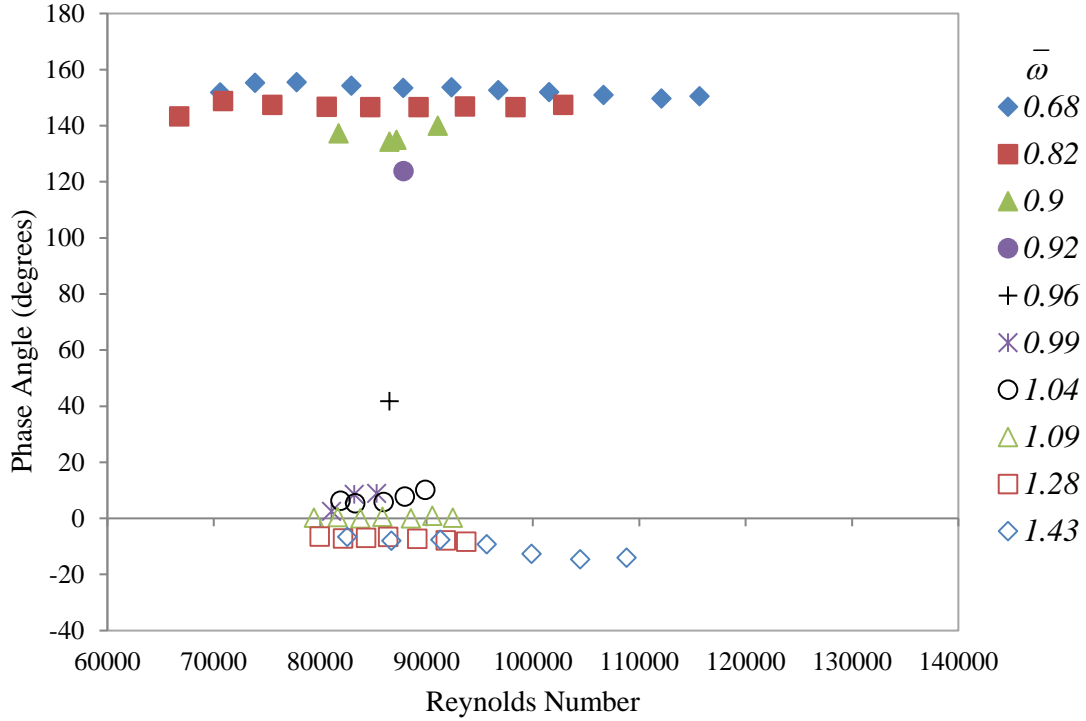
*Figure 4.22: Phase angle between pitch and heave oscillations over Reynolds Number*

## 4.3.3 Aerodynamic Load Analysis

The phase-averaged aerodynamic moment and lift coefficients are calculated for frequency ratios 0.68 and 1.43 based on Equations 1.2 and 1.3 (re-stated below), for Reynolds numbers close to the 1DOF analysis. The analysis did not include results for frequency ratios close to one, because the high degree of modulation in the oscillations at these configurations did not produce discernable results. The same filtering conditions, differentiation scheme and number of phase-averaged cycles used in the 1DOF case, are used for 2DOF. As in previous analysis, the analytical static and unsteady results from Theodorsen's are included for comparison. Plots of the numerical results are included in Figures 4.23 to 4.24.

$$M_h \ddot{h} - \frac{M_\theta c x_\theta}{2} \ddot{\theta} + D_h \dot{h} + K_h h \ = \ L \qquad [1.2]$$

$$I_{EA} \ddot{\theta} - \frac{M_\theta c x_\theta}{2} \ddot{h} + D_\theta \dot{\theta} + K_\theta \theta = M_{EA} \qquad [1.3]$$

The aerodynamic moment curves for the response of both frequency ratios are similar in shape to the 1DOF (see Figure 4.12), and to each other (Figures 4.23A and 4.24A). As observed in the 1DOF case, using Theodorsen's equations predicts negative work throughout the cycle. The total experimental work done by the moment in 2DOF was calculated to be positive however, where the values for 0.68 and 1.43 frequency ratios are close in value to the 1DOF

case. This observation suggests that for frequency ratios away from one, the behaviour in pitch for a 2DOF LCO induced by stall flutter is not strongly influenced by the introduction of heave motion. The similarity of the moment curve with the 1DOF case also suggests that the pitch drives the motion in heave. For the 0.68 frequency ratio case, the moment curve is qualitatively similar to the 1DOF experimental curve.

Similar to the results obtained from coupled flutter induced LCOs, the lift curves as a function of heave (Figures 4.23B and Figures 4.24B) follow irregular ellipses influenced by non-linear effects, however not as strongly as the moment curves. This also correlates to the observation that the heave PSDs (Figures 4.14 and 4.17) in both stall and coupled flutter induced LCOs contain reduced odd-superharmonic content compared to the pitch PSDs, thus a lower degree of non-linearity. Also similar to the coupled flutter case, the aerodynamic lift does more work throughout the cycle. For a frequency ratio of 0.63, the experimental and analytical curves in Figure 4.23B both exhibit a clockwise loop, indicating positive work throughout the cycle. For a frequency ratio of 1.43 however, Theodorsen's equations predict a stable counter-clockwise loop, while experiment shows positive work done throughout the cycle in Figure 4.24B. The positive slope of the ellipses for the lift at a frequency ratio of 1.43 indicate the oscillations are close to being in-phase

The behaviour is similar to the curves presented by Dimitriadis and Li for symmetric LCOs where the frequency ratio is well above one [24]. In their study, the hysteresis loops occur in the moment curves, and a 'bow-tie' elliptical shape in the aerodynamic lift. The behaviour is generally similar to the observations in this study. Since the frequency ratio tested in their study is 6.94, and well above one, the behaviour follows 1DOF characteristics and is pitch driven. However, the study by Dimitriadis and Li observed extra regions in the moment curve for one case. The reason for this is still unclear, and may be the subject of future studies [24].

*Figure 4.23A: Aerodynamic moment coefficient for $\bar{\omega} = 0.68$ and $U_\infty = 8.47$ m/s ($Re_c = 8.8x10^4$).*



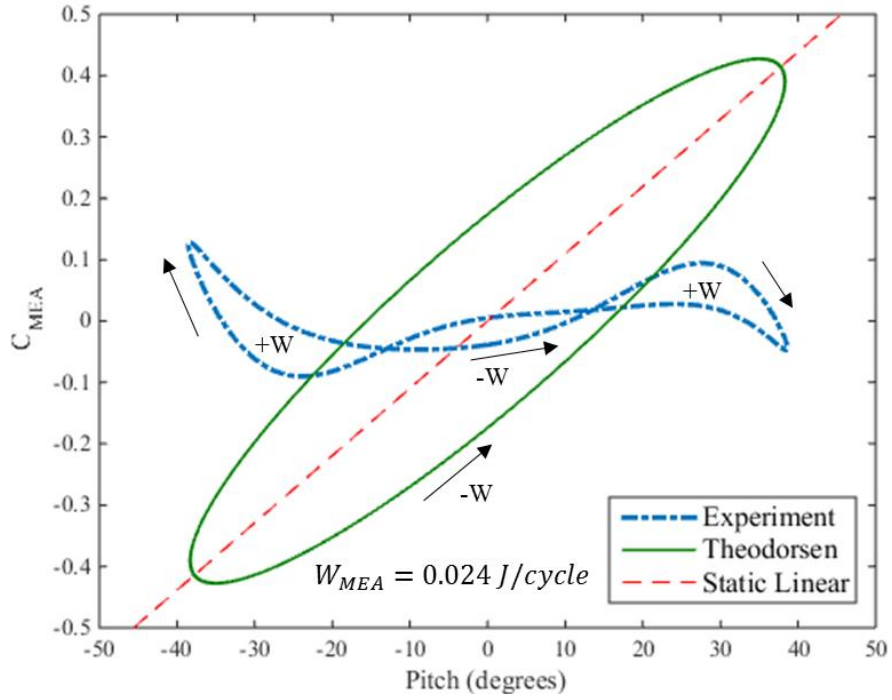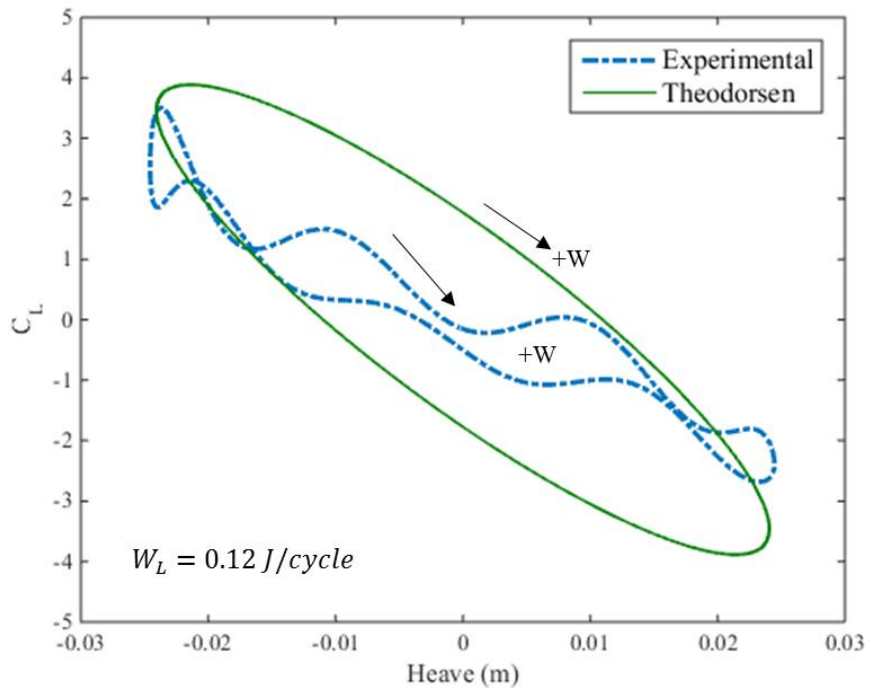*Figure 4.23B: Aerodynamic lift coefficient for $\bar{\omega} = 0.68$ and $U_\infty = 8.47$ m/s ($Re_c = 8.8x10^4$).*
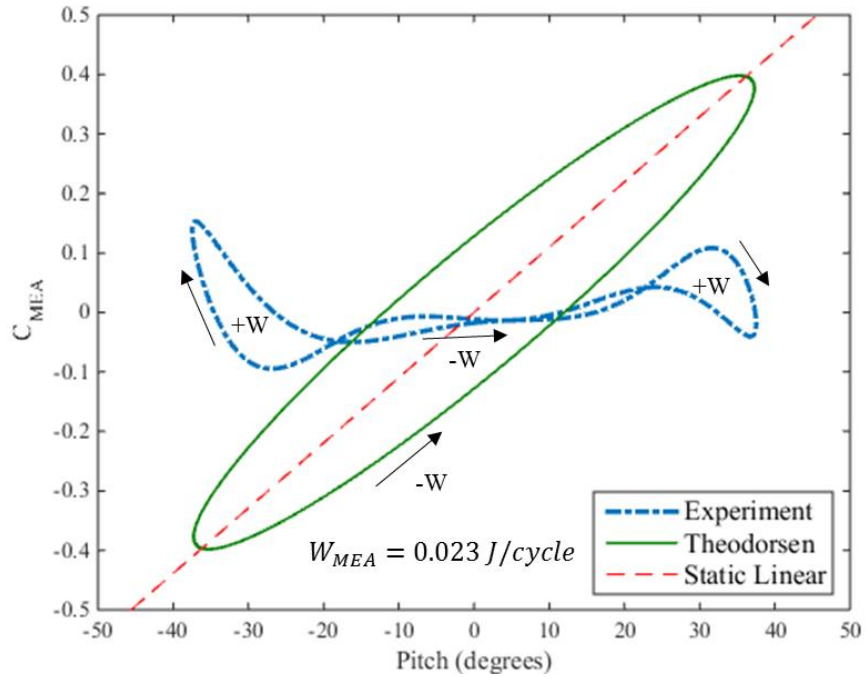
*Figure 4.24A: Aerodynamic moment coefficient for $\overline{\omega} = 1.43$ and $U_\infty = 8.39$ m/s ($Re_c = 8.7x10^4$).*
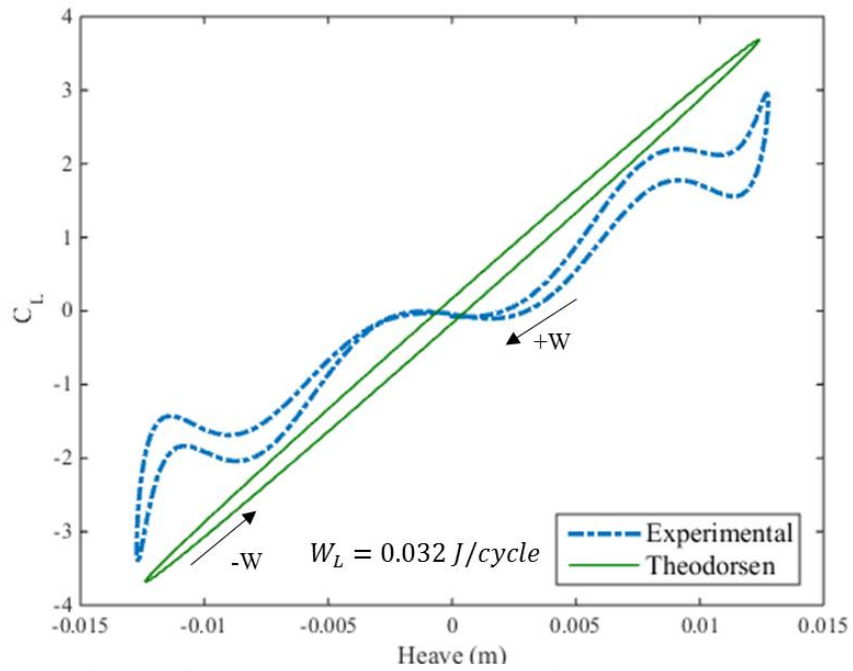


*Figure 4.24B: Aerodynamic lift coefficient for $\overline{\omega} = 1.43$ and $U_\infty = 8.39$ m/s ($Re_c = 8.7x10^4$).*

### 4.3.4 Two Degree-of-Freedom Lock-In

The resonance-like phenomenon in heave, as well as the beating pattern seen in the response for LCOs occurring for frequency ratios close to one is further investigated in this section. In order to explore the sensitivity of the response with frequency ratio, the LCO response for each configuration was investigated over a common Reynolds number. The pitch amplitude, oscillation frequency, heave RMS, as well as phase angle at a Reynolds number of approximately $8.7 \times 10^4$ are plotted across frequency ratios, shown in Figure 4.25.

The resonance effects surrounding a frequency ratio of one in Figure 4.25 can be observed through the difference in behaviour across frequency ratios. Close to a frequency ratio of one, the pitch amplitude and frequency values experience a slight decrease. The heave response reacts more sensitively to changing frequency ratio, where a sharp peak occurs at a frequency ratio of one. As discussed previously in section 4.2.2, the phase angle between the pitch and heave oscillations is approximately 150° below a frequency ratio of one, becoming in-phase above one. The phenomenon indicates a change in dynamics in this region, where the weak feedback coupling between the degrees of freedom may occur. Further analysis was conducted in order to determine whether this coupling is a result of lock-in phenomenon.

Although a resonance is peak is observed in heave, the determining plot for lock-in concerns the frequency, as shown in Figure 1.15 in the Introduction and Background section 1.5.4. The normalized excitation frequency in the x-axis for a cylinder undergoing von Kármán vortex shedding, $U_\infty/f_n D$, can be re-defined in terms of the frequency ratio for a 2DOF airfoil system, as shown below [28].

$$\frac{U_\infty}{f_n D} = \frac{f_s D/St}{f_n D} = \frac{1}{St}\frac{f_s}{f_n} \tag{4.3}$$

where $f_n$ refers to the natural frequency of the structure, and $f_s$ refers to the frequency of the shed vortices into the wake. For a wing free to oscillate in pitch and heave, the natural frequency in heave and shedding frequency correspond to the heave $\omega_h$ and pitch $\omega_\theta$ natural uncoupled frequencies, respectively.

$$\frac{1}{St}\frac{f_s}{f_n} \propto \frac{\omega_s}{\omega_h} \rightarrow \frac{\omega_\theta}{\omega_h} = \frac{1}{\bar{\omega}} \tag{4.4}$$

The plot of the LCO frequency divided by the heave natural uncoupled frequency ($f_h = 1/2\pi\,[K_h/M_h]^{1/2}$) versus the inverse of the frequency ratio is shown in Figure 4.26. This was done for three Reynolds numbers: $8.2 \times 10^4$, $8.7 \times 10^4$, $9.05 \times 10^4$. As can be observed, the characteristic lock-in plateau occurs at frequency ratios close to one. Two important frequencies for the same frequency ratio can be observed in the plateau region. The beating phenomenon in the LCO response at frequency ratios of 0.92 and 0.96 occurs as an interaction between the two frequencies located in the lock-in region.
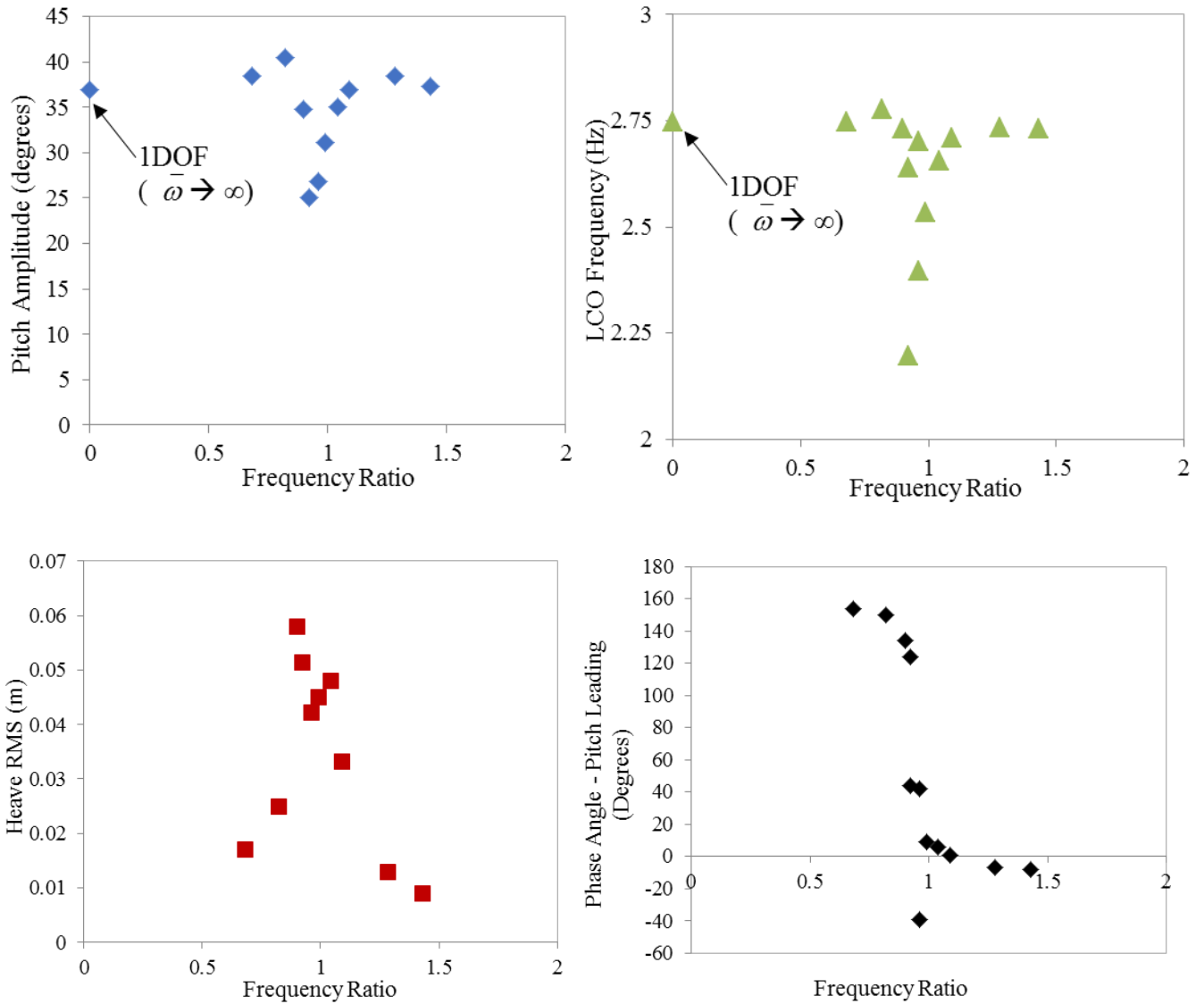
*Figure 4.25: Pitch amplitude (top-left), LCO frequency (top-right), heave RMS (bottom-left), and phase angle (bottom-right) as a function of frequency ratio for $Re_c \sim 8.7 \times 10^4$.*

Therefore, it can be inferred that for a range of frequency ratios close to one, a coupling occurs from the heave to the pitch degree of freedom. This is characterized by a significant increase in the heave amplitude, and a lock-in of the LCO frequency onto the heave dominated frequency. Away from lock-in, the uncoupled pitch motion drives the heave oscillation. This observation is further supported by the fact that the phase angle between the two degrees of freedom changes from a value of $\sim\pi$ to $\sim 0$ with increasing frequency ratio. The tendency of the phase between the 2DOFs to be either approximately 180° or 0° for frequency ratios outside of one, further supports the idea that the pitch drives the heave as a forced system in these regimes. During lock-in, however, the heave motion couples back to the pitch. As discussed in by Poirel et al., this newly discovered phenomenon can be referred to as *2DOF or coupled lock-in*,

84

whereas the classic case of the forced oscillation of a bluff-body interacting with its own wake is classified as *1DOF or forced lock-in* [28].
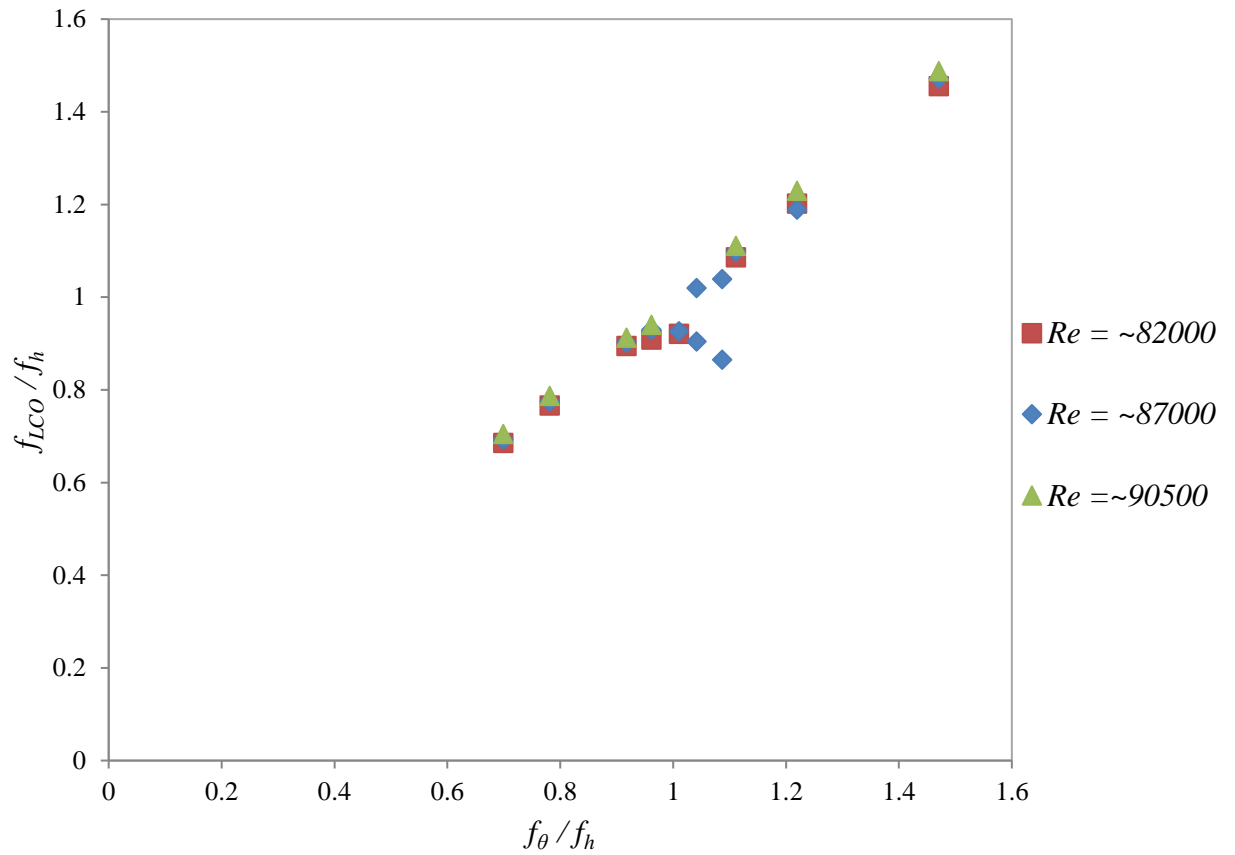


*Figure 4.26: Normalized LCO frequency as a function of the inverse of the frequency ratio for three Reynolds numbers.*

## 4.4 Energy Calculations

As done for coupled flutter induced LCOs, the kinetic energy of the oscillations, as well as the experimental efficiency were calculated for the range of frequency ratios tested. The same process defined in section 1.6, and used in section 3.4, is used again here in order to compare the energy extraction potential of stall flutter induced LCOs. Both the calculated aerodynamic efficiency and kinetic energy are plotted as a function of Reynolds number below. Similar to the response exhibited by coupled flutter induced LCOs, the trend of the kinetic energy observed in Figure 4.27 follows the behaviour of the heave amplitude. Similar observations were made by Poirel and Mendes for SAOs. Even though stall flutter is fundamentally a 1DOF problem, and the overall cycle averaged work and kinetic energy of the 1DOF case is positive, the introduction of the heave degree-of-freedom greatly increases the energy uptake by the structure [13].
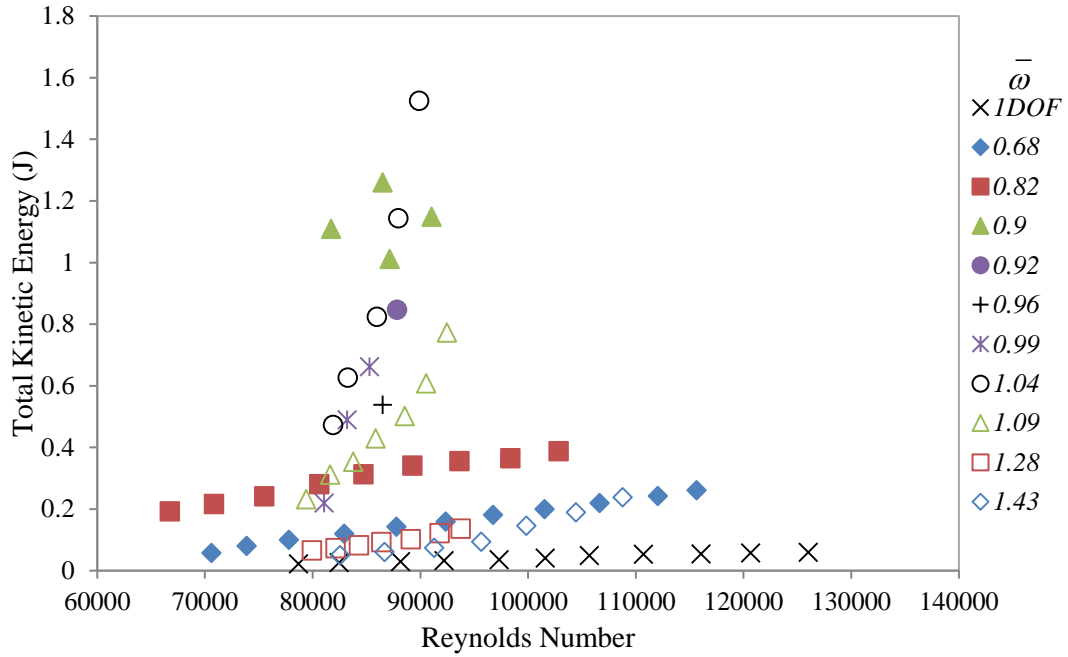
*Figure 4.27: Kinetic energy sum of pitch and heave oscillations for each frequency ratio tested, for increasing Reynolds numbers*
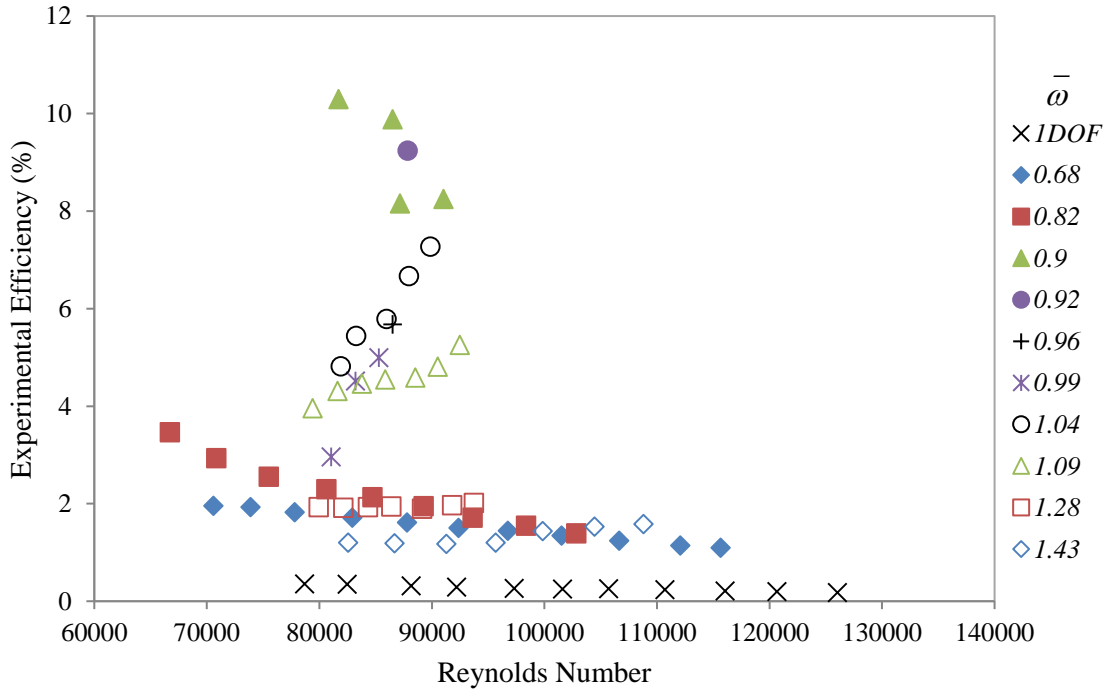


*Figure 4.28: Experimental efficiency of each frequency ratio tested, for increasing Reynolds numbers*

The aerodynamic efficiency follows a different trend from that seen in coupled flutter. The aerodynamic efficiency decreases with Reynolds number for cases where the frequency ratio is below one. For frequency ratios above one however, the aerodynamic efficiency increases with Reynolds number. The rate of change in aerodynamic efficiency, as well as overall magnitude decreases as the frequency ratio moves away from one. The highest values in aerodynamic efficiency occur close to the lock-in region. The energy extraction of the structure thus increases when resonance occurs. This could imply that a higher degree of structural coupling increases the aerodynamic efficiency and energy extraction potential from the flow. The maximum efficiency recorded for these sets of tests is 10.3%. Compared to the results obtained for coupled flutter, the maximum aerodynamic efficiency value for stall flutter is much more reduced than the maximum efficiency value for coupled flutter. It is important to note that it is difficult to effectively compare the differences in efficiencies between both phenomena since they occur within different ranges of Reynolds numbers. In addition, it is not clear if higher efficiencies at higher Reynolds numbers could be obtained through stall flutter, had the experimental rig been designed to withstand increased amplitudes and frequencies of oscillations.

# Chapter 5 – Discussion and Conclusions

The need to develop alternative, clean, sustainable, environmentally benign, and efficient forms of energy generation becomes increasingly imperative as the world population continues to grow exponentially. Since the power generated by the movement of the Earth's atmosphere is estimated to be hundreds of terrawatts, there has been particular interest in wind power generation. The high cost-factor, requirement for large towers, noise concerns, and threat to birds of horizontal-axis wind turbines (HAWTs) has motivated the development of alternative methods to extract energy from the wind [1]. Since there is energy available to be extracted from the flow through LCOs, the potential for a sustainable energy extraction mechanism exists through reciprocating motion. Due to the inherently non-linear nature of both coupled flutter and stall flutter induced LCOs, analytical predictions of their behaviour are limited. The differences in the overall behaviour, as well as the potential of energy extraction, between the stall and coupled flutter induced LCOs, is still not very well understood.

In order to understand the difference between stall and coupled flutter, an experimental study was conducted at the large re-circulating wind tunnel at RMC. The aeroelastic system comprised of a rigid wing with a NACA 0012 profile, free to oscillate in 1DOF pitch and 2DOF pitch and heave. The stiffness in pitch and heave were determined through sets of linear springs. The overall goal of the thesis was to deepen the understanding of the difference between coupled flutter and stall flutter induced LCOs, both in terms of response and energy extraction potential. The objectives of this thesis include investigating which aeroelastic behaviours occur for two different EA locations: at 27% and 35% of the chord length aft of the leading edge. The sensitivity of the pitch and heave amplitude, frequency and phase angle to Reynolds number was analyzed. The difference in behaviour over varying frequency ratios for both types of LCOs was explored. For stall flutter in particular, the effect of the addition of the heave degree of freedom was also explored. The experimental phase-averaged aerodynamic loads per cycle were investigated and compared between configurations. Finally, the experimental efficiencies of each configuration were plotted and compared.

## 5.1 Comparison Between Coupled and Stall Flutter Induced Limit Cycle Oscillations

### 5.1.1 LCO Response Sensitivity to Frequency Ratio and Reynolds Number

For the two EA locations tested, coupled flutter was tested only for an elastic axis location of 27% aft of the leading edge. The oscillations were inferred to be due to coupled flutter because any oscillations died out when the heave motion was blocked. In addition, all oscillations occurred at airspeeds above those obtained from analytical predictions. The

frequency ratios for coupled flutter induced LCOs include $0.67 \leq \bar{\omega} \leq 1.34$ for $3.7 \times 10^4 \leq Re_c \leq 1.4 \times 10^5$. Stall flutter occurred for an elastic axis location at 35% aft of the leading edge, since 1DOF LCOs were recorded in pitch for a range of airspeeds. Four different pitch springs were tested for 1DOF oscillations. The range of frequency ratios for 2DOF oscillations tested included $0.64 \leq \bar{\omega} \leq 1.43$, and the range in Reynolds numbers $5.6 \times 10^4 \leq Re_c \leq 1.3 \times 10^5$.

Both types of flutter produced LCO trends that varied with frequency ratio. Both responses were influenced by non-linear content. Also for both types of flutter, higher non-linear content is found in the pitch response rather than the heave response. This is exhibited by the prominent odd super-harmonics in the spectral content of the pitch oscillations, as well as the additional hysteresis loops in the experimental aerodynamic moment curves. Both types of flutter induced LCOs also produced oscillations for certain configurations which resembled SHM behaviour. Oscillations at all frequency ratios produced this kind of well-behaved response for coupled flutter. Well-behaved oscillations only occurred for stall-flutter induced LCOs where $\bar{\omega} \neq 1$. When the frequency ratio approached one for stall flutter induced LCOs however, a periodic interference pattern, or beating phenomenon, occurred as a result of the interaction between two frequencies. One of the frequencies was pitch dominated, and the other heave dominated.

The behaviour of the pitching amplitude with increasing Reynolds number differs greatly between coupled flutter and stall flutter induced LCOs. For coupled flutter LCOs, the highest amplitudes occur for frequency ratios slightly above one, and all frequencies tend to converge towards a common value. Pitch amplitudes are seen to increase with increasing Reynolds number for frequency ratios below one. On the other hand, pitch responses for frequency ratios above one decreased towards a common value with increasing Reynolds number. Conversely for stall flutter induced LCOs, the introduction of the heave degree-of-freedom does not significantly affect the pitch amplitude. The pitch amplitudes for all frequency ratios are close in value to the 1DOF case for increasing Reynolds number. Similar to the behaviour observed by Dimitriadis and Li, the pitch amplitude for stall flutter LCOs increases with Reynolds number until it reaches a plateau of about 45° [24]. For both the stall and coupled flutter LCOs, the heave RMS amplitudes increase with Reynolds number. For coupled flutter, the branches may originate from a single point, similar to the observations by Pigolotti et al., however it is still unclear [21]. The rate of increase of the heave amplitude RMS branches increases for frequency ratios close to one for stall flutter LCOs. The phase angle between the 2DOFs increases with Reynolds number towards an asymptotic value of approximately 160°. The phase angles may approach 180° with increasing Reynolds number, indicating a tend towards a forced system. Comparatively, the phase angle between the 2DOFs in stall flutter remains mostly unchanged with increasing Reynolds number across frequency ratios for stall flutter LCOs. However, the phase angle changes from approximately 150° to in-phase with increasing frequency ratio for a constant Reynolds number. This also supports the observation that stall flutter is a forced, pitch-driven system for frequency ratios outside of one.

All reduced frequency values for both LCO cases are above 0.05, indicating a high level of aerodynamic unsteadiness. They vary little across frequency ratios and decrease with Reynolds number. However, the coupled flutter case follows a more exponential profile, while the trend for stall flutter is more linear. The LCO frequency increases with Reynolds number for both cases. The sensitivity of the frequency with Reynolds number differs between coupled and stall flutter. Similar to the behaviour of pitch amplitude for coupled flutter induced LCOs, the frequency increases with frequency ratio and tends to converge towards a common value. Also similar to the pitch amplitude for stall flutter, all values across frequency ratios follow the 1DOF case closely, and unlike the coupled flutter case, follow a more linear trend.

Plotting the experimental unsteady moment curves over pitch angle, the curves for both LCO types contain hysteresis loops. The appearance of hysteresis loops indicates non-linearity in the response associated with separated flow. The lift curves all follow more elliptical shapes, although they are also influenced by non-linear content. For both flutter cases, the majority of the positive work is done by the lift. For coupled flutter induced LCOs, the lift does all of the work since stabilizing regions make up the majority of the enclosed area of the curves, the resulting total work done by the moment being negative. The 2DOF moment curves are similar to the 1DOF curve for stall flutter where a stabilizing region is enclosed by two destabilizing loops.

The introduction of the heave degree of freedom was found to have a significant impact on the stall flutter LCO response for frequency ratios close to one. Outside a frequency ratio of one, 2DOF stall flutter is a forced problem, where the pitch oscillations drive the heave motions. This observation is supported by the fact that the pitch amplitude values are very close in value to the 1DOF case, and the moment curves also closely resemble the ones produced by 1DOF LCOs. At a particular Reynolds number, the phase angle between the 2DOFs switches from about 150° to in-phase as the frequency ratio increases, indicating a forced excitation. Behaviour around a frequency ratio of one is characterised by a resonance-like effect, where the heave amplitude RMS is markedly increased compared to frequency ratios below and above one. Further analysis was carried out, where the ratio of the LCO frequency and the natural frequency in heave was plotted over the inverse of the frequency ratio. On the subsequent plot, the characteristic plateau of a lock-in region appears. Also observed are the two interacting frequencies which produce the beating phenomenon in the region where the behaviour changes from forced to coupled motion. A weak coupling, or feedback interaction, occurs as the heave oscillations lock in to the pitch-driven motions around a frequency ratio of one. The resonant heave behaviour, as well as the characteristic plateau which occurs within a lock-in region, support the idea that a weak coupling occurs between the pitch and heave DOFs.

## 5.1.2 Energy Extraction Behaviour and Potential of Limit Cycle Oscillations

Of the two types of flutter induced LCOs, significantly higher efficiencies are achieved through coupled flutter. The highest value is close to 45%, for frequency ratios slightly above one at the lowest airspeed tested. The efficiency decreases exponentially with increasing

Reynolds number. The parameters of the LCO response which govern efficiency are unclear, however the configuration which produced the highest efficiency was at a frequency ratio of 1.14. The pitch amplitude (71.1°), frequency (3.05 Hz), heave amplitude RMS (2.51 cm) were the highest, and the phase angle (24.2°) the lowest out of the other configurations at the Reynolds number ($3.75 \times 10^4$) where maximum efficiency occurs. However, as the efficiencies decrease exponentially with Reynolds number, the phase angles between the 2DOFs increase and tend towards 180° as an inverse function. Comparatively, the highest efficiency achieved through stall flutter induced LCOs was 10.3% at a frequency ratio of 0.9. The highest efficiencies produced by stall flutter induced LCOs occurred within the lock-in region. The efficiency of the LCO decreased with increasing Reynolds number for frequency ratios below one, and increased with Reynolds number for frequency ratios above one. The rate of increase of the trends was increased for frequency ratios closer to one. The highest efficiency values also corresponded with phase angles between the 2DOFs falling between 0° and 180°.

From these results, it can be concluded that coupling between pitch and heave is crucial for energy extraction from a flow using a reciprocating design. In addition, it appears that the phase angle between the 2DOFs and inclusion of the heave degree of freedom influences energy extraction. More energy is extracted for phase angles between 0° and 180°. Allowing the heave degree of freedom to oscillate greatly increases the energy uptake for stall flutter induced LCOs, which is inherently a 1DOF problem. The same observation was made for 2DOF SAOs by Poirel and Mendes [13]. Understanding the dynamics of the entire system is therefore essential to obtain maximum efficiencies from a kinematically-passive device driven by aeroelastic instability.

The potential for the design of a new type of energy extracting device through reciprocating motion has been realized in this thesis. This stands in contrast to the better understood traditional wind-turbine problem, which is both kinematically and dynamically different. Wind-turbines rely on continuous rotational motion. On the other hand, the amount of energy extractable though the reciprocating device studied depends on its aeroelastic response, and on the underlying physical tenets of the flutter. It is important to note that the theoretical maximum percent of extractable energy from a flow is known as the Betz limit, and is analytically derived to be 59.3% [38]. The maximum efficiency obtained from this study meets or exceeds the aerodynamic efficiencies of other simulated prototypes of reciprocating designs. The results for efficiency are also comparable to conventional rotary designs. In practice, the most efficient HAWTs extract a maximum of about 45% of the available wind power. The performance of the two types of devices can only be compared at low airspeeds however. The design used in this study therefore may have more potential for use at low airspeeds. Conditions with reduced airspeed include heights close to the ground, where traditional HAWTs experience problems with performance. Therefore, there may be promise to favour similar designs based on reciprocating motion in applications where the use of HAWT towers becomes problematic. Potential for subsequent development thus exists for use in remote areas, such as defense

applications and First Nation communities for example, where the transportation of large towers becomes impractical.

## 5.2 Recommendations for Future Work

Subsequent development is required in extending this work to explore the practical applicability of a reciprocating device using aeroelastic instability as well as furthering the understanding of the physics. The effect of including a generator or load to the design, as well as its effect on the aeroelastic response should be considered as the next step. Experiments with a load (simulated or physical) can be performed in order to generate responses with more realistic structural damping values and phases between pitch and heave motions. In addition, scaling the parameters of the system in this study for practical applications should be investigated.

Further experiments should also consider using a more robust test set-up to explore the physics of aeroelastic phenomena at the extremities of the Reynolds numbers explored in this study. The physics of 2DOF stall flutter has potential for additional study, especially at higher Reynolds numbers than the ones explored in this study. Exploring the system's capabilities to extract energy at lower Reynolds number through coupled flutter induced LCOs for higher efficiencies should also be considered. The nature of the aerodynamic nonlinearity of the system remains unclear. The influence of the separated flow during the LCO cycle, as well as the importance and nature of shed LEVs in both coupled and stall flutter remains to be seen. This may be achieved through experimental means, such as Particle Image Velocimetry (PIV), or through numerical means such as Large Eddy Simulations (LES).

In addition, the effect of free-stream turbulence on both types of LCO responses is also not fully understood. Subsequent experimental investigations should include a turbulence grid. The effect of free-stream turbulence becomes important when analyzing the feasibility of using a kinematically-passive device for outdoor applications, since the atmospheric boundary layer contains high levels of turbulence.

# References

[1] Young, J., Lai, J.C.S. and Platzer, M.F. "A review of progress and challenges in flapping foil power generation", *Progress in Aerospace Sciences.* Vol. 67, 2014, pp. 2-28.

[2] Patil, M.J. "From Fluttering Wings to Flapping Flight: The Energy Connection", *Journal of Aircraft,* Vol. 40, No. 2, pp. 270-276, 2003

[3] Fung, Y.C. *An Introduction to the Theory of Aeroelasticity,* Wiley, Dover, 1993

[4] Dowell, E., Edwards, J. and Strganac, T. "Nonlinear Aeroelasticity", *Journal of Aircraft,* Vol. 40, No. 5, pp. 857-874, 2003

[5] Henderson M.L. and McMasters J.H. "Low-speed Single-element Airfoil Synthesis", Technical Soaring, Vol. 6, pp.1-21, 1980

[6] Kinsey, T. and Dumas, G. "Optimal Operating Parameters for an Oscillating Foil Turbine at Reynolds Number 500,000", *AIAA Journal,* Vol. 52, No. 6, 2014

[7] McKinney, W. and DeLaurier, J. "The Wingmill: An Oscillating-Wing Windmill", *Journal of Energy,* Vol. 5, No. 2, pp. 109-121, 1981

[8] Kinsey, T. and Dumas, G. "Parametric Study of an Oscillating Airfoil in a Power-Extraction Regime", *AIAA Journal,* Vol. 46, No. 6, pp. 1318-1330, 2008

[9] Lalande, G. "Conception d'un prototype expérimental d'hydrogénérateur à ailes oscillantes", Master's thesis ; Dept. of Mech. Eng., Laval University; Quebec City, Canada; 2011

[10] Platzer, M.F., Ashraf, M.A., Young, J. and Lai, J.C.S. "Extracting Power in Jet Streams: Pushing the Performance of Flapping Wing technology", *27th International Congress of the Aeronautical Sciences, 2010.*

[11] Veilleux, J. and Dumas, G. "Numerical Optimization of a fully-passive flapping-airfoil turbine", *Journal of Fluids and Structures,* Vol 70, pp. 102-130, 2017

[12] Harris, Y. "The Aeroelastic Dynamics of a NACA 0012 Airfoil Oscillations in Pitch at Transitional Reynolds Numbers," Master's Thesis, Royal Military College of Canada, Kingston, Ontario, Canada, 2007.

[13] Poirel, D. and Mendes, F. "Experimental Small-Amplitude Self-Sustained Pitch-Heave Oscillations at Transitional Reynolds Numbers", *AIAA Journal,* Vol. 52, No. 8, 2014, pp. 1581-1590.

[14] Mendes, F. "Self-Sustained Aeroelastic Oscillations of a 2DOF NACA 0012 Airfoil at Transitional Reynolds Numbers", Master's Thesis, Royal Military College of Canada, Kingston, Ontario, Canada, 2016

[15] Poirel, D., Harris, Y. and Benaissa, A. "Self-Sustained Aeroelastic Oscillations of a NACA0012 Airfoil at Low-to-Moderate Reynolds Numbers", *Journal of Fluids and Structures,* Vol. 24, No. 5, 2008, pp. 700-719.

[16] Peristy, L., Poirel, D. and Yuan, W. "Characterization of the Aeroelastic Behaviour of a NACA0012 Airfoil at Transitional Reynolds Numbers", *CSME International Congress*, Toronto, Canada, June 1-4, 2014

[17] Peristy, L. "Examination of Small and Large Amplitude Aeroelastic Oscillations in Pitch of a NACA0012 airfoil", Master's Thesis, Royal Military College of Canada, Kingston, Ontario, Canada, 2014.

[18] Goyaniuk, L., Poirel, D., Benaissa A. and Yuan W. "Analysis of One Degree-of-Freedom Stall Flutter Limit Cycle Oscillations", *63rd CASI Aeronautics Conference,* Toronto, Canada, May 16-18th, 2017.

[19] Poirel, D. "Random Dynamics of a Structurally Nonlinear Airfoil in Turbulent Flow", Ph.D. Thesis, McGill University, Montreal, Quebec, Canada, 2001

[20] Theodorsen, T. "General Theory of Aerodynamic Instability and the Mechanism of Flutter", NACA report 496, 1935

[21] Pigoloti, L., Mannini C. and Bartoli, G. "Experimental study on the flutter-induced motion of two-degree-of-freedom plates", *Journal of Fluids and Structures,* Vol 75, pp. 77-98, 2017

[22] Halfman R., Johnson H.C. and Haley S.M. "Evaluation of High-Angle-of Attack Aerodynamic-Derivative Data and Stall-Flutter Prediction Techniques", Technical Note 2533, Massachusetts Institute of Technology, Cambridge, Massachusetts, USA, 1951

[23] McCroskey W. *The phenomenon of dynamic stall,* NASA TM-81264, 1981

[24] Dimitriadis, G. and Li, J. "Bifurcation of Airfoil Undergoing Stall Flutter Oscillations in Low-Speed Wind Tunnel", *AIAA Journal,* Vol. 47, No. 11, pp. 2578-2596, 2009

[25] Bhat, S. and Govardhan, R. "Stall flutter of NACA 0012 airfoil at low Reynolds numbers", *Journal of Fluids and Structures,* Vol. 41, pp. 166-174, 2013

[26] Blevins, R. *Flow-Induced Vibrations,* Krieger Publishing Company, Malabar, Florida USA, 2001

[27] Williamson, C.H.K. "Vortex Dynamics in the cylinder wake", *Annual Reviews of Fluid Mechanics,* Vol. 28, pp. 477-539, 1996

[28] Poirel, D., Goyaniuk, L. and Benaissa, A. "Frequency Lock-in in Pitch-Heave Stall Flutter", *Journal of Fluids and Structures,* Vol. 79, pp. 14-25, 2018

[29] Mueller, T.J. "Low Reynolds Number Vehicles," AGARD AG-288, 1985.

[30] Gad-el-Hak, M. "Control of Low-Speed Airfoil Aerodynamics", *AIAA Journal,* Vol. 28, No. 9, pp. 1537-1552, 1990

[31] Huang, R.-F. and Lin, C. "Vortex Shedding and Shear-Layer Instability of Wing at Low-Reynolds Numbers," *AIAA Journal,* Vol. 33, No. 8, pp. 1398-1403, 1995

[32] Métivier, V., Dumas, G., and Poirel D. "Effects of Inertia and Boundary Layer Tripping on Aeroelastic, Self-Excited Pitch Oscillations of an Airfoil," *56th CASI Aeronautics Conference and Annual General Meeting,* Ottawa, Canada, May 2009

[33] Yuan, W., Poirel, D., Wang, B., and Benaissa, A. "Effect of Freestream Turbulence on Airfoil Limit-Cycle Oscillations at Transitional Reynolds Numbers," *Journal of Aircraft,* Vol 52, No. 4, pp. 1214-1225, 2015

[34] O'Meara M. and Mueller T.J. "Laminar Separation Bubble Characteristics on an Airfoil at Low Reynolds Numbers", AIAA Journal, Vol. 25, No. 8, 1987, pp. 1033-1041.

[35] Worden, K. and Tomlinson G.R. *Nonlinearity in Structural Dynamics,* Institute of Physics, 1993

[36] White, F.M. *Viscous Fluid Flow,* Third Edition, McGraw-Hill, 2006

[37] Manwell, J.F., McGowan, J.G. and Rogers, A.L. *Wind Energy Explained*, Wiley, 2009

# Appendix A – Blockage Calculations

## A.1 Cross Sectional Areas of Experimental Rig Components

The frontal cross-sectional areas of each component in the test rig are listed in the Table A.1 below. The cross-sectional area based on the frontal projection of the wing at 0°, as well as at the maximum pitch angle observed in experiment of 77.5°, are also included. This angle is used in order to determine the maximum blockage that was experienced during testing.

| | Area (m²) |
|---|---|
| end plate supports | 0.0038 |
| end plates | 0.0195 |
| fiberglass rods | 0.0021 |
| airfoil, $\theta = 0°$ | 0.0114 |
| airfoil, $\theta = 77.5°$ | 0.0929 |

*Table A.1 Experimental rig frontal areas*

The total areas of the obstructions for each pitch angle case are shown below in Table A.2.

| | Area (m²) |
|---|---|
| total frontal area, $\theta = 0°$ | 0.0368 |
| total frontal area, $\theta = 77.5°$ | 0.118 |

*Table A.2 Total frontal areas of obstructions*

Since the areas of all the test components at as obstructions, they reduce the effective cross-sectional area which permits the free-stream flow. Table A.3 below presents the unobstructed cross-sectional area ($A_{TS}$) of the test section, as well as the cross-sectional area of the free-stream with obstructions ($A'_{TS}$) for each pitch angle case.

| | Area (m²) |
|---|---|
| unobstructed test section | 0.821 |
| obstructed test section, $\theta = 0°$ | 0.784 |
| obstructed test section, $\theta = 77.5°$ | 0.702 |

*Table A.3 Total unobstructed and obstructed cross-sectional*

## A.2 Blockage Calculations

The free-stream airspeed ($U'_{TS}$) due to the obstructions in the test section is calculated using equation A.1 below:

$$U'_{TS} = \frac{A_{TS}}{A'_{TS}} U_{TS} \qquad \text{[A.1]}$$

The percent increase in the free-stream airspeed due to the obstructions ($\delta U$) is:

$$\delta U = \frac{U'_{TS} - U_{TS}}{U_{TS}} x100\% \qquad \text{[A.2]}$$

### A.2.1 Blockage for a Wing at $\theta = 0°$

From equation A.1, and using the calculated values presented in Table A.3, the blockage created by the wing at 0° is:

$$U'_{TS} = \frac{0.821}{0.784} U_{TS} = 1.047 U_{TS}$$

$$\delta U = \frac{1.047 U_{TS} - U_{TS}}{U_{TS}} x100 = 4.7\%$$

### A.2.2 Blockage for a Wing at $\theta = 77.5°$

The maximum blockage experienced throughout this study is:

$$U'_{TS} = \frac{0.821}{0.702} U_{TS} = 1.168 U_{TS}$$

$$\delta U = \frac{1.168 U_{TS} - U_{TS}}{U_{TS}} x100 = 16.8\%$$

The value is below 20%, and is not considered to significantly influence the results of this study.

# Appendix B – Convergence Study

In order to determine the adequate sample size of data collected, a convergence study was performed. For this study, 2DOF LCOs due to coupled flutter were analyzed in order to determine at which sample size the magnitude of the amplitude of oscillation ceased to change. The configuration used was for an elastic axis location at 27% the chord length, and a frequency ratio of 1.04. Data was collected for 120 seconds, at a sampling frequency of 1 kHz. There was difficulty obtaining data beyond a 200 second sample. LCO data was collected for three different airspeeds. A manual perturbation was used in order to induce LCOs. Once data was collected, the oscillation was manually ceased, the RPM increased, and the process repeated twice more. Attention was paid to the LCO response to ensure that data was collected only once the system reached steady state. The ammeter was monitored in order to confirm little variation in airspeed at each value of fan RPM.
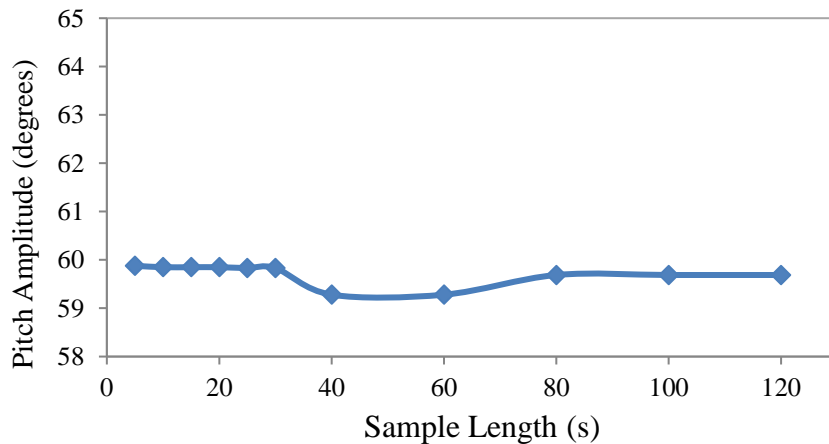


*Figure B.1: Pitch amplitude values for various sample sizes at an airspeed of 3.95 m/s, and a maximum sample size of 120 seconds.*
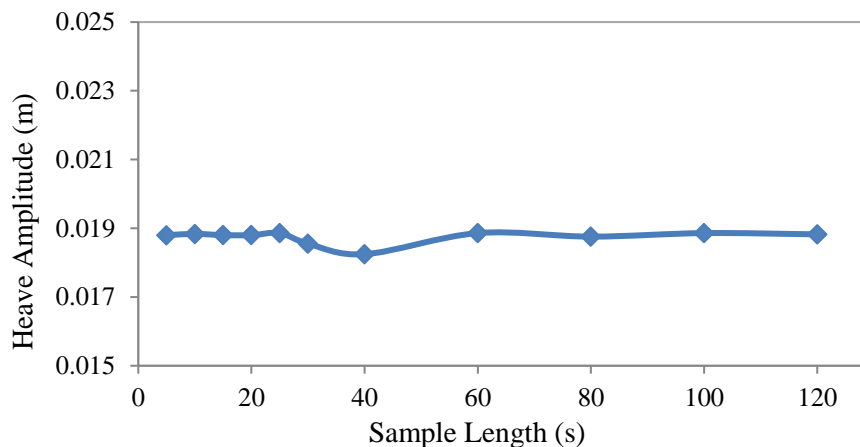


*Figure B.2: Heave amplitude values for various sample sizes at an airspeed of 3.95 m/s, and a maximum sample size of 120 seconds*

Pitch and heave amplitudes were calculated from the modes of the corresponding histograms using 200 bins. The amplitudes were calculated from various increasing sample lengths, with the maximum size being 120 seconds. The results are presented in the figures below. As can be observed, the amplitude values appear to level off at about 80 seconds. From this information, the majority of the analysis in this thesis was conducted for a sample length of 80 seconds.
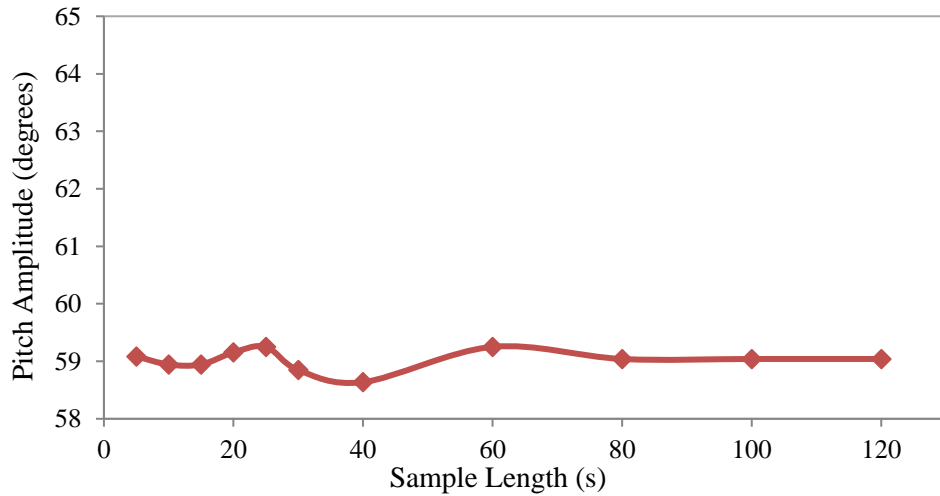


*Figure B.3: Pitch amplitude values for various sample sizes at an airspeed of 4.09 m/s, and a maximum sample size of 120 seconds.*
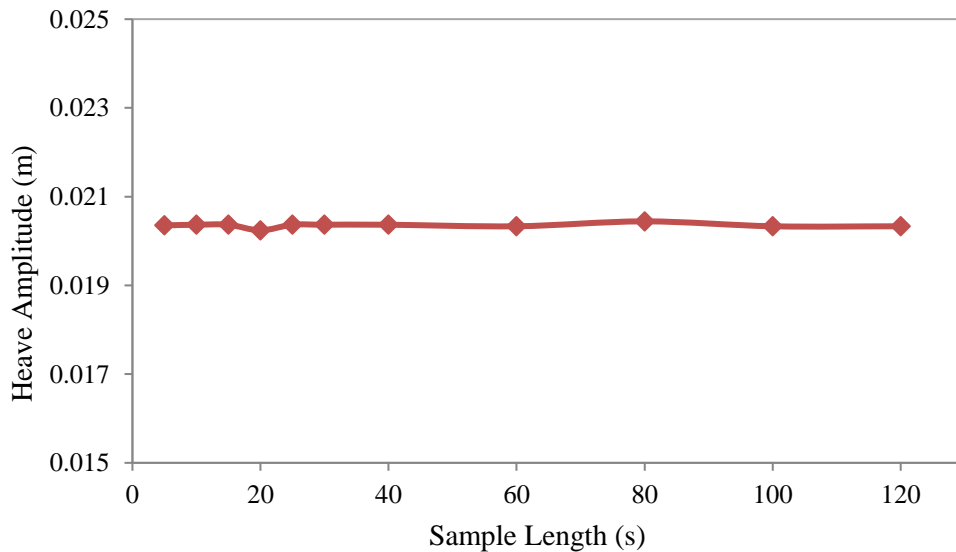


*Figure B.4: Heave amplitude values for various sample sizes at an airspeed of 4.09 m/s, and a maximum sample size of 120 seconds.*
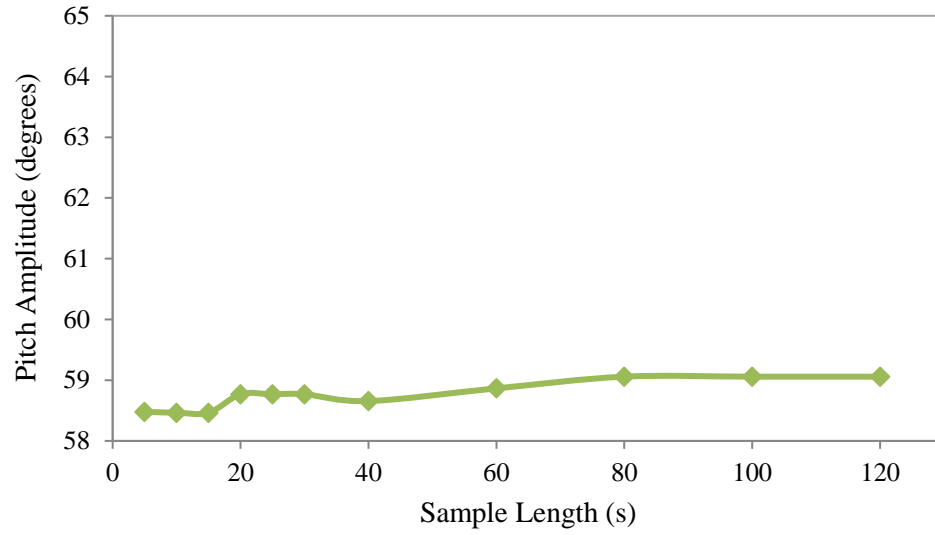
*Figure B.5: Pitch amplitude values for various sample sizes at an airspeed of 4.23 m/s, and a maximum sample size of 120 seconds.*
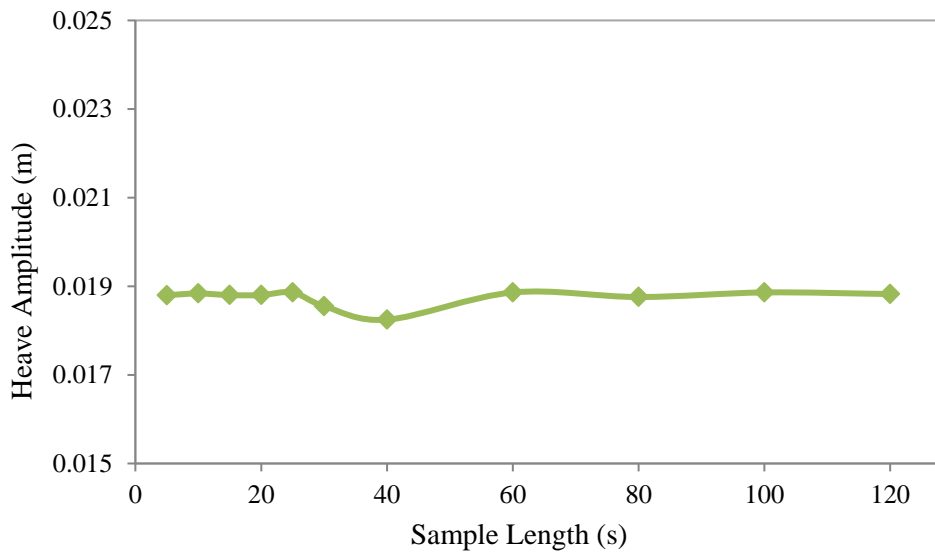


*Figure B.6: Heave amplitude values for various sample sizes at an airspeed of 4.23 m/s, and a maximum sample size of 120 seconds.*

# Appendix C – Initial Conditions

The influence of initial conditions on the response of a 1DOF LCO was studied. The pitch stiffness $K_\theta$ was kept at 0.3 Nm/rad. The effect of increasing and decreasing airspeed was explored, and was compared to an LCO response where the oscillations are induced from rest at each airspeed increment.

Three runs were conducted, the Run 1 had the airspeed increased to a maximum, then decreased. For this test, a manual perturbation initially induced the LCO, however the wing was allowed to oscillate without interruption for the remainder of the test run. Data was collected when the LCO amplitude was deemed to have reached steady state at each airspeed increment. Run 2 was conducted similarly to the first, however the airspeed was decreased first from a maximum airspeed to the minimum, then increased. A perturbation was induced at each airspeed increment, and data was recorded when the LCOs reached steady state for Run 3. Before the airspeed was increased, the LCOs were stopped such that the wing remained at rest while the airspeed was increased.

The results for LCO amplitude and frequency from each test run were plotted with airspeed. They are presented below in Figures C.1 and C.2. It can observed that initial conditions with airspeed do not significantly affect the LCO response. Regardless, the same initial conditions in Run 3 were used throughout the study.
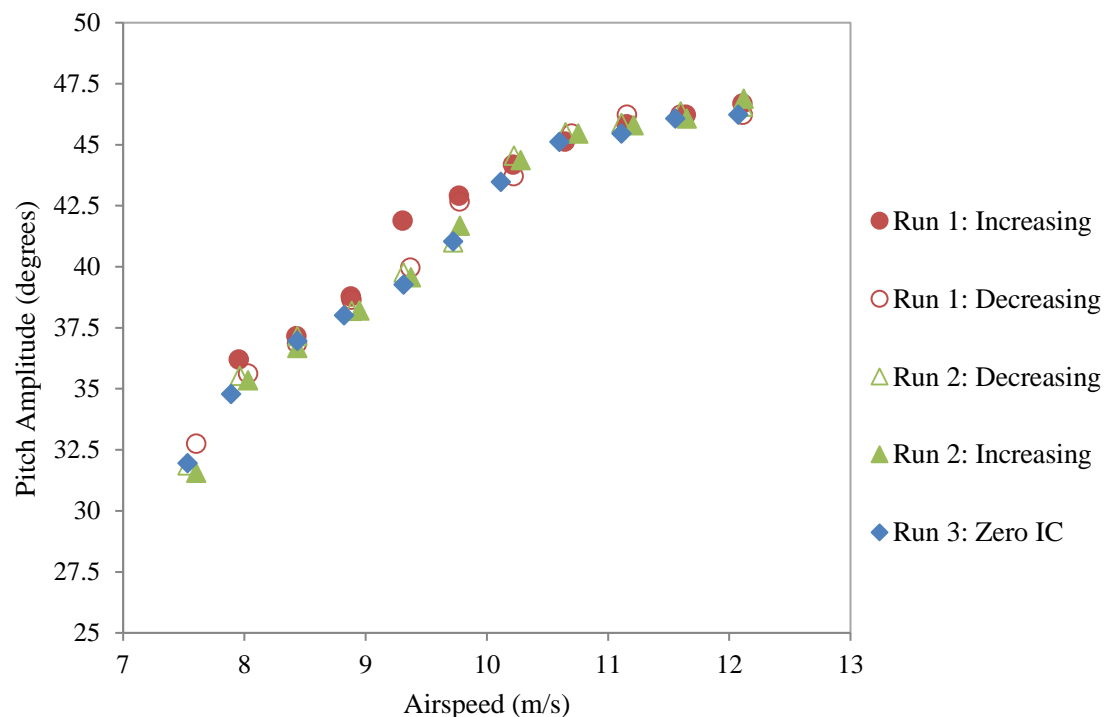


*Figure C.1: 1DOF stall flutter LCO amplitude for different initial conditions in airspeed.*
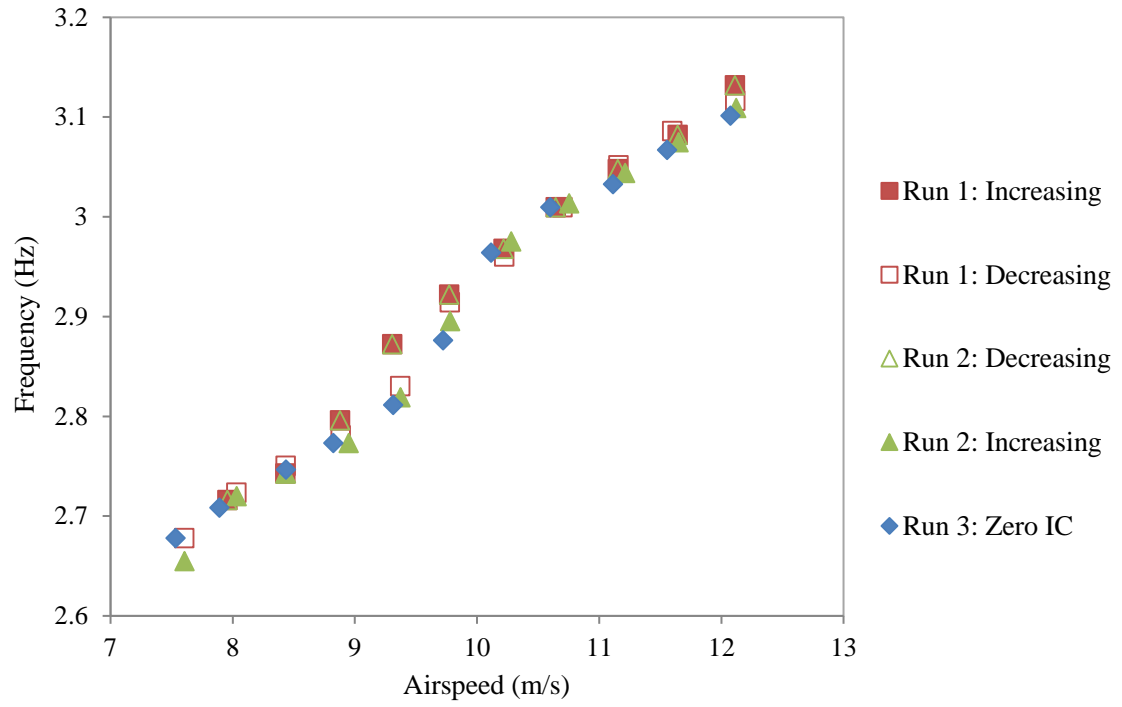
*Figure C.2: 1DOF stall flutter LCO frequency for different initial conditions in airspeed.*

# Appendix D – Differentiation Scheme

A five-point formula is used for the numerical differentiation of the velocity and acceleration terms for both pitch and heave [35]. Once calculated over a time interval, knowing the structural terms, the moment and lift could be calculated from the equations of motion 1.2 and 1.3. Little difference in values was found between results obtained using a five-point versus seven-point equation. Sample equations for velocity and acceleration in pitch are shown below.

$$\dot{\theta} = \frac{1}{12\Delta t}(-\theta_{i+2} + 8\theta_{i+1} - 8\theta_{i-1} + \theta_{i-2}) \qquad \text{[D.1]}$$

$$\ddot{\theta} = \frac{1}{12\Delta t}(-\dot{\theta}_{i+2} + 8\dot{\theta}_{i+1} - 8\dot{\theta}_{i-1} + \dot{\theta}_{i-2}) \qquad \text{[D.2]}$$

# Appendix E – List of Experiments

Included in the tables below is a summary of each experiment. The damping ratio and structural damping constants were averaged from the results obtained from no-flow tests. The stiffness in pitch and heave were determined from the averages of the slopes of the linear curves obtained from calibration.

| EA Location | Test Date | Range of Airspeeds | Configuration | $\zeta_\theta$ | $D_\theta$ (Nms/rad) | $\zeta_h$ | $D_h$ (Ns/m) | $K_\theta$ (Nm/rad) | $K_h$ (N/m) |
|---|---|---|---|---|---|---|---|---|---|
| 27% the chord length | March 3rd, 2017 | 9.28 m/s - 13.99 m/s | $\bar\omega = 0.67$ | 0.0333 | 0.0012 | 0.0796 | 4.51 | 0.3 | 307.1 |
| | March 4th, 2017 | 9.16 m/s -12.95 m/s | $\bar\omega = 0.71$ | 0.0332 | | 0.0729 | 4.36 | | 343.775 |
| | August 18th, 2016 | 6.41 m/s - 12.12 m/s | $\bar\omega = 0.86$ | 0.0394 | 0.0014 | 0.0293 | 2.1 | | 503.8 |
| | August 25th, 2016 | 6.24 m/s - 12. 6 m/s | | 0.0379 | | 0.0271 | 2.00 | | |
| | March 6th, 2017 | 5.36 m/s - 10.52 m/s | $\bar\omega = 0.93$ | 0.0325 | 0.0011 | 0.0544 | 4.22 | | 586.71 |
| | March 7th, 2017 | 4.74 m/s - 8.01 m/s | $\bar\omega = 1.01$ | 0.0326 | 0.0012 | 0.0541 | 4.73 | | 693 |
| | March 27th, 2017 | 4.73 m/s - 10.43 m/s | | 0.0313 | 0.0011 | 0.0455 | 3.87 | | |
| | March 8th, 2017 | 4.25 m/s - 6.46 m/s | $\bar\omega = 1.04$ | 0.0316 | 0.0011 | 0.0516 | 4.49 | | 738.05 |
| | April 7th, 2017 | 4.27 m/s - 10.35 m/s | | 0.0321 | | 0.0446 | 3.89 | | |
| | August 10th, 2016 | 3.94 m/s - 6.83 m/s | $\bar\omega = 1.09$ | 0.0443 | 0.0013 | 0.0261 | 2.86 | | |
| | August 15th, 2016 | 3.92 m/s - 8.84 m/s | | 0.0388 | 0.0014 | 0.0282 | 2.39 | | 805.4 |
| | August 18th, 2016 | 3.65 m/s - 7.08 m/s | $\bar\omega = 1.14$ | 0.0382 | | 0.0206 | 1.94 | | 889.69 |
| | March 10th, 2017 | 6.07 m/s - 6.16 m/s | $\bar\omega = 1.34$ | 0.0325 | 0.0011 | 0.0399 | 4.43 | | 1229.26 |

*Table E.1: List of coupled flutter tests for each configuration performed with the elastic axis set at 27% the chord length.*

| EA Location | Test Date | Range of Airspeeds | Configuration | $\xi_\theta$ | $D_\theta$ (Nms/rad) | $\xi_h$ | $D_h$ (Ns/m) | $K_\theta$ (Nm/rad) | $K_h$ (N/m) |
|---|---|---|---|---|---|---|---|---|---|
| 35% the chord length | October 30th, 2016 | 5.69 m/s - 11.15 m/s | *1DOF* | 0.0364 | 0.0009 | N/A | N/A | 0.15 | N/A |
| | October 31st, 2016 | 6.22 m/s - 11.08 m/s | *1DOF* | 0.0352 | | | | 0.2 | |
| | March 1st, 2016 | 7.26 m/s - 11.16 m/s | *1DOF, with sandpaper* | 0.0345 | 0.0012 | | | | |
| | September 18th, 2016 | 7.53 m/s - 12.07 m/s | *1DOF* | 0.0308 | 0.0011 | | | | |
| | October 11th, 2016 | 6.81 m/s - 11.17 m/s | $\bar{\omega} = 0.68$ | 0.0295 | | 0.1816 | 3.64 | | 343.775 |
| | October 12th, 2016 | 6.67 m/s - 10.28 m/s | $\bar{\omega} = 0.82$ | 0.0706 | 0.001 | 0.0382 | 2.74945 | | 503.8 |
| | November 18th, 2016 | 6.62 m/s - 10.23 m/s | $\bar{\omega} = 0.82$ | 0.0285 | | 0.0341 | 2.409 | | 503.8 |
| | November 22nd, 2016 | 8.03 m/s - 8.94 m/s | $\bar{\omega} = 0.9$ | 0.0300 | | 0.0576 | 4.56 | | 610.64 |
| | January 30th, 2017 | 8.47 m/s | $\bar{\omega} = 0.92$ | 0.0275 | 0.0009 | 0.0579 | 4.74 | | 637.06 |
| | January 16th, 2017 | 8.34 m/s | $\bar{\omega} = 0.96$ | 0.0245 | 0.001 | 0.0482 | 4.10 | 0.3 | 693 |
| | January 13th, 2017 | 7.82 m/s - 8.23 m/s | $\bar{\omega} = 0.99$ | 0.0317 | 0.0011 | 0.0358 | 3.07 | | 738.05 |
| | August 29th, 2016 | 8.08 m/s - 8.92 m/s | | 0.0320 | | 0.0256 | 2.32 | | 805.4 |
| | December 7th, 2016 | 8.05 m/s - 8.85 m/s | $\bar{\omega} = 1.04$ | 0.0291 | | 0.0376 | 3.37 | | 805.4 |
| | December 9th, 2016 | 8.01 m/s - 8.81 m/s | | 0.0304 | | 0.0343 | 3.08 | | 805.4 |
| | October 14th, 2016 | 7.86 m/s - 9.16 m/s | $\bar{\omega} = 1.09$ | 0.0299 | 0.001 | 0.0282 | 2.65 | | 889.69 |
| | December 13th, 2016 | 7.71 m/s - 8.99 m/s | | 0.0342 | | 0.0380 | 3.54 | | 889.69 |
| | January 23rd, 2017 | 7.71 m/s - 9.05 m/s | $\bar{\omega} = 1.28$ | 0.0289 | | 0.0408 | 4.32 | | 1229.26 |
| | October 26th, 2016 | 7.99 m/s - 10.54 m/s | $\bar{\omega} = 1.43$ | 0.0297 | | 0.0279 | 3.54 | | 1533.24 |
| | December 21st, 2016 | 7.77 m/s - 11.77 m/s | *1DOF* | 0.0298 | 0.0012 | N/A | N/A | | N/A |
| | January 9th, 2017 | 7.71 m/s - 8.65 m/s | $\bar{\omega} = 0.76$ | 0.0298 | | 0.0550 | 3.98 | | 503.8 |
| | January 9th, 2017 | 8.32 m/s - 8.38 m/s | $\bar{\omega} = 0.96$ | 0.0302 | 0.0011 | 0.0492 | 4.41 | 0.35 | 805.4 |
| | December 21st, 2016 | 7.98 m/s - 8.39 m/s | $\bar{\omega} = 1.01$ | 0.0292 | | 0.0393 | 3.66 | | 889.69 |
| | January 10th, 2017 | 7.74 m/s - 8.62 m/s | $\bar{\omega} = 1.32$ | 0.0759 | | 0.03115 | 3.80 | | 1533.24 |

*Table E.1: List of stall flutter tests for each configuration performed with the elastic axis set at 35% the chord length.*

# Appendix F – Additional Stall Flutter LCO Results

Additional experiments for stall flutter induced 2DOF LCOs were conducted for a pitch stiffness of 0.35 Nm/rad, the EA set to 35% the chord length. Although additional frequency ratios at this pitch stiffness should be tested in order to more properly compare behaviours, the preliminary results correlate to the case in the main body. For cases where the frequency ratio is less than or greater than one, the pitch drives the heave motion. A resonance phenomenon is observed, where the amplitude in heave and efficiency are increased for the two frequency ratios closest to one.
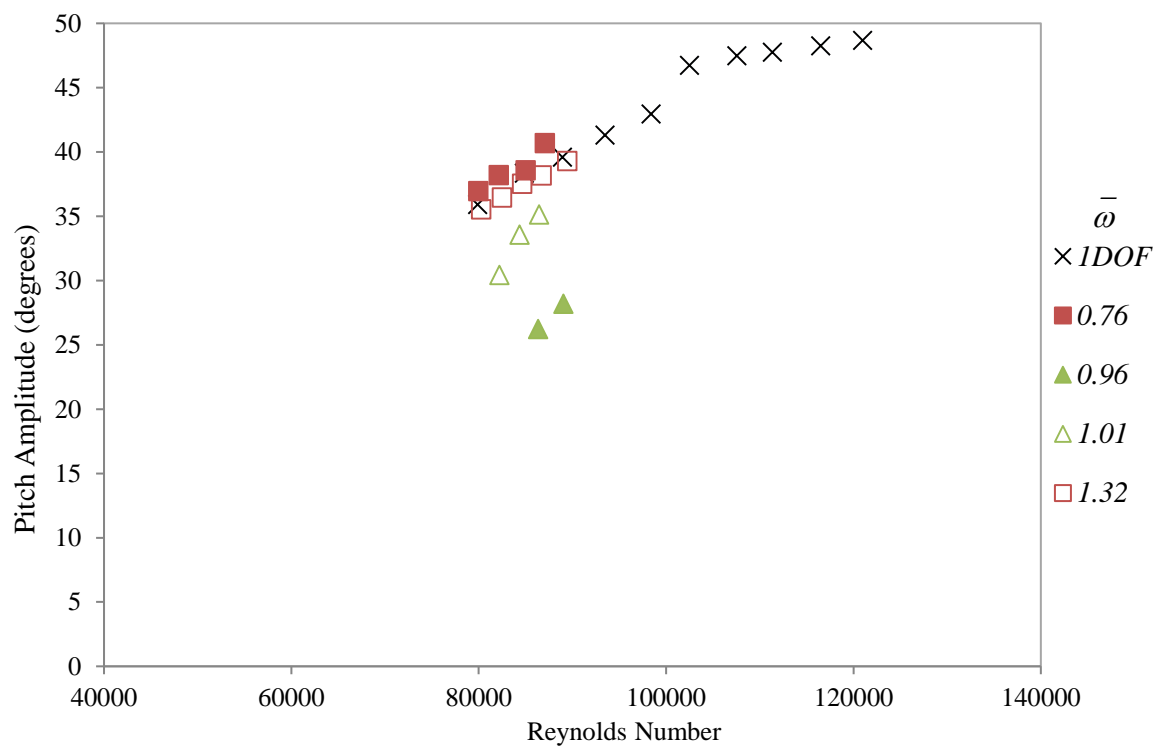


*Figure F.1: Pitch amplitude for each frequency ratio over increasing Reynolds Numbers.*
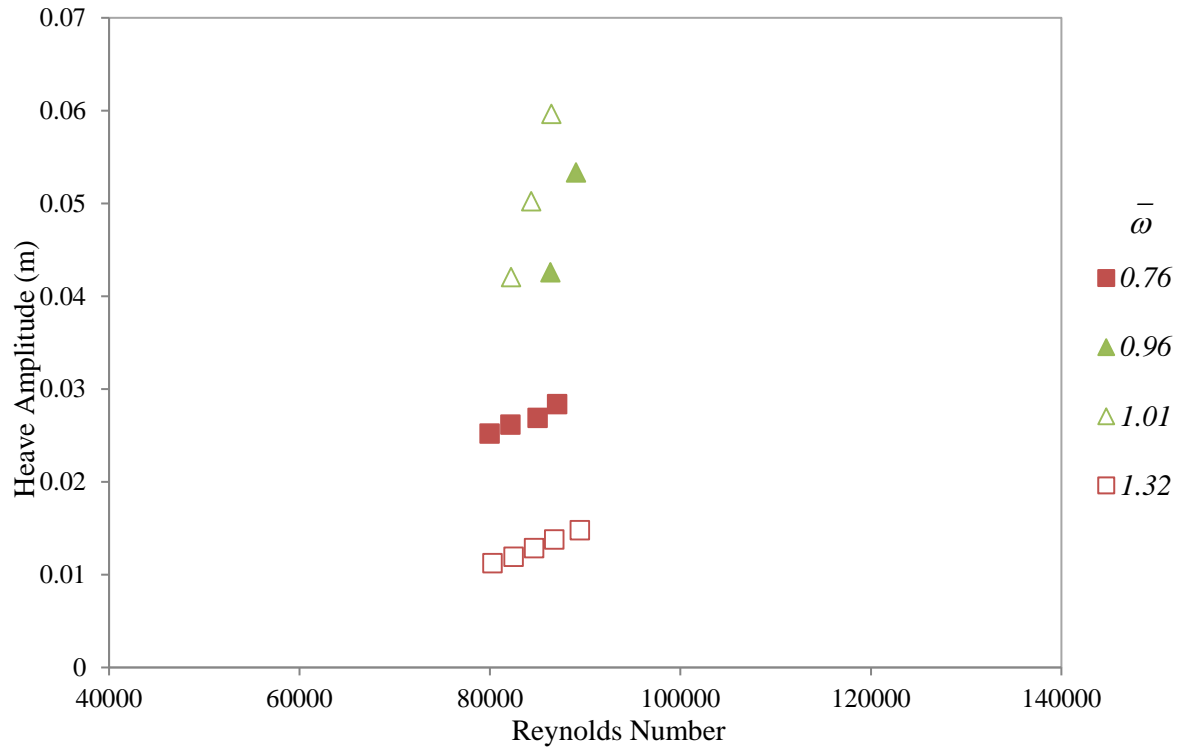
*Figure F.2: Heave amplitude for each frequency ratio over increasing Reynolds Numbers.*
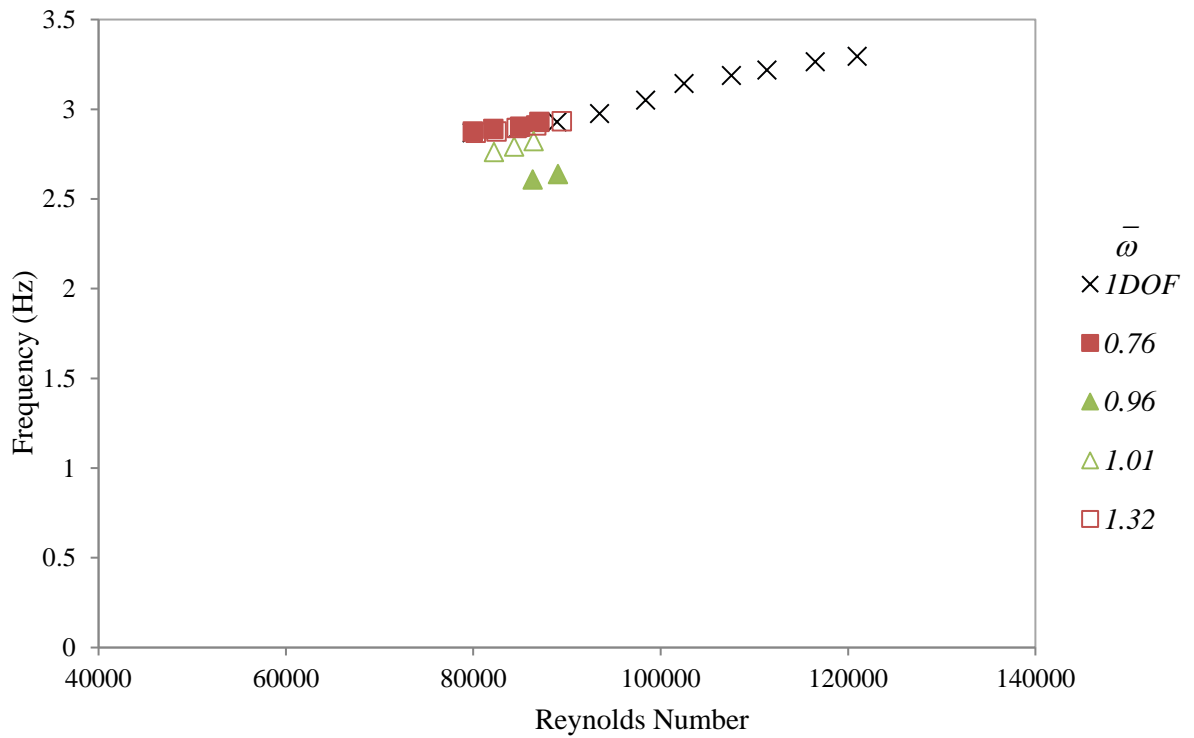


*Figure F.3: LCO frequency for each frequency ratio over increasing Reynolds Numbers*
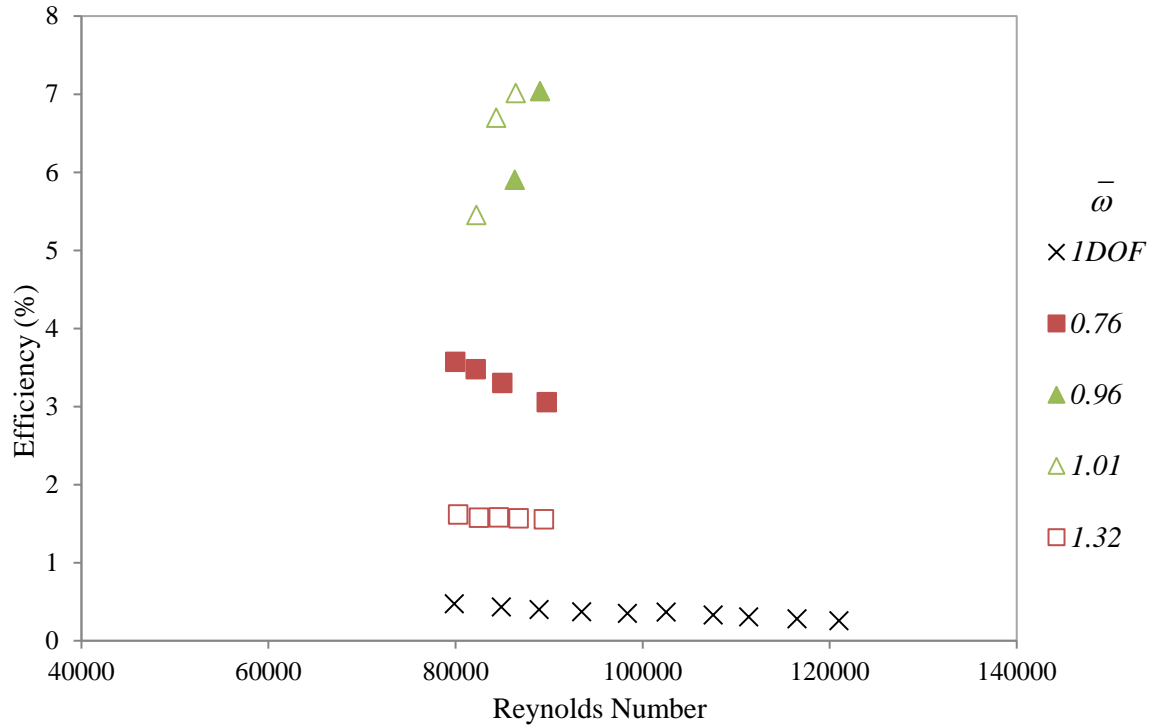
107

*Figure F.4: Aerodynamic efficiency of each frequency ratio tested, for increasing Reynolds Numbers*
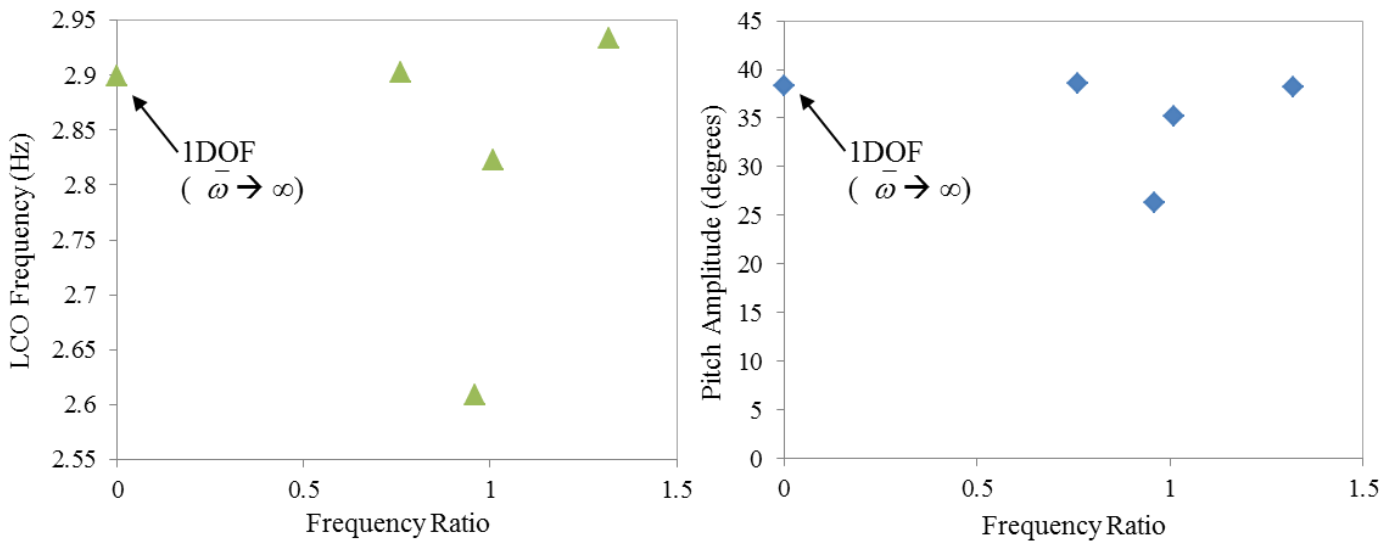


*Figure F.5: Pitch amplitude (right) and LCO frequency (left) as a function of frequency ratio for a Reynolds number of approximately 8.6 x 10$^4$.*
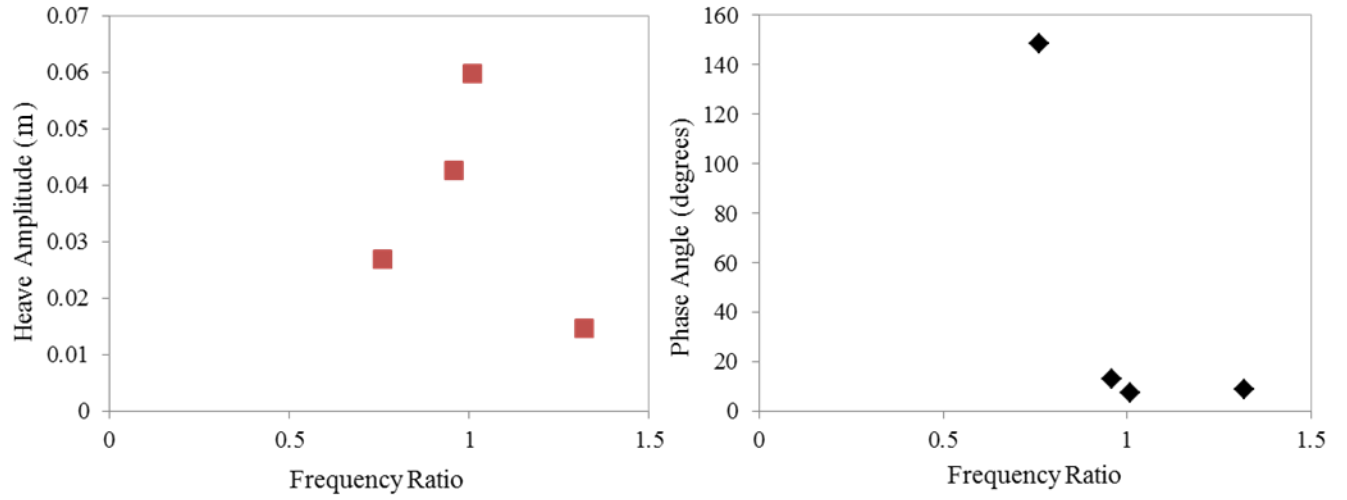
*Figure F.6: Heave Amplitude (left) and phase angle (right) as a function of frequency ratio for a Reynolds number of approximately 8.6 x 10⁴.*

# Appendix G – Uncertainty Analysis

## G.1 Error Propagation

For a function of the form $y = f(x_1, x_2, \ldots, x_n)$, in which $n$ independent variables have uncertainties $\Delta x_1, \Delta x_2, \ldots, \Delta x_n$, the uncertainty in $y$ can be estimated from by using Equation G.1. Here, the uncertainty can be calculated by taking the partial derivatives with respect to each variable, and multiplying each term with their corresponding estimated uncertainties.

$$\Delta y \cong \left| \frac{\partial f}{\partial x_1} \right| \Delta x_1 + \left| \frac{\partial f}{\partial x_2} \right| \Delta x_2 + \cdots + \left| \frac{\partial f}{\partial x_n} \right| \Delta x_n \qquad \text{[G.1]}$$

## G.2 Uncertainty Calculations

### G.2.1 Air Density ($\rho$)

The uncertainty in the air density $\Delta\rho$ is calculated by deriving Equation G.3 from the methods used above (for Equation G.1), from Equation 2.15 (restated below).

$$\rho = \frac{P_{atm}}{R_{air} T_\infty} \qquad \text{[2.15]}$$

$$\Delta\rho = \left| \frac{\partial \rho}{\partial P_{atm}} \right| \Delta P_{atm} + \left| \frac{\partial \rho}{\partial T_\infty} \right| \Delta T_\infty \qquad \text{[G.2]}$$

$$\Delta\rho = \frac{1}{R_{air}} \left[ \left| \frac{1}{T_\infty} \right| \Delta P_{atm} + \left| -\frac{P_{atm}}{T_\infty{}^2} \right| \Delta T_\infty \right] \qquad \text{[G.3]}$$

Taking the average ambient temperature and pressure to be 293°K and 101300 Pa respectively, and the corresponding uncertainties ($\Delta T_\infty$ and $\Delta P_{atm}$) to be ±0.1°K and ±50 Pa as well, the uncertainty in air density is calculated to be ±0.001 kg/m³.

### G.2.2 Dynamic Pressure ($P_{dyn}$)

For the equation used to calculate the dynamic pressure $P_{dyn}$ as presented in Chapter 2, Equation G.5 for the uncertainty in the dynamic pressure $\Delta P_{dyn}$ is derived.

$$P_{dyn} = 673.7(V - V_0) \qquad \text{[2.16]}$$

$$\Delta P_{dyn} = \left| \frac{\partial P_{dyn}}{\partial V} \right| \Delta V + \left| \frac{\partial P_{dyn}}{\partial V_0} \right| \Delta V_0 \qquad \text{[G.4]}$$

$$\Delta P_{dyn} = 673.7(\Delta V + \Delta V_0) \tag{G.5}$$

Estimating the error in $V_0$ from the voltmeter ($\Delta V_0$) to be ±0.001 V, and the error in $V$ ($\Delta V$) to be ±0.01 V, an uncertainty of ±7 Pa was calculated for the dynamic pressure using Equation G.5.

## G.2.3 Airspeed ($U_\infty$)

For an airspeed of 8 m/s (from September 18th 2016 test) the dynamic pressure was taken to be 42 Pa, and the air density to be 1.2 kg/m$^3$. Using the uncertainties estimated for air density and dynamic pressure in the derived Equation G.7 (from Equation 2.17), the uncertainty in the airspeed $\Delta U_\infty$ was calculated to be ±0.7 m/s.

$$U_\infty = \sqrt{\frac{2P_{dyn}}{\rho}} \tag{2.17}$$

$$\Delta U_\infty = \left| \frac{\partial U_\infty}{\partial P_{dyn}} \right| \Delta P_{dyn} + \left| \frac{\partial U_\infty}{\partial \rho} \right| \Delta \rho \tag{G.2}$$

$$\Delta U_\infty = \frac{\sqrt{2}}{2} \left[ \left| \frac{1}{\sqrt{\rho P_{dyn}}} \right| \Delta P_{dyn} + \left| -\sqrt{\frac{P_{dyn}}{\rho^3}} \right| \Delta \rho \right] \tag{G.3}$$